

**„Correlated network activity forms computational subcircuits
in the accessory olfactory bulb“**

Von der Fakultät für Mathematik, Informatik und Naturwissenschaften der RWTH
Aachen University zur Erlangung des akademischen Grades eines
Doktors der Naturwissenschaften genehmigte Dissertation

vorgelegt von

Master of Science

Sebastian Tobias Malinowski

aus

Bergheim

Berichter: *Univ.-Prof. Dr. rer. nat. Marc Spehr*

Prof. Yoram Ben-Shaul, Ph.D.

Tag der mündlichen Prüfung: 30.08.2022

Diese Dissertation ist auf den Internetseiten der Universitätsbibliothek verfügbar.

Contents

1. Introduction	1
1.1 Chemosensory Communication	1
1.2 The Accessory Olfactory System	3
1.2.1 The Vomeronasal Organ	3
1.2.2 The Accessory Olfactory Bulb	7
1.3 Neural Oscillations	10
1.3.1 Oscillatory Activity Patterns	11
1.3.2 Accessory Olfactory Bulb Mitral Cell Oscillations	13
1.4 Cellular Calcium Signalling	14
1.4.1 The Cellular Calcium Signalling Toolkit	17
1.4.2 Using Calcium Measurements to Study Neural Activity	18
1.5 Aims	20
2. Materials & Methods	21
2.1 Materials	21
2.1.1 Equipment	21
2.1.2 Chemicals	22
2.1.3 Consumables	24
2.1.4 Primer	25
2.1.5 Solutions	25
2.1.6 Animals	28
2.1.7 Genotyping	28
2.1.8 Software	29
2.2 Methods	30
2.2.1 Surgical Procedures	30
2.2.2 Data Acquisition	32
2.2.3 Data Analysis	35

3. Results.....	41
3.1 AOB Mitral Cell Calcium Activity <i>In Vitro</i>	41
3.1.1 Spontaneous Calcium Activity in AOB Mitral Cells	42
3.1.2 Rhythmic AOB Mitral Cell Discharge	44
3.1.2 AOB Mitral Cells Organize into Distinct Microcircuits	48
3.1.3 Pharmacological Dissection of Spontaneous AOB Mitral Cell Network Activity	52
3.1.4 Pharmacological Dissection of AOB Microcircuit Formation	58
3.2 AOB Mitral Cell Calcium Activity <i>In Vivo</i>	59
3.2.1 AOB Mitral Cell Imaging Using Glass Microprisms	59
3.2.2 Spontaneous AOB Mitral Cell Activity.....	62
4. Discussion	78
4.1 Calcium Oscillations are a Hallmark of Mitral Cell Network Activity	78
4.2 Accessory Olfactory Bulb Network Computation.....	81
4.2.1 Effects of Oscillatory Activity on Sensory Input.....	81
4.2.2 Microcircuits as Functional Subnetworks of the Accessory Olfactory Bulb.....	82
4.2.3 Effects of Oscillatory Activity on Accessory Olfactory Bulb Output	85
4.3 Mitral Cell Network Pharmacology	86
4.4 Future Directions based on Single-Cell Mitral Cell Calcium Imaging <i>In Vivo</i> ..	89
5. Summary	91
6. References	92
7. Abbreviations.....	111
8. Acknowledgement	114
9. Curriculum Vitae	116
10. Eidesstattliche Erklärung	120

1. Introduction

For every living organism it is indispensable to detect and compute cues from the outer world to ensure continuity. Each taxon developed a unique set of different sensory systems to screen the environment for important information. These systems are tuned and highly specialized to detect one specific physical stimulus type (Müller, 1826). Aside the detection of soundwaves or light, the detection of chemosensory cues, either volatile or non-volatile, is of utmost importance to nearly all species (Manzini, Schild and Di Natale, 2022).

1.1 Chemosensory Communication

Together with the gustatory system, the sense of smell is capable to decode information mediated by a myriad of different chemical cues (Chamero, Leinders-Zufall and Zufall, 2012). Whereas taste provides information about non-volatile molecules, indicating, for example, quality of food (Lapis, Penner and Lim, 2016), smell is used to detect both, volatile and non-volatile compounds (Mombaerts, 2004). Especially with respect to social interactions, like territorial behaviour, mating or maternal care, detecting semiochemicals emitted by other individuals is crucial (Lin *et al.*, 2005). These chemosignals convey information about the sender's identity, sexual state, or health status (Ache and Young, 2005; Ferrero *et al.*, 2011; Boesveldt and Parma, 2021). Depending on their function they can either be highly volatile to span large distances, or stationary to keep information at one place for a longer period.

Whereas genetic evidence for peripheral receptors detecting these cues was found decades ago (Ngai *et al.*, 1993; Dulac and Axel, 1995), knowledge about the exact identity of most receptor-ligand pairs and the underlying brain circuit computation, leading to changes in behaviour or endocrine state, remains fragmentary at best. This causes two major problems: First, we do not know which semiochemicals act as mediators for a given information and, second, we lack a deep understanding where in the brain a certain cue is computed.

A major step towards unravelling these issues would be to gain deeper functional knowledge of individual olfactory subsystems. We need to understand which ligands are detected by which subsystem, which brain areas receive input from this detected information and how these subsystems interact. Finally, to gain a comprehensive

1. Introduction

understanding of behaviour, we also need to account for multimodal inputs, refining the reaction of an organism to its environment.

Socially relevant chemosensory stimuli are detected by the olfactory system, which is subdivided into anatomically separated subsystems (Brennan and Zufall, 2006) (Figure 1). For most mammals, these are the main olfactory system (MOS), the accessory olfactory system (AOS) (Spehr, 2010), the Grueneberg Ganglion (Grüneberg, 1973) and the Septal Organ of Masera (Rodolfo-Masera, 1943).

For a long time, information processing in the MOS and AOS was regarded functionally separate based on divergent projections of bulbar mitral and tufted cells (Scalia and Winans, 1975). More recent findings, however, indicate that anatomical connections between these subsystems already exists on bulbar level (Vargas-Barroso *et al.*, 2016) and that their information is also merged and integrated in higher brain areas (Spehr *et al.*, 2006; Baum, 2012).

The peripheral structure of the MOS is the main olfactory epithelium (MOE). The murine MOE contains around 1000 isoforms of odorant receptors (Buck and Axel, 1991). They are broadly tuned to volatile odorant cues (Tazir *et al.*, 2016). Aside from odorant detection, there is accumulating evidence that the MOS is also capable of detecting socially relevant cues. Trace amine-associated receptors expressed in sensory neurons (Liberles and Buck, 2006; Ferrero *et al.*, 2011) or the non-GPCR MS4A protein expressed in sensory neurons of the necklace subsystem (Greer *et al.*, 2016) are detecting intra- or conspecific chemosensory cues and elicit behavioural responses. While early-stage processing in the MOS is relatively well understood, even at transcriptional levels (Tsukahara *et al.*, 2021), we lack a comprehensive understanding of AOS function.

1. Introduction

1.2 The Accessory Olfactory System

In many mammalian species, the AOS plays a crucial role in extracting information during social interactions to initiate changes in behaviour and physiological state (Chamero, Leinders-Zufall and Zufall, 2012). Chemical cues emerged as predominant carriers of information between most animals about social hierarchy, endocrine and sexual state, as well as individuality (Brennan and Zufall, 2006). This is true for both intra- and interspecific levels. Rodents, and mice in particular, developed an exceptionally sensitive and accurate sense of smell. In addition, ever increasing opportunities for neuroscientific research due to advanced mouse genetics (Kim *et al.*, 2018) make mice an attractive model organism to study olfactory function. Hence, the following paragraphs will describe the accessory olfactory system, using mice as example.

1.2.1 The Vomeronasal Organ

The peripheral detection organ of the AOS is the vomeronasal organ (VNO). This structure was first described in several domesticated animal species by the Danish anatomist Ludvig Jacobson in 1813 (Trotier and Doving, 1998). Therefore, it is also known as Jacobson's organ. He and others described the organ as a paired cylindrical structure at the base of the anterior nasal septum (Ciges *et al.*, 1977; Halpern, 2003). It is blind-ending and encapsulated by a cartilaginous capsule. Its opening is extended via the vomeronasal duct into the anterior part of the nasal cavity (Figure 1).

The VNO in the mature mouse accommodates around 100,000 to 200,000 vomeronasal sensory neurons (VSNs) in a crescent-shaped sensory epithelium (Wilson and Raisman, 1980, Figure 1). They are supported, structurally and metabolically, by a band of sustentacular cells. VSNs are bipolar neurons, extending a small unbranched dendrite towards the VNO lumen. Here, a VSN extends numerous microvilli that contact the vomeronasal mucus. This physical contact with the external environment enables the detection of semiochemical cues.

1. Introduction

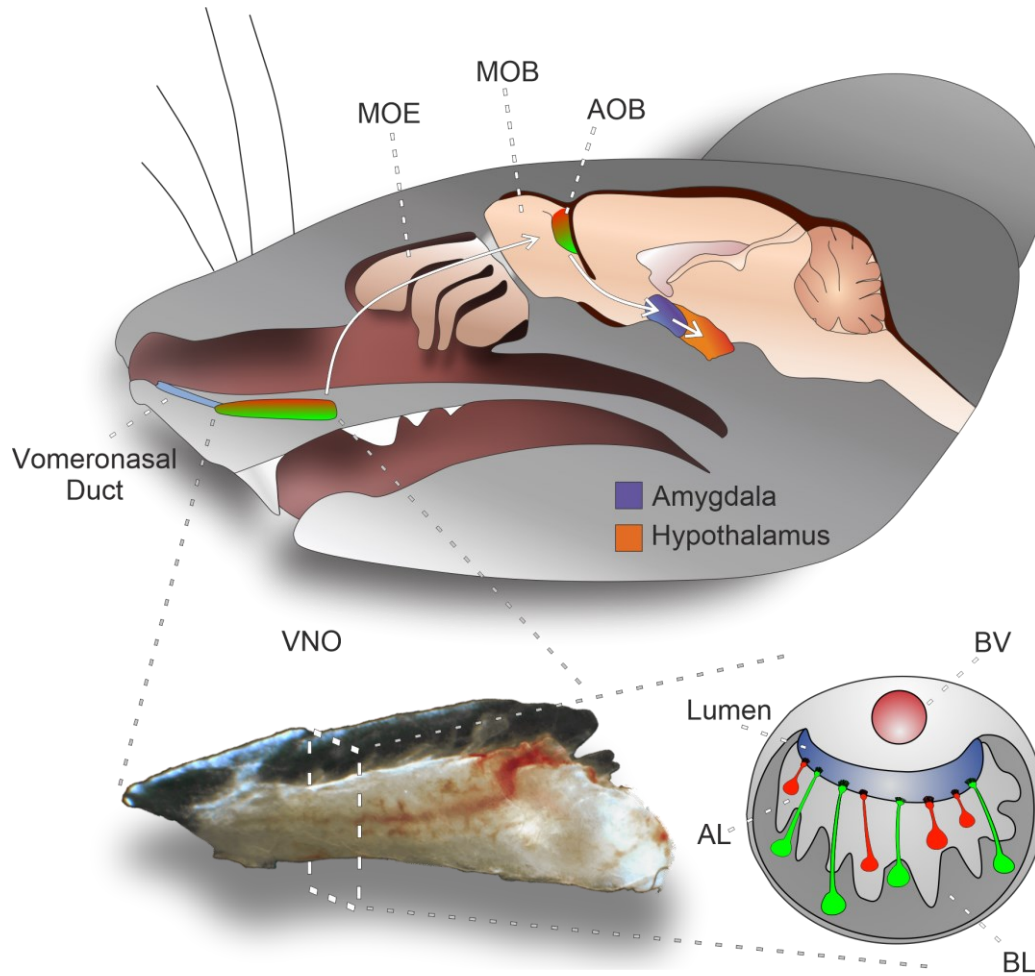


Figure 1: The Accessory Olfactory System. Schematic overview of the mouse AOS. Sagittal mouse head illustrating the two major olfactory subsystems. The vomeronasal organ (VNO) can actively suck semiochemicals into the vomeronasal duct. Apical (red) and basal (green) vomeronasal sensory neurons (VSNs) extract information and forward it to glomeruli of the anterior (red) and posterior (green) accessory olfactory bulb (AOB). AOB main projection neurons (mitral cells) project to the vomeronasal amygdala (blue), which is connected to hypothalamic neuroendocrine centers (orange). The VNO is encapsulated by a cartilaginous capsule. The non-sensory area contains a blood vessel (BV). VSNs are either located in the apical layer (AL) or basal layer (BL) of the sensory epithelium. Adapted from Mohrhardt, Nagel et al., 2018.

VSNs extend a long unmyelinated axon. At the basal lamina, these axons coalesce into vomeronasal nerve bundles (Figure 2). These enter the brain through the cribriform plate together with olfactory nerve fibres, projecting along the medial olfactory bulbs, and finally target the glomerular layer of the AOB (Meredith, 1991; Belluscio *et al.*, 1999; Rodriguez, Feinstein and Mombaerts, 1999, Figure 2B).

1. Introduction

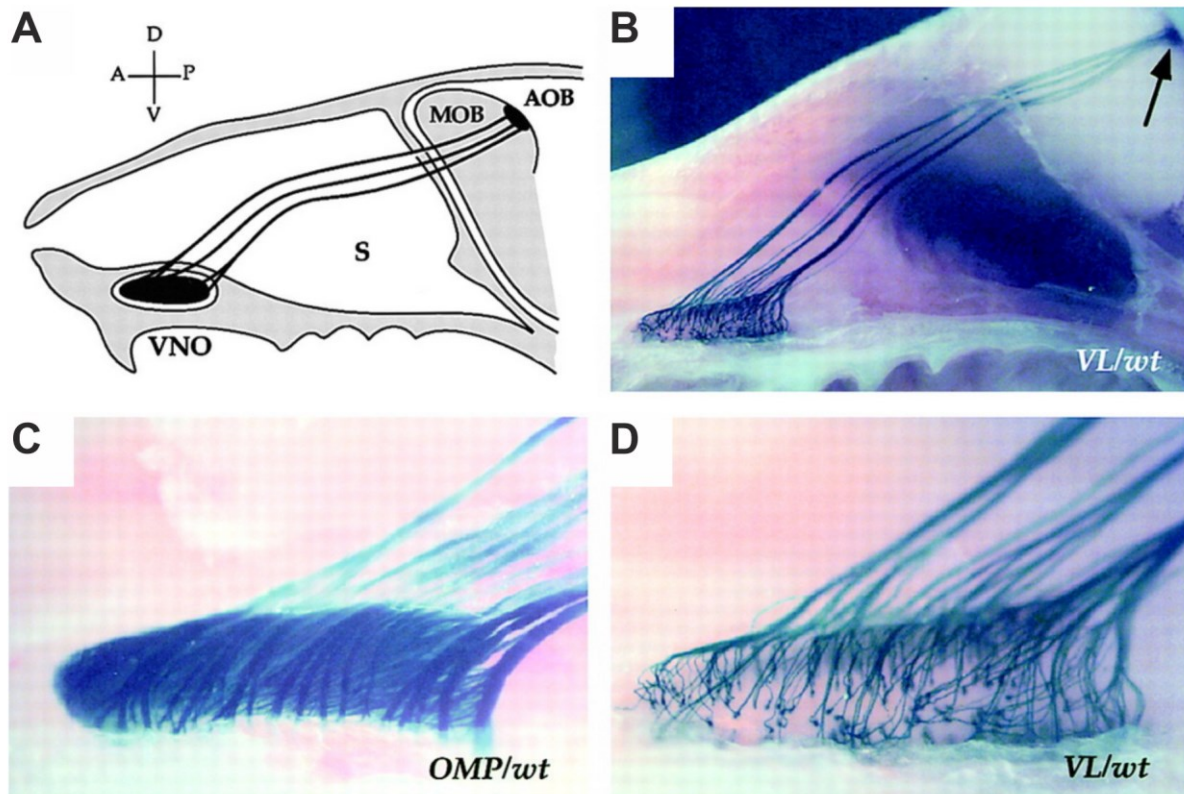


Figure 2: Projections of the Vomeronasal Organ. **A:** Schematic parasagittal section of a mouse head. Depicted is the axonal innervation from vomeronasal organ (VNO) axons through the septum (S) and cribriform plate towards the accessory olfactory bulb (AOB, black arrow), bypassing the main olfactory bulb (MOB) laterally. **B:** Whole-mount sagittal section of a VR2-IRES-tdTomato mouse, stained with X-gal. VR2 neurons project axon bundles towards the accessory olfactory bulb (AOB, black arrow). **C:** Lateral whole-mount view of the VNO from a heterozygous OMP-tdTomato mouse. All vomeronasal sensory neurons expressing the olfactory marker protein (OMP) are visible. **D:** Same whole-mount specimen as in B zoomed in towards the VNO. Note that only VR2 neurons are stained. Adapted from Rodriguez, Feinstein and Mombaerts, 1999.

On its lateral side, the VNO displays a large blood vessel (Figure 1). This blood vessel is surrounded by highly vascularized tissue. Here, rich innervation of sympathetic fibres can be found (Trotier and Doving, 1998). A large portion of these fibres originate from the superior cervical ganglion (Meredith and O'Connell, 1979; Ben-Shaul *et al.*, 2010). Evidence from behaving hamsters indicates that, upon arousal, vomeronasal pumping activity increases and enables stimulus uptake (Meredith, 1994). The exact mechanism, however, remains elusive. One hypothesis is that arousal leads to an increase in adrenergic activation of the blood vessel, leading to vasoconstriction and to negative intraluminal pressure (Meredith *et al.*, 1980). As a result, volatile and non-volatile stimuli can enter the vomeronasal duct and finally the VNO lumen. Stimulus sources of less volatile stimuli like peptides and proteins can thereby be actively extracted from faecal excretions, vaginal secretions, tears or urine (Wysocki, Wellington and Beauchamp, 1980; Luo, Michale S. Fee and Katz, 2003).

1. Introduction

The VNO, however, cannot only detect pheromones. It is furthermore important for predator sensing (Chamero, Leinders-Zufall and Zufall, 2012), prey detection (Halpern and Frumin, 1979), and intra- and interspecific communication (Hurst *et al.*, 2001; Leinders-Zufall *et al.*, 2004; Wyatt, 2009).

Pheromones are detected by vomeronasal receptors. Most VSNs express either vomeronasal receptor type 1 (V1R) (Dulac and Axel, 1995, Figure 1) or vomeronasal receptor type 2 (V2R) (Herrada and Dulac, 1997; Matsunami and Buck, 1997; Ryba and Tirindelli, 1997, Figure 1). Each of these two receptor families contain more than 100 potentially functional receptors (Del Punta *et al.*, 2002; Roppolo *et al.*, 2007; Young and Trask, 2007). Another prominent receptor family, albeit of substantially smaller gene family size, are formylated peptide receptors (FPRs) (Liberles *et al.*, 2009; Rivière *et al.*, 2009).

V1R receptors are $G_{\alpha i2}$ -coupled and are expressed in the more apical part of the VNO sensory epithelium. Their projections target the anterior AOB (Figure 1, red). Although not many receptor ligand pairs are known, V1Rs are thought to detect small molecules (Chamero, Leinders-Zufall and Zufall, 2012). Here, for example 2-heptanone (Boschat *et al.*, 2002) and sulphated estrogens (Isogai *et al.*, 2011; Haga-Yamanaka *et al.*, 2014; Haga-Yamanaka, Ma and Yu, 2015) were shown to activate Vmn1r49 and Vmn1r85, respectively.

V2Rs on the other hand are $G_{\alpha o}$ -coupled, often coexpressed with H2-Mv receptors (Ishii, Hirota and Mombaerts, 2003), and located in the basal VNO (Figure 1, green). V2Rs project to the posterior part of the AOB. They display a large putative extracellular ligand binding site and enable the detection of large non-volatile peptides and proteins, such as major urinary proteins (MUPs) or major histocompatibility complex (MHC) peptides (Cheetham *et al.*, 2007; Chamero, Leinders-Zufall and Zufall, 2012).

The third member of vomeronasal receptors is associated with the detection of sickness-related substances. Some members of the formyl peptide receptors (FPR), FPR1 and FPR2, are expressed by neutrophils and monocytes (Le, Murphy and Wang, 2002). They function as sensors for bacterial metabolites and inflammatory modulators (Kolaczowska and Kubes, 2013). These two receptors, however, are not expressed in VSNs. In contrast, FPR3 is found in both, immune cells and VSNs.

1. Introduction

FPR3 is coexpressed with $G_{\alpha o}$ -positive VSNs, other FPR-rs family members are expressed in $G_{\alpha i2}$ -positive VSNs (Munger, 2009).

VSNs are extremely sensitive chemosensors. They detect ligand concentrations in the picomolar to low nanomolar range, which was shown for MHC peptides (Leinders-Zufall *et al.*, 2004) and sulfated steroids (Haga-Yamanaka, Ma and Yu, 2015; Chamero *et al.*, 2017). VSN axons are organized as large, tightly fasciculated fibre bundles, finally targeting the caudal part of the AOB. Then they are segregating according to receptor identity and targeting either the rostral or caudal entrance region.

1.2.2 The Accessory Olfactory Bulb

The AOB is subdivided into several functionally and anatomically different layers (Larriva-Sahd, 2008) and represents the first processing stage of the AOS. The entrance region of the AOB is the glomerular layer (GL) (Figure 1A-B, Figure 3). VSN axons target this region. Sensory input from the VNO to the AOB is topographically organized along its rostro-caudal axis. V1R-positive (apical) projections terminate in the anterior AOB, V2R-positive (basal) projections terminate in the posterior AOB (Figure 1). V1R-positive VSNs express the olfactory axon cell adhesion molecule (OCAM) and make synapses with OCAM-negative AOB mitral cells (AMC) in the rostral region of the GL (Belluscio *et al.*, 1999; Rodriguez, Feinstein and Mombaerts, 1999). In contrast, V2R-positive neurons lack OCAM expression, therefore targeting OCAM-positive AMCs in the caudal part of the GL. FPR-rs3-positive VSNs synapse on AMCs in the rostral AOB (Dietschi *et al.*, 2013).

In the GL, synapses between VSN axons and AMC dendrites form glomeruli (Figure 3). One receptor-specific VSN population is targeting 4-30 individual glomeruli (Belluscio *et al.*, 1999; Rodriguez, Feinstein and Mombaerts, 1999; Wagner *et al.*, 2006). AOB glomeruli are diffusely organized, typically having a diameter of 10-30 μm (Tirindelli *et al.*, 2009). They are tightly clustered and sparsely surrounded by inhibitory interneurons, the periglomerular cells (PGCs). The exact computational function of PGCs is not fully understood yet (Dulac and Wagner, 2006).

1. Introduction

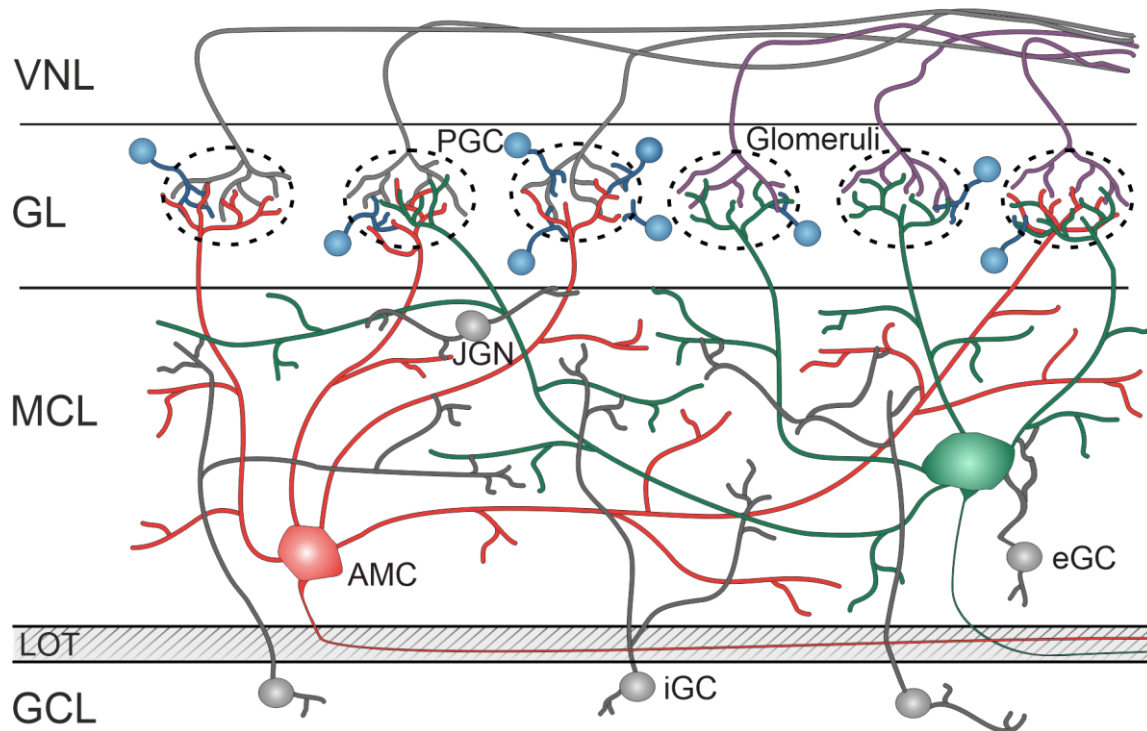


Figure 3: Wiring Pattern of the AOB. Axonal projections of VSNs entering the AOB via the vomeronasal nerve layer (VNL). In the glomerular layer (GL) they make synapses with AMCs, the main projection neurons of the AOB. In addition, PGCs add inhibitory modulation to the glomeruli (black circles). AMC somata are located in the mitral cell layer (MCL). Here, in a subglomerular zone they share synapses with juxtglomerular neuron (JGN). Furthermore, AMCs share dendrodendritic synapses with external granule cells (eGC). AMCs forward excitatory, glutamatergic input to granule cells, whereas they make a GABAergic inhibitory backprojection. The lateral olfactory tract (LOT) is a fiber tract sending projections from AMCs and main olfactory bulb projections to higher brain areas. He also builds a prominent border between MCL and granule cell layer (GCL). The GCL mainly harbors axonless internal granule cells (iGC). Their dendrites extend towards AMCs in the MCL. Adapted from Mohrhardt, Nagel et al., 2018.

AMCs are the main projection neurons of the AOB. Their somata are located in the mitral cell layer (MCL) (Figure 3). They are the only AOB neurons that receive input from the peripheral detection structure, the VNO, and that forward information to higher brain areas, like amygdala and hypothalamus. This information flow is initially mediated via the lateral olfactory tract (LOT).

Despite their designation as “mitral cells”, in analogy to mitral cells in the main olfactory bulb, AMC morphology is highly heterogeneous. Cell bodies, dendritic arborisations, axonal projections and even location differ dramatically among neurons (Salazar *et al.*, 2006). One AOB hemisphere contains roughly 7000 AMCs (Mohrhardt *et al.*, 2018). Not only extending apical glomerular dendrites (Takami and Graziadei, 1991; Meisami and Bhatnagar, 1998), AMCs also display secondary dendrites in lateral direction that are shorter in length and fewer in number (Mori, 1987).

1. Introduction

A prominent physiological speciality of the olfactory bulb, including the AOB, is the reciprocal dendrodendritic synapse (Didier *et al.*, 2001; Shepherd *et al.*, 2007). The unique feature of these synapses is that both opposing synaptic compartments share pre- and postsynaptic elements. They are formed between inhibitory interneurons, granule cells (GCs), and AMCs in the MCL. GCs are further subdivided into external GCs (eGC), located within the MCL, and internal GCs (iGC), located in the granule cell layer (GCL) (Larriva-Sahd, 2008) (Figure 3). Here, eGCs form synapses with the proximal dendritic regions and AMC somata. On the other hand, iGCs form synapses with distal AMC dendrites.

Presynaptically, AMCs form glutamatergic synapses with GCs, mediating excitation. On the other hand, GCs mediate presynaptic GABA release onto AMCs, mediating reciprocal inhibition. Physiologically, this leads to both self- and / or lateral inhibition of AMCs upon activation. Self-inhibition could silence distinct AMCs. In addition, lateral inhibition is a mechanism for contrast enhancement (Price and Powell, 1970; Schoppa and Urban, 2003) and was shown to be involved in olfactory memory formation (Kaba *et al.*, 1994; Brennan and Keverne, 1997).

AOB output is mediated via AMC axons, leaving the brain region as a fibre bundle via the LOT together with MOB mitral cell axons. Some of the AMC axons seem to not directly lay in the LOT, but cross the border between anterior and posterior AOB (Vargas-Barroso *et al.*, 2016). This is intriguing, because anatomically there is supposed to be a clear cut border between these two areas (Larriva-Sahd, 2008). The exact physiological function of this connection, however, is unclear.

The AOB receives top-down input from many different brain areas like the corticomedial amygdala and the bed nucleus of the stria terminalis (Broadwell and Jacobowitz, 1976; Fan and Luo, 2009). In addition, top-down modulation by the locus coeruleus, the horizontal limb of Broca and the raphe nuclei are known (Smith and Araneda, 2010a; Oboti *et al.*, 2018). Fibres from these nuclei enter the AOB either via the bulbar core white matter or the LOT (Larriva-Sahd, 2008). For example, noradrenergic activation of $\alpha 1$ -receptors was shown to increase GABA release by GCs, leading to AMC inhibition (Araneda, 2006). Linking AOB modulation to the AOS role in regulating the endocrine state of the animal, projection neurons in both amygdala and bed nucleus of the stria terminalis express ER- α estrogen receptors

1. Introduction

(Fan and Luo, 2009). This is a possible mechanism how endocrine state and the AOS are linked.

One of the most intriguing features of the AOS is that important behaviours like aggression, mating and the change in endocrine state are processed input-to-output along a neural pathway of only 2-3 relay synapses. Starting from the VNO that detects sensory input, information is forwarded to the AOB where AMCs project to higher brain areas like the vomeronasal amygdala (Martinez-Marcos, 2009). This means that the AOS, unlike other sensory systems, bypasses the thalamocortical axis. The unique cortical target of the AOB is the posteromedial cortical nucleus of the amygdala (Gutiérrez-Castellanos *et al.*, 2014). This target, together with the medial amygdala, builds the vomeronasal amygdala. Here, pheromonal signals elicit either innate or conditioned fear responses (Duvarci and Pare, 2014) or modulate responses in a state-dependent manner (Stowers and Liberles, 2016). Receiving direct input from AMCs, the medial amygdala forwards information to the ventromedial hypothalamus (VMH). VMH triggers defensive behaviours in response to predator cues, but also reproductive and aggressive responses. Moreover, recent findings indicate a role of AMC activity in guiding pulsatile neuroendocrine release (Gorin *et al.*, 2016; Tsitoura *et al.*, 2020). These downstream targets include nuclei that contain gonadotropin-releasing hormone neurons (Chu *et al.*, 2012), as well as vasopressin neurons (Brown, 2004).

1.3 Neural Oscillations

Decoding of environmental stimuli into signals the brain can process is crucial. Signal components on a neuronal level can either be computed by amplitude modulation, or in a temporal domain via frequency modulation. Amplitude modulation enables the coding of signal strength and duration via the extent of change in membrane potential and its duration. Frequency modulation, however, describes the frequency of membrane potential fluctuations, always using the same amplitude and duration of one event. In a neuronal context these frequencies are displayed via action potentials (APs). APs not only occur as single events, but can either extend their coding ability by occurring in units of bursts (Lisman, 1997), generating local field potentials (Losacco *et al.*, 2020), or displaying precisely rhythmic windows of excitation (Mizuseki *et al.*, 2009).

1.3.1 Oscillatory Activity Patterns

Rhythmically occurring windows of excitation are classified as oscillatory activity (Berger, 1929). Oscillatory activity patterns are a widespread coding strategy in neuronal networks and can be observed both at the level of APs and local field potentials (Buzsáki and Draguhn, 2004). Oscillatory activity increases the coding capacity of neuronal networks. Therefore, this phenomenon occurs throughout the brain with different characteristics.

Observing thalamocortical activity, it can be linked to behavioural states like sleep and arousal (Steriade, McCormick and Sejnowski, 1993). Here, depending on the brain state and the behavioural output, the oscillatory activity can be highly variable in rhythmicity and frequency (von Krosigk, Bal and McCormick, 1993).

Oscillatory patterns enable temporal tuning of large populations of neurons and increase their coding capacity (Buzsáki, Logothetis and Singer, 2013). Depending on the brain area function and the time scales relevant for a given sensory system, oscillatory frequencies vary from infraslow (<0.1 Hz) (Schroeder and Lakatos, 2009) to ultra-fast (200-600 Hz) frequencies (Buzsáki and Draguhn, 2004, Figure 4). This is described for the visual system (Gochin *et al.*, 1994), the control of motor functions (Galvan and Wichmann, 2008), learning processes (Lisman, 1999) and, finally, also the AOS (Gorin *et al.*, 2016).

Two distinct ways are known how neuronal networks can establish, maintain and change their oscillatory activity. First, the oscillations can emerge from intrinsic pacemaker properties of a neuron population or subpopulation (Marder and Bucher, 2001; Gorin *et al.*, 2016). Here, changes in membrane conductance lead to ion in- or outflux and therefore changes membranes potential (Llinás, 1988). Second, these pacemaker neurons can entrain other cells within the neuronal network. This influences their excitatory and inhibitory periods, leading to consolidation or change in frequency of oscillatory activity (Fries, 2015). The coupling can either be maintained via electrical coupling, mediated by gap junctions (Bennett and Zukin, 2004), or via chemical synapsis using different neurotransmitters (Crunelli and Hughes, 2010).

1. Introduction

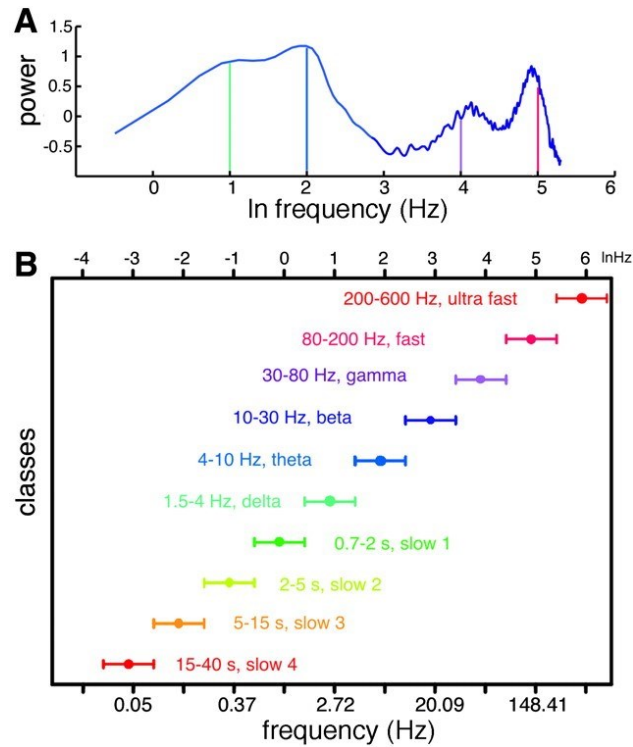


Figure 4: Oscillation Frequencies in the Brain are Widespread and Heterogeneous. **A:** Power spectrum of hippocampal EEG during sleep and awake periods in the mouse. The spectrum was “whitened” by removing logarithmic slope. The four peaks close to logarithmic integers are color-coded as the peaks in **B**. **B:** Oscillatory spectra in the rat cortex. Note the linear progression of frequency classes on the logarithmic scale. Bars indicate the range of frequencies for different bands. Adapted from Buzsáki and Draguhn, 2004.

Neuronal oscillations can be quantified by measures like power spectral density (PSD) and autocorrelation (Buzsáki and Draguhn, 2004, Figure 4). The PSD displays the power over the analysed frequency range of a given signal. This approach gives an estimation of a certain frequency band’s power within the signal by calculating the Fourier transformation of its autocorrelation (Gupta *et al.*, 2020, Figure 4).

The autocorrelation is used to detect periodicity in a given signal analysing its relation in time (‘Correlation Methods’, 2003; Vilela *et al.*, 2013). Here, the signal is time-shifted to itself to detect self-similarity at certain time lags. This can also be done for two different neuronal signals to detect a possible activity coupling in the time domain. This measure is referred to as cross-correlation (Narayanan and Laubach, 2009).

Calculating these measures allows to quantify and analyse the influence of oscillations on information coding. For example, infra-slow oscillations are meant to function as a reset for the computation in certain brain regions via either phase or amplitude coding (Buzsáki, Logothetis and Singer, 2013). This organized periodic activity enables neuronal networks to extend their computational properties. In the main olfactory system, for instance, spike synchronization facilitates odour recognition (Brody and

1. Introduction

Hopfield, 2003). Furthermore, this effect is meant to play an important role in the AOS indicated, both, *in vitro* and *in vivo* (Gorin *et al.*, 2016; Zylbertal, Yarom and Wagner, 2017; Tsitoura *et al.*, 2020). The exact biological function, however, needs to be further investigated.

1.3.2 Accessory Olfactory Bulb Mitral Cell Oscillations

As discussed, neuronal oscillations play a crucial role in brain function. There is evidence that the olfactory sense uses this mechanism extensively to process information. This was shown for the main olfactory bulb (Schaefer *et al.*, 2006; Liu and Shipley, 2008). Oscillations in the main olfactory system are coupled to breathing and are relatively fast (Hayar *et al.*, 2004). In the AOS, however, it was shown that infraslow oscillations in the range <0.1 Hz seem to be most prominent (Vargas-Barroso *et al.*, 2016; Gorin *et al.*, 2016; Zylbertal, Yarom and Wagner, 2017; Tsitoura *et al.*, 2020). This evidence is true *in vivo* as well as *in vitro*. In addition, *in vivo* experiments indicate no coupling between the animals breathing and AMC oscillations (Luo, Michale S. Fee and Katz, 2003; Ben-Shaul *et al.*, 2010).

General oscillation patterns in the AOB, however, can be diverse or highly regular in frequency over several minutes (Gorin *et al.*, 2016; Tsitoura *et al.*, 2020). Furthermore, *in vitro* experiments show that not every AMC is oscillating. In electrophysiological *in vitro* experiments oscillating AMCs made up 69.7% of the total population (Gorin *et al.*, 2016). Taking this into account, together with the heterogeneity of oscillation frequencies, it is tempting to speculate that this might be a mechanism to cluster particular subsets of AMCs into functional AOB subunits. Hereby, one of these clusters could function as a computational subunit for one specific VSN receptor identity. This idea is further supported by the fact that some AMCs oscillate intrinsically, whereas some are entrained by others.

Intrinsically oscillating AMCs show rhythmic behaviour based on their ion channel composition. This was shown to be established by interdependent subthreshold persistent Na^+ currents, R-type Ca^{2+} currents and Ca^{2+} activated big conductance K^+ currents (Gorin *et al.*, 2016). These AMCs cease their oscillatory pattern after hyperpolarisation of their membrane potential in a whole-cell patch clamp experiment. Synaptically driven AMC oscillations are maintained during hyperpolarisation as subthreshold oscillations. The physiological meaning of recruiting synaptically driven

1. Introduction

AMCs by intrinsic pacemaker cells, however, remains speculative. Therefore, we do not know to which extent the AOS makes use of the additional temporal coding opportunities that these oscillatory activity patterns offer. Moreover, the exact impact on higher brain areas like the vomeronasal amygdala and the hippocampus, leading the changes in behaviour and endocrine state of the animal, needs further investigation.

1.4 Cellular Calcium Signalling

The bivalent ion calcium is involved in nearly all cellular regulation processes (Clapham, 2007). It is an intracellular messenger that is involved in cellular functions like neuronal excitability, secretions, muscle contractions, gene expression and apoptosis (Ringer, 1883; Orrenius, Zhivotovsky and Nicotera, 2003). In every cell, the cytosolic calcium concentration is tightly controlled. Due to a high concentration gradient over the plasma membrane even minor increases in calcium conductivity result in relatively large currents, rapidly changing the intracellular calcium concentration (Carafoli, 1988). This enables the control of calcium in two domains: temporal and spatial.

At resting conditions, the cytoplasmic calcium concentration is around 100-200 nM. Extracellular calcium levels, however, are approximately 1 mM. The changes of intracellular calcium concentration are fast due to the more than 10,000-fold lower concentration compared to the outside. Furthermore, due to the low cytosolic calcium concentration, changes in small cellular compartments, so-called microdomains, tightly regulate cell homeostasis in space (Berridge, 2006). Calcium influx to the cytosol, however, is not only maintained from extracellular sources. Indeed, internal calcium storages play a major role in calcium homeostasis (Giorgi, Marchi and Pinton, 2018).

The major intracellular calcium storage organelle is the endoplasmic reticulum (ER), especially the smooth ER (Figure 5). Its intracellular calcium concentration is in the high micromolar range (Berridge, 2002). The ER releases calcium into the cytosol via either inositol 1,4,5-trisphosphate receptors (Ins(1,4,5)P₃R) or via ryanodine receptors (RyR). These receptors are calcium sensitive, enabling a calcium-induced calcium release. On the other hand, the ER calcium store is filled via pumps (Lytton *et al.*, 1992). This process needs hydrolysis of ATP and is maintained by the sarcoplasmic / endoplasmic reticulum calcium ATPase (SERCA) pump.

1. Introduction

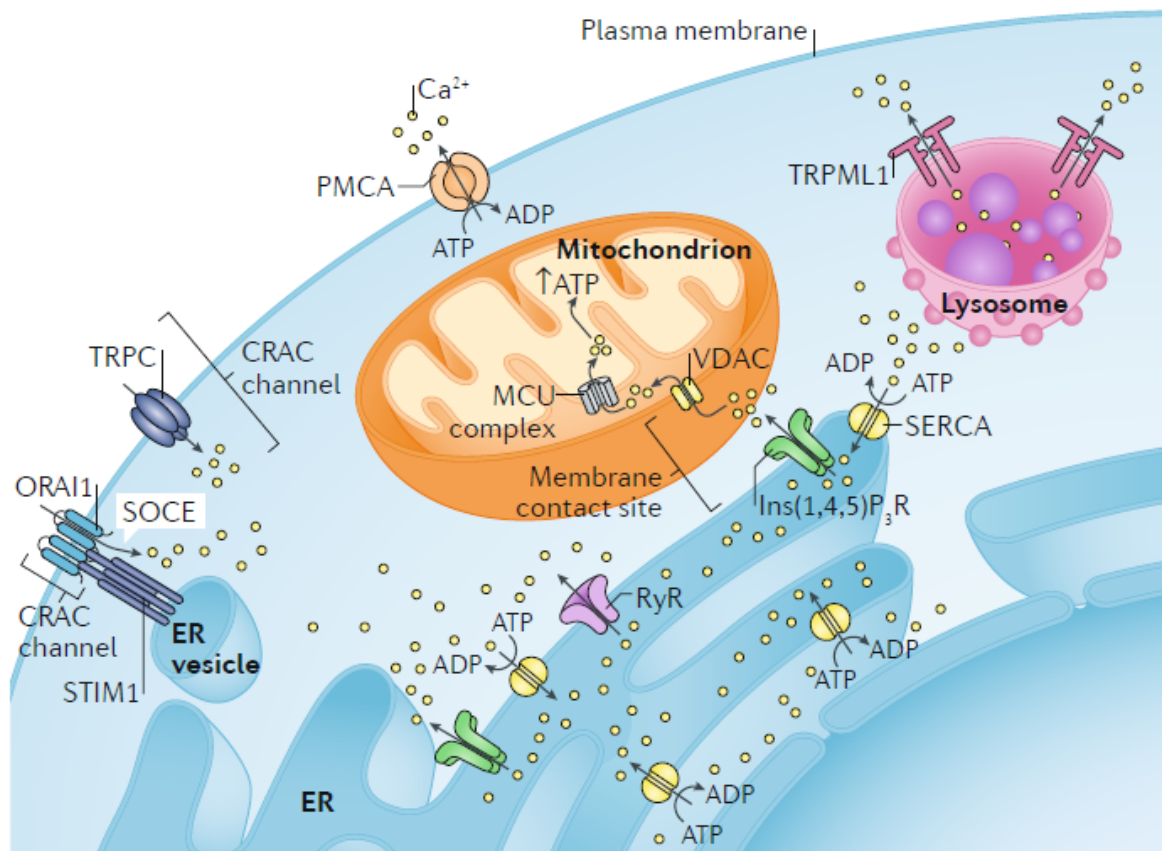


Figure 5: Intracellular Calcium Signalling. The major intracellular calcium storage of the cell is the endoplasmic reticulum (ER). Calcium release from the ER is mediated by inositol 1,4,5-trisphosphate receptors (Ins(1,4,5) P_3 R) or ryanodine receptors (RyR) towards the cytosol. Calcium uptake under the consumption of ATP is mediated by the sarcoplasmic or endoplasmic reticulum calcium ATPase (SERCA) pump. As shown, mitochondria are in close proximity to the ER. Therefore, calcium released by the ER is taken up via voltage-dependent anion-selective channel proteins (VDAC) towards the intermembrane space. Mitochondrial calcium uniporter (MCU) mediating calcium transport towards the mitochondrial lumen. Furthermore, the ER has connections with the stromal interaction molecule 1 (STIM1), enabling calcium influx from the extracellular space after ER calcium depletion. Extracellular calcium is further taken up either via canonical transient receptor potential channels (TRPC) or plasma membrane calcium ATPases (PMCA). Finally, the intracellular calcium level also depends on transient receptor channel mucolipin receptor (TRPML) mediated currents from lysosomes. From Giorgi, Marchi and Pinton, 2018.

Another prominent cell organelle that is associated with intracellular calcium regulation is the mitochondrion (Slater and Cleland, 1953). The outer mitochondrial membrane is highly permeable to calcium, enabling influx to the intermembrane space (Figure 5). This largely depends on the expression of voltage-dependent anion-selective channel proteins (VDAC) (Messina *et al.*, 2012). Moreover, they build an interface between mitochondria and the ER, making calcium influx to the mitochondrion even more effective. The calcium influx over the inner mitochondrial membrane is mediated by the mitochondrial calcium uniporter (MCU). Hereby, mitochondria not only change the intracellular calcium concentration, but they are also affected by it. Furthermore, due

1. Introduction

to their nonstationary position within the lumen, they can shape cellular calcium responses in connection to their specific position.

More recently it was shown that lysosomes largely contribute to internal calcium homeostasis (Hirschi *et al.*, 2017). Here, calcium efflux is mediated by the transient receptor channel mucolipin receptor (TRPML) family (Figure 5). Lysosome calcium signalling was shown to be crucial for important cellular processes like organelle trafficking and fusion (Xu and Ren, 2015).

Lastly, a huge proportion of cellular calcium homeostasis is mediated by plasma membrane proteins (Figure 5). ER calcium depletion via Ins(1,4,5)P₃R triggers the activation of the calcium sensor protein stromal interaction molecule 1 (STIM1), which activates calcium release-activated calcium channel (CRAC) proteins (Deak *et al.*, 2014) like the calcium release-activated calcium channel protein 1 (ORAI1). In addition, canonical transient receptor potential channels (TRPC) mediate a calcium influx (Lee *et al.*, 2010). Finally, the cytosolic calcium level is kept at a constant low level through plasma membrane calcium ATPases (PMCAs) (Schatzmann, 1966).

In neurons these mechanisms are similar, although specific channel subtypes and ion concentrations may vary between cell types (Berridge, Lipp and Bootman, 2000). In general, the calcium concentration is elevated from around 100 nM up to several micromolar during neuronal activity (Bootman and Berridge, 1995). Since neurons fire APs during activity, a change in membrane potential, hereby activates voltage-activated calcium channels (Vierra and Trimmer, 2022).

Given these findings, which are far from being comprehensive, it becomes apparent how important experimental visualization of cellular calcium levels is to analyse cellular / neuronal activity. To enable this, scientists developed different ways to make the cellular calcium level accessible during live-cell experiments throughout research areas.

1. Introduction

1.4.1 The Cellular Calcium Signalling Toolkit

The first successful approach to directly monitor cellular calcium signals used an organic calcium sensor based on EGTA, a chemical with calcium chelating properties (Tsien, 1980). Over the years, calcium imaging was expanded to include many different experimental designs and samples: cell culture, brain slices and finally *in vivo* experiments in both anesthetized and awake animals. In the beginning, neurons in brain slices were loaded with calcium sensitive dye (Tsien, 1981). Here, a bolus injection of a membrane permeable calcium indicator dye, like for example fluo-4 (Gee *et al.*, 2000) or Oregon Green (White and McGeown, 2002), is applied to the tissue of interest. Membrane permeability is often achieved by using an acetoxymethyl ester form of a calcium-sensitive fluorochrome. After diffusion, the dye is hydrolysed within the cytosol by endogenous esterases. Excitation is mediated by a light source at a dye specific wavelength. The emitted fluorescence is detected by an optical system (Bootman *et al.*, 2013). The advantage of this approach, being easily applicable to many different preparations, comes at a certain cost: a lack of cell specificity.

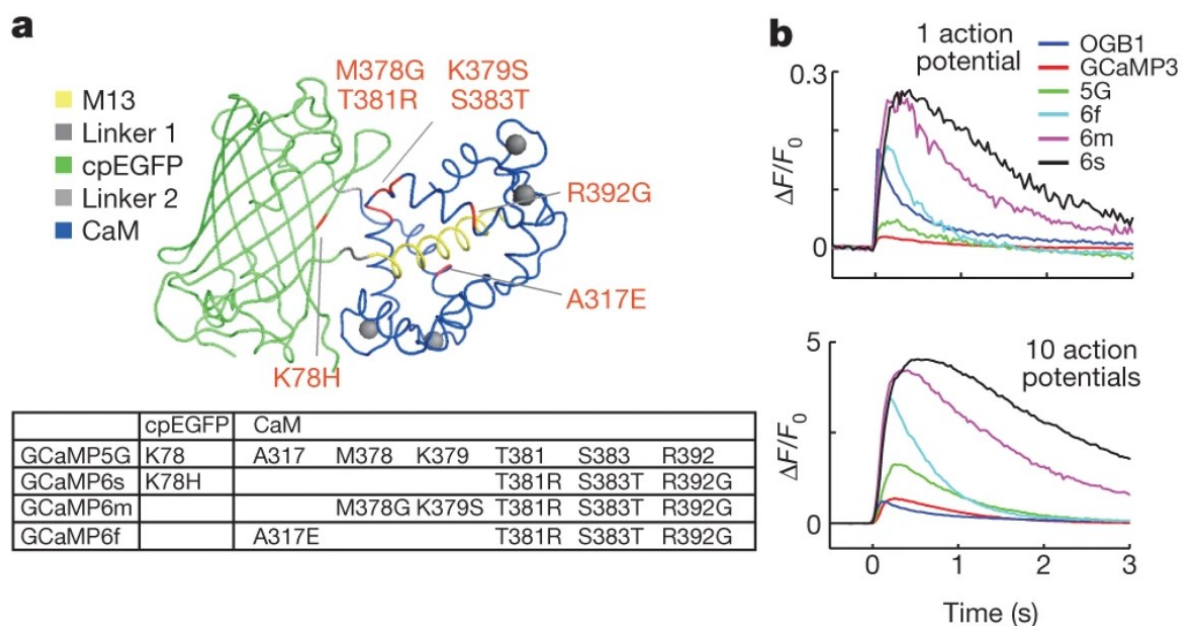


Figure 6: Mutagenesis of Different GCaMP Variants and Molecular Properties in Dissociated Neurons. **A:** Molecular structure of GCaMP and mutations in different GCaMP variants relative to GCaMP5G. Circular permuted enhanced green fluorescent protein (cpEGFP), Calmodulin (CaM) and the M13 peptide are the functional substructures. **B:** Fluorescence signals averaged across multiple neurons for GCaMP3, 5G, 6f, 6m, 6s and Oregon Green Bapta-1-AM (OGB1-AM). Top: Fluorescence changes in response to a single AP. Bottom: Fluorescence changes in response to 10 APs. APs were triggered by electrode stimulation. Note the superior signal after stimulation of GCaMP6 variants compared to older calcium dyes like OGB1-AM. From Chen *et al.*, 2013.

1. Introduction

To overcome this bottleneck, genetically encoded calcium indicators (GECIs) like GCaMP were engineered (Nakai, Ohkura and Imoto, 2001, Figure 6). GCaMP is a fusion protein based on green fluorescent protein (GFP), calmodulin (CaM) and the M13 peptide (Figure 6A). Combined with cell-specific genetic markers they offer superior signal-to-noise ratios and sensitivity, exclusively in the neuron population of interest. Since then, GECIs are constantly developed. They yield even better biophysical properties (Chen *et al.*, 2013; Dana *et al.*, 2019, Figure 6A) or exhibit modified emission and excitation wavelengths to enable multi-colour calcium imaging (Akerboom *et al.*, 2013).

Using these new, highly specific approaches it became possible to precisely monitor and analyse cellular calcium levels. One approach that is deduced from this toolbox is using the intracellular calcium level as a proxy for neuronal activity (Clapham, 2007). In neuroscience, this approach can be used to enable large-scale calcium imaging of cellular networks, both *in vitro* and *in vivo*.

1.4.2 Using Calcium Measurements to Study Neural Activity

To understand brain function on different levels neuroscientists developed a battery of techniques. These methods have different advantages and disadvantages that need to be considered when choosing the appropriate experimental design. As previously described, AMC oscillations were described on an electrophysiological level (Zylbertal *et al.*, 2015; Gorin *et al.*, 2016; Zylbertal, Yarom and Wagner, 2017). This technique gains detailed information about a single cell's activity, ion channel composition, as well as synaptic connections (Neher and Sakmann, 1976). To analyse and understand the activity of a neuronal network on large scales a different technique was developed: population live-cell calcium imaging.

GECIs, expressed in a neuronal population under control of a cell-specific genetic promoter, enable large-scale population analysis. Neurons fire APs to code information. An AP is a change in membrane potential characterized by rapid depolarization and recurrent repolarization. This change leads to opening of voltage-sensitive calcium channels, leading to an increase of cytosolic calcium concentration (Catterall, 2011). If a GECI, like GCaMP, is expressed within neurons and cytosolic calcium levels rise, GCaMP molecules will change their conformation upon binding of

1. Introduction

calcium to CaM. The change in conformation leads to a change in fluorescence intensity that is recorded, e.g., with a confocal laser scanning microscope, to gain spatially defined high-resolution images (Minsky, 1988). Doing so, modern GECIs like GCaMP6f enable single AP resolution up to 10 Hz (Hartung and Gold, 2020). Although these results are not applicable to all experimental conditions, trains of APs can be resolved and yield reliable responses (Mao *et al.*, 2008). These fluorescent signals, functioning as a proxy for APs and therefore cell activity, can be used to gain information about neuronal activity patterns. Due to relatively slow binding kinetics (several ms) of calcium dyes compared to the sampling frequency of whole-cell patch clamp experiments, however, calcium imaging data will always contain temporal uncertainty (Dana *et al.*, 2019). Mathematical methods like cross-correlations in combination with cluster algorithms can further be used to describe the temporal information coding of neuronal networks (Stringer and Pachitariu, 2019).

1. Introduction

1.5 Aims

The AOS is indispensable for most mammals to detect semiochemicals, ultimately leading to changes in animal behaviour and / or physiological state. Considering the relatively simple neuronal pathway that links pheromone detection by the VNO to stereotypic animal reactions, the AOB as the AOS first integration site is of particular importance. The exact coding mechanisms, enabling the extraction of semiochemical information, however, are still elusive. Especially the information coding strategy of AMCs, the AOB's main projection neurons, is barely understood.

Therefore, in this thesis I aim to apply an experimental toolbox consisting of *in vitro* and *in vivo* large-scale calcium imaging approaches, enabling observation of AMC network activity at single-cell resolution. Here, I will record intracellular calcium levels as a proxy for neuronal activity. Utilising Tbet-Cre x GCaMP6f mice will enable genetically restricted expression of the sensitive calcium indicator GCaMP6f exclusively in AMCs. Experimentally, *in vitro* calcium imaging in acute brain slices will enable pharmacological dissection of functional AOB network connectivity. In addition, *in vivo* calcium imaging in AMCs will, for the first time, provide insights into AMC calcium fluctuations in the living animal.

Analysing AMC network activity at single-cell resolution will shed light on possible physiological subtypes of neuron populations. Furthermore, I aim to decipher coding mechanisms on network level, like formation of sub-network ensembles in the AOB. Here, I will utilise state-of-the-art clustering algorithms to detect possible orchestrated AMC network activity. Analysing AOB network activity and connectivity, combining *in vitro* and *in vivo* calcium imaging techniques, will give important insights into AOS coding capacity. I will extend the knowledge about AMC physiology, coding strategies in the AOB and possible influences of e.g. top-down modulation, which can only be addressed in the intact AOS of living animals.

2. Materials & Methods

2.1 Materials

2.1.1 Equipment

Microscope DM 6000 CFS – TCS SP8	Leica Microsystems
Microscope DM 6000 CFS - TCS SP5	Leica Microsystems
Mai Tai HP 1040S	Spectra-Physics
Binocular SF4	Leica Microsystems
Binocular light source L2	Leica Microsystems
Binocular S6E	Leica Microsystems
Binocular SMZ-168	Motic
Dental Drill K.1070, 0.6mm drill	Freedom
Dumont SS Fine Forceps (11200-33)	Fine Science Tools
Flexible in vivo stage for Leica SP8	Luigs&Neumann
Forceps with replaceable plastic tips	Fine Science Tools
Form 3 3D Printer	formlabs
Iris Forceps (11064-07)	Fine Science Tools
Micro scales XA105 dual range	Mettler Toledo
Microscope CCD camera DFC 360 FX	Leica Microsystems
Microscope CCD camera DFC 365 FX	Leica Microsystems
Objective $\infty/0$ HC AP0 L 20x/1.00 W	Leica Microsystems
Objective $\infty/-/A$ N PLAN 5x/0.12	Leica Microsystems
Objective $\infty/0/D$ HC FLUOTAR L 25x/0.95 W VISIR	Leica Microsystems
Optical table	TMC Linos
Osmometer osmomat 030	Gonotec
Perfusion system 8-in-1	AutoMate Scientific

2. Materials & Methods

pH Meter five easy	Mettler Toledo
pH electrode InLab routine (for solutions)	Mettler Toledo
PID Thermocontroller cTRON 16 (467-080)	Jumo
Resistance thermometer PT100 (285-661)	RS Components
Scale	Tristar
Silicon heating pad 7.5W (245-556)	RS Components
Stirring plate Cimarec i	Thermo Fisher Scientific
Thermal Cycler T100	Bio-Rad
Trigger interface TIB 14S	HEKA Elektronik
Vibrotom VT1000S	Leica Microsystems
Water bath JB Nova	Grant Instruments

2.1.2 Chemicals

Acetic acid	VWR
Bucain 7.5 mg/ml	Puren Pharma GmbH&Co. KG
Calcium chloride	Sigma-Aldrich
Carbogen (5% CO ₂ + 95% O ₂)	Gaseportal
Carbon dioxide	Gaseportal
D-AP5	Abcam / Tocris
D-(+)-Glucose	Sigma-Aldrich
Deoxyribose nucleoside triphosphates	Sigma-Aldrich
DirectPCR®-Ear	VWR
DirectPCR®-Tail	VWR
D-Sucrose	VWR
Ethanol	Diagonal

2. Materials & Methods

Gabazine	Abcam
GelRed	Biotium
GeneRuler 1kb Plus	Thermo Fisher Scientific
GoTaq® G2 Flexi DNA Polymerase	Promega
Hydrochloric acid	AppliChem
Magnesium chloride hexahydrate	Sigma-Aldrich
Magnesium sulfate	AppliChem
NaCl 0.9%	B. Braun
Narcoren 16g/100 ml	Boehringer Ingelheim
NBQX disodium salt	Abcam / Tocris
Potassium chloride	Sigma-Aldrich
peqGold low melt agarose	VWR
peqGold universal agarose	VWR
Protein kinase K	VWR
Rimadyl 5mg/kg	Zoetis
Sodium dihydrogen phosphate	Sigma-Aldrich
Sodium hydrogen carbonate	Sigma-Aldrich
Sodium hydroxide	AppliChem
Tris (1 M), pH 8.0	Thermo Fisher Scientific
2-[4-(2- hydroxyethyl)piperazin-1-yl]ethanesulfonic acid (HEPES)	VWR
2,2',2'',2'''-(Ethane-1,2-diyl dinitrilo)tetraacetic acid (EDTA)	AppliChem

2. Materials & Methods

2.1.3 Consumables

Cutting blades	Wilkinson
Cell culture dishes (145 x 20 mm)	Falcon
Eppendorf tubes 0.5 ml	Eppendorf
Eppendorf tubes 50 ml	Eppendorf
Gloves gentle skin sensitive	Meditrade
Pasteur pipettes	VWR
Syringe BD Plastipak	Becton Dickinson
Solution Filter 0.2 µm	VWR
Gelatin sponge	SMI Spon
Tuberculin syringe 1ml	Teqler
Tissue glue	Surgibond
Blunt needle G21, 0.8x22mm	Sterican
Microprism 1.5 mm (4531-0023)	Tower Optical
Blu Tack adhesive gum	Bostik
Bepanthen eye- and nose cream	Bayer Vital GmbH
Clear Resin	formlabs

2. Materials & Methods

2.1.4 Primer

Table 1: Primer and Supplier

Primer	Supplier
GCaMP6f forward (ACG AGT CGG ATC TCC CTT TG)	Thermo Fisher Scientific
GCaMP6f reverse (CCG AAA ATC TGT GGG AAG TC)	Thermo Fisher Scientific
Tbx21-cre1 forward (AGA GAA AGC CCA GGA GCA G)	Thermo Fisher Scientific
Tbx21-cre1 reverse (CAT GTC CAT CAG GTT CTT GC)	Thermo Fisher Scientific

2.1.5 Solutions

Table 2: S1 - Bicarbonate buffered oxygenated extracellular artificial cerebrospinal fluid.

Chemical	Concentration [mM]
Sodium chloride	124
Potassium chloride	3
Sodium hydrogen carbonate	26
Glucose	10
Calcium chloride	1.3
Magnesium sulfate	1.3
Sodium dihydrogen phosphate	1.25

Osmolarity was adjusted to 300 mOsm using 0.18g glucose per missing mOsm. Oxygenation was established and pH (7.3) was adjusted using carbogen (95% O₂ / 5% CO₂).

2. Materials & Methods

Table 3: S2 - Sucrose-based bicarbonate-buffered oxygenated artificial cerebrospinal fluid.

Chemical	Concentration [mM]
Sucrose	220
Sodium hydrogen carbonate	26
Glucose	10
Potassium chloride	3
Sodium dihydrogen phosphate	1.25

Osmolarity was adjusted to 300 mOsm using 0.18g glucose per missing mOsm. Oxygenation was established and pH (7.3) was adjusted using carbogen (95% O₂ / 5% CO₂).

Table 4: S3 - HEPES-buffered non-oxygenated extracellular solution.

Chemical	Concentration [mM]
HEPES	10
Sodium chloride	145
Potassium chloride	5
Calcium chloride	1
Magnesium chloride	1

pH was adjusted to 7.3 using sodium hydroxide. Osmolarity was adjusted to 300 mOsm using 0.18g glucose per missing mOsm.

2. Materials & Methods

Table 5: S4 - Elevated potassium extracellular solution.

Chemical	Concentration [mM]
Potassium chloride	50
Sodium chloride	100
HEPES	10
Calcium chloride	1
Magnesium sulfate	1

pH was adjusted to 7.3 using sodium hydroxide. Osmolarity was adjusted to 300 mOsm using 0.18g glucose per missing mOsm.

Table 6: S5 - Polymerase chain reaction mix.

Chemical	Concentration
Buffer for GoTag-Polymerase	1x
Deoxyribose nucleoside triphosphates	0.2 mM
Magnesium chloride	1.5 mM

Table 7: S6 - Tris-Acetate-EDTA buffer.

Chemical	Concentration [mM]
Tris (1 M), pH 8	40
Acetic acid	20
EDTA	1

2. Materials & Methods

Table 8: S7 - HEPES-buffered non-oxygenated extracellular solution including pharmacological inhibitors.

Chemical	Concentration
Sodium chloride	145 mM
Potassium chloride	5 mM
HEPES	10 mM
Calcium chloride	1 mM
Magnesium chloride	1 mM
<hr/>	
<i>either:</i>	
AP5	100 μ M
Gabazine	10 μ M
NBQX	10 μ M

pH was adjusted to 7.3 using sodium hydroxide. Osmolarity was adjusted to 300 mOsm using 0.18g glucose per missing mOsm.

2.1.6 Animals

All animal procedures were performed under the approval of local authorities and the European Union legislation for animals used for scientific purposes (Directive 2010/63/EU). Furthermore, we followed recommendations of the Federation of European Laboratory Animal Science Associations (FELASA). The animals were housed in groups of both sexes on a 12-hour light-dark cycle with water and food *ad libitum*. Adult mice of either sex were used for the experiments in line with the according animal experimentation license. Only mice from the C57BL/6 strain were used.

2.1.7 Genotyping

We genotyped each animal that was used for either *in vitro* or *in vivo* experiments. After weaning, ear tags were taken and lysed in 200 μ l of DirectPCR®-Ear and 2 μ l protein kinase K for 12-16 hours at 55°C. We stopped the lysis by heating all samples for 1 hour at 85°C.

2. Materials & Methods

Table 9: PCR protocol for genotyping of mouse ear tags. We repeated steps 2-4 35 times and used S5. For primers see 2.1.4.

Step	Temperature	Duration
1. Denaturation	95°C	5 min
2. Denaturation	95°C	30 s
3. Annealing	61°C	30 s
4. Elongation	72°C	45 s
5. Elongation	72°C	10 min
6. Storage	4°C	∞

The expected fragment size was ~300bp for Tbet and ~450bp for GCaMP6f. Because of their comparable product size, we analysed both targets in one PCR approach. We analysed both PCR products by gel electrophoresis using 1% agarose dissolved in S6 and GelRed. We set the power supply initially to 80V for 15 minutes and later to 120V for 30 minutes.

2.1.8 Software

Corel Draw Graphics Suite 2019	Corel Corporation
ImageJ 1.51n & 1.53c (FIJI)	NIH Image
Microsoft Office	Microsoft Corporation
Python 3.6.0 (Spyder 3.1.2)	Python Software Foundation
Leica LAS AF	Leica Microsystems
Leica LAS X	Leica Microsystems
Igor Pro 9	Wavemetrics
MATLAB R2021a	Mathworks
Suite2p 0.7.2	HHMI Janelia Research Campus

2. Materials & Methods

2.2 Methods

2.2.1 Surgical Procedures

2.2.1.1 Acute Accessory Olfactory Bulb Brain Slice Preparation

We sacrificed young adult Tbet-Cre x GCaMP6f mice by decapitation after brief exposure to CO₂. We removed the jawbone and the skin of the skull. The bone of the dorsal skull was thinned between the eye sockets by gentle scraping using a scalpel. Afterwards, we removed the anterior dorsal skull and performed a bilateral craniotomy, gaining access to the mouse brain. After removing the brain, we separated the olfactory bulb from the forebrain using a scalpel. We separated both bulbs and embedded them in pre-heated (42°C) 4% peqGold low melt agarose (dissolved in S3). During the whole preparation procedure, the brain was kept in ice-cold S2.

Using a Leica VT1000S vibratom, each bulb was cut in 250 µm thin sagittal acute brain slices using the following settings:

Speed:	3.5 AU
Frequency:	5.5 AU
Amplitude:	Position 3

During the whole cutting procedure, the tissue was always stored in ice-cold S2. Acute brain slices were stored until experimental use in S1 in darkness at room temperature. Prior to experiment, we allowed tissues a recovery time of at least 1 hour.

2. Materials & Methods

2.2.1.2 Optical Exposure of the Accessory Olfactory Bulb *In Vivo*

For *in vivo* two-photon calcium imaging of the AOB we used 3-6 months old Tbet-Cre x GCaMP6f mice of either sex. We initially anaesthetised mice using pentobarbital (40mg/kg body weight). To maintain deep anaesthesia, we injected 20% of the initial pentobarbital dose throughout the experiment when needed. Deep anaesthesia was confirmed by testing the toe-pinch reflex. For analgesia, we injected carprofen (5mg/kg bodyweight). Before skin incision, the targeted area was anaesthetised using bupivacaine (1%). We applied physiological saline subcutaneously (0.07ml NaCl 0.9%/20g bodyweight) to maintain fluid and electrolyte balance. We did not exceed the recommended maximum amount of fluid application from 1 ml/kg/h. To maintain body temperature, we kept the animal on a silicon heating pad at 37°C. We prevented the eyes from running dry by applying Bepanthen eye and nose cream.

Prior to skin incision, we shaved the head of the mouse to prevent contamination by body hair. Afterwards, we opened the skin using sharp scissors gaining access to the animal's skull. Gently scratching the skull with sharp forceps, we removed the remaining skin on the skull to prepare for a unilateral craniotomy. Using a dental drill, we gently thinned the bone above a large blood vessel between olfactory bulb and forehead. Here, we made a punctual incision into the bone on the lateral and medial side. Having the skull above the blood vessel thinned, we inserted adhesive gum glue through the drilled hole using sharp forceps to block the blood vessel. After this, we performed a unilateral craniotomy above the olfactory bulb and the cortex using a dental drill. Afterwards, we gently removed the dura matter with a bent sharp needle from the cortex. This enables us to remove 1.5 x 1.5 mm of cortex tissue by negative pressure using a blunt needle. This step is crucial, since excessive bleeding by blood vessels of the mouse brain needs to be prevented. Any potential bleeding was stopped using gelatin sponge. After successfully removing cortex tissue we inserted the 1.5 x 1.5 x 1.5 mm aluminium coated glass microprism which is mounted in a custom build 3D printed prism holder. After mounting the microprism to the holder, it was carefully inserted into the mouse head with gentle pressure towards the backside of the olfactory bulb. This prevented any fluid, like blood, between the microprism surface and brain tissue, that eventually could have restricted our optical access. Lastly, we glued the microprism holder to the remaining skull using tissue glue, preventing any movement during two-photon recordings.

2. Materials & Methods

2.2.2 Data Acquisition

2.2.2.1 *In Vitro* Data Acquisition

For *in vitro* AMC calcium imaging we transferred the acute brain slices of Tbet-Cre x GCaMP6f mice (see 2.2.1.1) to a custom-made slice chamber. We fixated the tissue using a slice anchor to prevent movement during imaging. For data acquisition we used a Leica DM 6000 CFS – TCS SP5 confocal microscope. The microscope was equipped with a Leica HC AP0 L 20x/1.00 W objective. The fluorescent images were recorded by a DFC 360 FX CCD camera and stored using the software Leica LAS X AF. The fluorescent calcium indicator GCaMP6f was excited using an argon laser at 488 nm. The laser intensity was adapted for each experiment to always use the dynamic range of the Leica Hybrid Detector in the best possible way.

Using the confocal microscope, we made sure to only collect fluorescent signal from a narrow optical z-plane. Doing so, we prevented possible strong cross-contamination from the fluorescence signals of AMCs above or below the cells of interest. Adjusting the pinhole aperture enabled us to restrict the optical z-section to 5-10 μm . The pinhole was adjusted in each experiment for the best possible signal-to-noise ratio. Fluorescent light was collected and detected by a photomultiplier.

All experiments were performed using the following microscope settings:

Excitation wavelength:	488 nm
Detector:	Leica Hybrid Detector (HyD)
Dichroic mirror:	TD 488/543/633
Image resolution:	1024x512 pixels
Recording frequency:	1 Hz
Scanning frequency:	300 Hz (Bidirectional X scanning)

Zoom and scan field rotation was adapted as needed for each recording. Ensuring best signal-to-noise ratio, we adjusted pinhole size between 3 to 13.5 AU and set the laser intensity between 10 to 24%. For each experiment we confirmed AOB histology taking a differential interference contrast image.

2. Materials & Methods

During physiological measurements, acute brain slices were constantly perfused in the recording chamber (using S1) and via the perfusion pencil (S3). Bath perfusion was gravity-driven. Perfusion via the perfusion pencil was controlled by gentle air pressure. Switching between the physiological standard solution (S3) and inhibitor solutions (S7) was controlled by a HEKA TIB 14S trigger interface.

The measurements under control conditions were performed over a duration of 20 minutes. For inhibitor experiments, we used the following recording paradigm over 33 minutes:

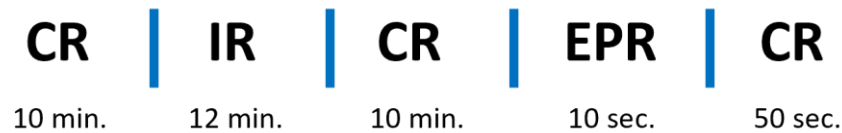


Figure 7: Recording Protocol for *In Vitro* Calcium Imaging Inhibitor Experiments. CR: control recording (S1+S3), IR: inhibitor recording (S1+S7), EPR: elevated potassium recording (S1+S4).

We first performed a 10-minute control recording (CR) to capture resting state activity. For CR we applied S1 via bath application and S3 via the perfusion pencil. Afterwards, a 12-minute period of inhibitor recordings (BR) followed. For this, we used S1 via the bath perfusion and S7 via the perfusion pencil. From this 12-minute period the first 2 minutes were used as equilibration time for the applied inhibitor. The remaining 10 minutes were used as a period for analysing. Hereafter, we again added a 10-minute CR with S1 via batch application and S3 via the perfusion pencil.

To reveal neurons that did not show any activity throughout the recording we applied an elevated potassium (EPR) stimulus (S4) for 10 seconds to depolarise silent, but vital neurons. After this, we again recorded a 50 second CR.

2. Materials & Methods

2.2.2.2 *In Vivo* Data Acquisition

After establishing optical access to MCL (see 2.2.1.2), we positioned the deeply anaesthetised Tbet-Cre x GCaMP6f mouse on a Luigs&Neumann In Vivo Stage and placed the animal under a DM 6000 CFS – TCS SP8 microscope. For overview images verifying AOB location, we used a Leica ∞ -/-A N PLAN 5x/0.12 objective. Here, for image acquisition, we used a Leica DFC 365 FX CCD camera. The fluorescent calcium indicator GCaMP6f was then excited using a Spectra-Physics Mai Tai HP 1040S two-photon laser at 930 nm. Laser intensity was adjusted for every experiment to ensure using the full dynamic range of the Leica hybrid detectors. We collected both GCaMP6f fluorescence emission and tissue background fluorescence to correct for movement artifacts. The image resolution was adapted to the field of view changing between 512x512 and 1024x512 pixels.

Using two-photon microscopy we achieved high tissue penetration depth due to the longer wavelength used for excitation compared to single-photon imaging. All *in vivo* imaging experiments were performed using the following settings:

Excitation wavelength:	930 nm
Detector:	Leica hybrid detector (HyD)
Image resolution:	512x512 or 1024x512
Recording frequency:	0.58 Hz, 1.15 Hz, 2.3 Hz or 4.55 Hz
Scanning frequency:	600 Hz (Bidirectional X scanning)

Zoom and scan field rotation was adapted as needed for each recording to ensure best neuron yield. The recording time varied between 5 to 31 minutes.

2. Materials & Methods

2.2.3 Data Analysis

2.2.3.1 *In Vitro* Data Analysis

2.2.3.1.1 Movement Correction

First, we performed a movement correction for x and y movement if necessary. Depending on movement type we either used a rigid body correction (ImageJ 1.51n) or a hidden Markov 2D model (sima motion correction, spyder 3.1.2, Dombeck *et al.*, 2007).

2.2.3.1.2 Data Extraction

After removing movement from the data, we extracted raw data traces using FIJI. Here, we extracted mean grey values from regions-of-interests (ROIs) for somata identified by elevated potassium (S4) stimulation. In addition, we drew an additional background ROI around each soma to correct for background/neuropil fluorescence. ROI mean grey values and center of mass were extracted. We subtracted background fluorescence from somatic calcium signals. Furthermore, we corrected for fluorescence dye bleaching using the MatLab function 'detrend'. All analysis steps were performed using custom-written software in MatLab. We thank Prof. Dr. Yoram Ben-Shaul for data analysis support.

2.2.3.1.3 Oscillation Analysis

AMC calcium signals *in vitro* were classified as either oscillating or non-oscillating. We used two measures for this: autocorrelation as a measure for rhythmicity and power spectral density to detect strong frequency peaks in the infraslow range. The following parameters were used for the analysis of 10-minute recordings:

For calculation of the autocorrelation, we used the MatLab function 'xcorr' with the following settings:

Maximum lag allowed:	100 seconds
Normalization option:	'coeff'

2. Materials & Methods

If we could detect a pronounced side trough in the autocorrelation between a lag of 30-100 seconds with a value lower than the autocorrelation value at lag -100 seconds, the activity was classified as rhythmic.

For spectral analysis we used the MatLab function 'pwelch'. We removed the DC signal of the power spectrum. The frequency was normalized the following:

$$\text{Normalized frequency} = \left(\frac{\text{Frequency}}{\pi} \right) * \left(\frac{\text{Sampling Frequency}}{3} \right)$$

We analysed frequencies from 0.01 – 0.3 Hz. If a frequency bin in this frequency range exceeded a power of 7 it was classified as oscillating. This criterion was true for AMC signals with a maximum mean grey value above 1.5.

Only if both criteria, autocorrelation and power spectral density, were true, the AMC was classified as oscillating. If the maximum mean grey value of the recording was below 1.5, we only used the autocorrelation criterion as measure to be an oscillating AMC.

Autocorrelation and power spectral density values depend on the analysed time window duration. If we wanted to classify AMCs based on a recording different from 10 minutes, we used a machine learning algorithm to objectively apply those measures objectively to different recording lengths. Here, we used a quadratic support vector machine with 5-fold cross-validation and 0.7 box constraint level.

2. Materials & Methods

2.2.3.1.4 Microcircuit Analysis

For microcircuit clustering we used cross-correlations as a measure for connectivity. We assumed that correlated activity of AMC calcium signals within a lag of ± 5 seconds indicates correlated neural activity, and therefore possible synaptic coupling. To validate this, we calculated the maximum positive correlation coefficient within the ± 5 second lag. To calculate cross-correlations, we used the MatLab function 'corrcoef' and normalized the cross-correlation values between -1 and 1. As input to the function we used a sliding window approach using 5-minute signal periods with a shift of 60 seconds for each time window. These 5-minute time windows were classified as oscillating or non-oscillating using the machine learning algorithm previously described (see 2.2.3.1.3).

Mathematically, signal correlation inherently reveals a certain degree of correlation. To only analyse cross-correlations that are higher than expected by chance (i.e., according to a normal distribution of random correlation coefficients), we needed a classification for significantly correlated AMCs. Therefore, we plotted all AMC pair maximum positive cross-correlation coefficients for all experiments and each time window. Then, we fitted a gaussian distribution to the left-side slope and peak of this distribution. For this population, we calculated the 95% confidence interval of the Gaussian fit and used it as a threshold for every time window. Every cross-correlation coefficient higher than this value indicated a significantly correlated AMC pair. We performed this thresholding for each experimental population: control conditions and the control measurements of the three different inhibitor conditions. The thresholds defined here were transferred to the cross-correlation populations for inhibitor conditions for pharmacological experiments.

Then, we clustered the oscillating AMCs by correlation coefficients above threshold. Each AMC within a cluster was correlated above threshold with all others. We defined a microcircuit as the largest mutually exclusive unique combination of AMCs found within one experiment. One AMC can thus be part of more than one microcircuit.

2. Materials & Methods

2.2.3.2 *In Vivo* Data Analysis

2.2.3.2.1 Movement Correction

The quality of *in vivo* calcium imaging experiments can suffer from movement artefacts caused by breathing and heartbeat of the animal. To remove these movement artefacts in x and y direction we used the software suite2p 0.7.2 from the Howard Hughes Medical Institute (Pachitariu *et al.*, 2017). Movement correction was only performed if necessary.

2.2.3.2.2 Data Extraction

After removing movement from the *in vivo* calcium recordings, we drew ROIs around the somata of active AMCs. ROIs were again hand-drawn to ensure exclusively analysing active and vital AMCs. In line with *in vitro* calcium imaging recordings, we drew a surrounding ROI to correct for possible background signal contamination. To further increase the signal-to-noise ratio we performed a three-point centered moving average of the raw data using the MatLab function 'smoothdata' and its smoothing method 'movmean'.

2.2.3.2.3 Peak Detection

Since we performed AMC calcium imaging *in vivo* for the first time, we aimed to classify the properties of AMC calcium signals. Furthermore, we searched for different neuron populations based on their physiology. Therefore, we needed to develop a peak detection that is suitable for our data. Lacking a reliable commercial / open-source peak detection algorithm suitable for our calcium imaging data, we performed a semi-automated custom-written peak detection in MatLab. Here, we divided between AMCs that showed either a fast or a slow activity pattern.

First, we manually selected the baseline signal of each analysed AMC. The peak detection itself was based on the MatLab function 'findpeaks'. For fast active AMCs we defined noise as the 0.75x standard deviation of the whole recording. We defined the 'MinPeakHeight' to be at least the selected baseline plus 0.75x standard deviation. Furthermore, we set the 'MinPeakDistance' to 2x the sampling frequency of the recording. Doing so, we could apply the peak detection for recordings with different recording frequency.

2. Materials & Methods

For slow active AMCs we did not only define the noise baseline value manually, but we also defined the minimum duration of one up-state. This information was again forwarded to the MatLab function 'findpeaks'. The 'MinPeakHeight' was again defined as 0.75x standard deviation. The parameter 'MinPeakDistance' was set to the minimum up-state duration that was previously defined manually.

In addition, each analysis was manually verified, i.e., if peak detection flagged obvious false positives or 'missed' false negatives we corrected this *post-hoc*.

2.2.3.2.4 Measurement of Peak Kinetics

The parameter full width at half maximum was calculated using the inbuilt function of the MatLab 'findpeaks' function. Furthermore, we defined time-to-peak. Here, we defined the starting point of each signal's slope by calculating the turning point from the baseline defined for each signal. We then calculated the time from this turning point to the peak detected by the function 'findpeaks'. From each peak's time point we then calculated the autocorrelation, as a measure for rhythmicity, and the inter-event times. The autocorrelation was, in line with our *in vitro* analysis, calculated using the MatLab function 'xcorr'. Spectral analysis was performed by calculating power spectral densities for every AMC using the MatLab function 'pwelch'. We removed the DC signal from the power spectral density using a digital band-pass filter, which was designed with the kind support of Dr. Thomas Künzel:

MatLab function:	designfilt
Lowpass cutoff:	0.99 (in fractions of Nyquist frequency)
Highpass cutoff:	0.007 (in fractions of Nyquist frequency)
'StopbandAttenuation1':	65
'PassbandRipple':	0.5
'StopbandAttenuation2':	65
'DesignMethod':	'cls'

2. Materials & Methods

The frequency was normalized the following:

$$\text{Normalized frequency} = \left(\frac{\text{Frequency}}{\pi} \right) * \left(\frac{\text{Sampling Frequency}}{3} \right)$$

2.2.3.2.5 Correlation Analysis

To check for correlated calcium activity between AMCs *in vivo* we calculated cross-correlations between every active cell in a given experiment. To calculate these values, we used the MatLab function 'corrcoef' and normalized the cross-correlation coefficients between -1 and 1. We used a sliding window approach, analysing 5-minute periods always shifted by 60 seconds. We plotted the highest positive cross-correlation coefficient.

3. Results

The experiments we performed aimed to extend our knowledge of AOB information coding, especially of the role of intracellular calcium fluctuations in AMCs. To gain a deeper understanding of AMC network activity we performed large-scale calcium imaging experiments, both *in vitro* and *in vivo*.

In vitro acute brain slice calcium imaging is a well-established approach to monitor cellular activity (Grienberger and Konnerth, 2012), allowing not only to monitor resting state conditions, but also to apply pharmacological agents. However, this approach cannot be used to quantify the effect of natural sensory stimulation of the AOS.

The *in vitro* data shown here has partly been published in Tsitoura, Mohrhardt, Malinowski *et al.*, 2020. All data shown in this thesis has been acquired and analysed by me.

Analysing AMC calcium fluctuations *in vivo*, when all bottom-up and top-down AOS connectivity is intact, has not been possible before. In my work, I established an experimental approach using glass microprisms to perform large-scale calcium imaging at cellular resolution in the AOB in the living animal for the first time.

3.1 AOB Mitral Cell Calcium Activity *In Vitro*

We used an *in vitro* approach in acute sagittal slices of the AOB to analyse AMC activity on a population basis on long time scales. The different layers of the AOB are clearly discernible in differential interference contrast microscopy images (Figure 8A). GL and LOT appear darker than the MCL, making the area of interest easy to target. Furthermore, we used a perfusion pencil (PP) to apply pharmacological agents. This enabled modulation of the AMC network with different inhibitory drug solutions (S7).

To selectively label AMCs we used Tbet-Cre x GCaMP6f mice (Figure 8B). The Tbet promotor allows selective labelling of AMCs (Haddad *et al.*, 2013, Figure 8B, Figure 8Ci-Cii). GCaMP6f was expressed under the Tbet promotor in AMCs and showed fluorescence intensities depending on intracellular calcium levels (Chen *et al.*, 2013), which we used as a proxy for cellular activity (Clapham, 2007). Fluorescence was recorded using a single photon confocal microscope (Leica SP5) at 20x magnification.

3. Results

The intracellular calcium level is largely influenced by membrane depolarisation. Applying elevated potassium solution (S4) allows visualization of all AMCs in a physiological state by shifting the membrane potential to more positive values. As shown, the MCL is densely packed with fluorescent neurons (Figure 8B).

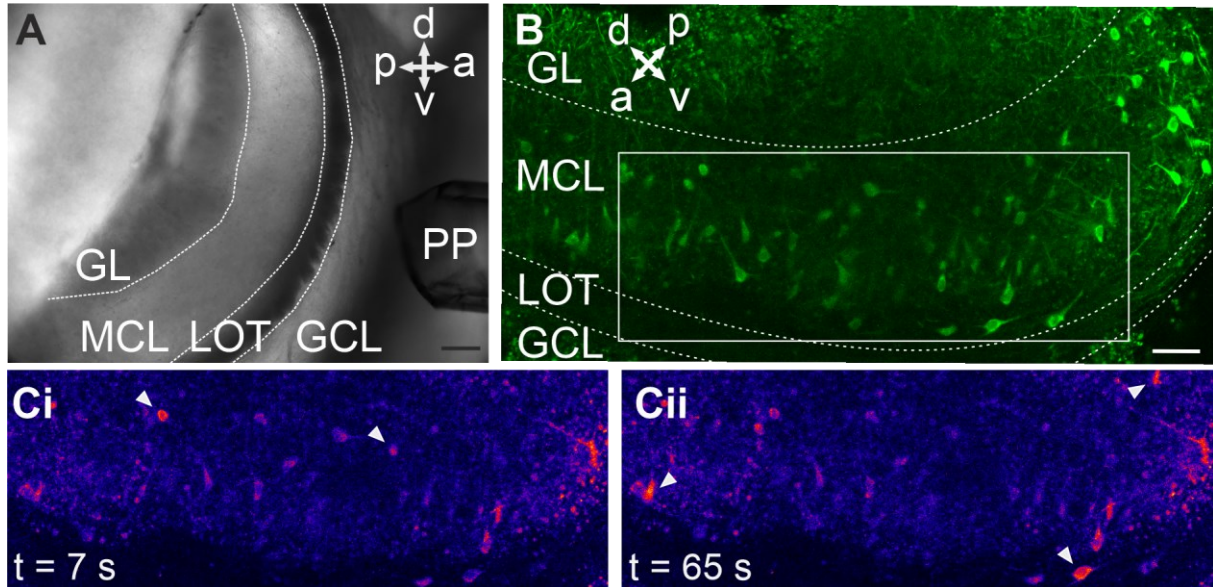


Figure 8: Experimental Setup for Confocal Large-Scale Calcium Imaging in Acute AOB Slices *In Vitro*. **A:** Differential interference contrast microscopy image of a sagittal AOB section. Note the layered AOB structure. Scale bar: 100 μm . a: anterior; v: ventral; p: posterior; d: dorsal. PP: perfusion pencil, 250 μm diameter. GL: glomerular layer; MCL: mitral cell layer; LOT: lateral olfactory tract; GCL: granule cell layer. **B:** Maximum projection (20-frames average) of GCaMP6f fluorescence during elevated potassium (S4) application. Individual AMC somata in the MCL are clearly discernible. Tbet-Cre x CGaMP6f mouse, green pseudocolor. Scale bar: 50 μm . **C:** Two different time points **Ci** (7s) and **Cii** (65s) of a representative recording. Zoom-in from white box in **B**. Note the different calcium transients in different neurons, indicated by the white arrows. Adapted from Tsitoura *et al.*, 2020.

While monitoring calcium-induced changes in fluorescence intensity over a time frame of 33 minutes, spontaneous calcium fluctuations were visible in a large portion of AMCs (Figure 8Ci, Figure 8Cii). The fluorescence intensity of distinct somata in the MCL clearly varied between the images taken at 7 and 65 seconds.

3.1.1 Spontaneous Calcium Activity in AOB Mitral Cells

Prolonged (33 min) monitoring of intracellular calcium concentration revealed that the vast majority of AMCs display spontaneous calcium fluctuations at resting conditions (Figure 9A). These spontaneous fluctuations can be classified into two distinct patterns: either signals fluctuated irregular (Figure 9A, red trace), or they showed a reoccurring, oscillatory behaviour (Figure 9A, blue traces). This observation was in line

3. Results

with previous electrophysiological observations (Gorin *et al.*, 2016). Finally, some AMCs did not show spontaneous discharge (Figure 9A, black trace). This AMC population was identified by application of elevated potassium solution (S4) for 10 seconds via the AP (Figure 9A, grey shaded areas).

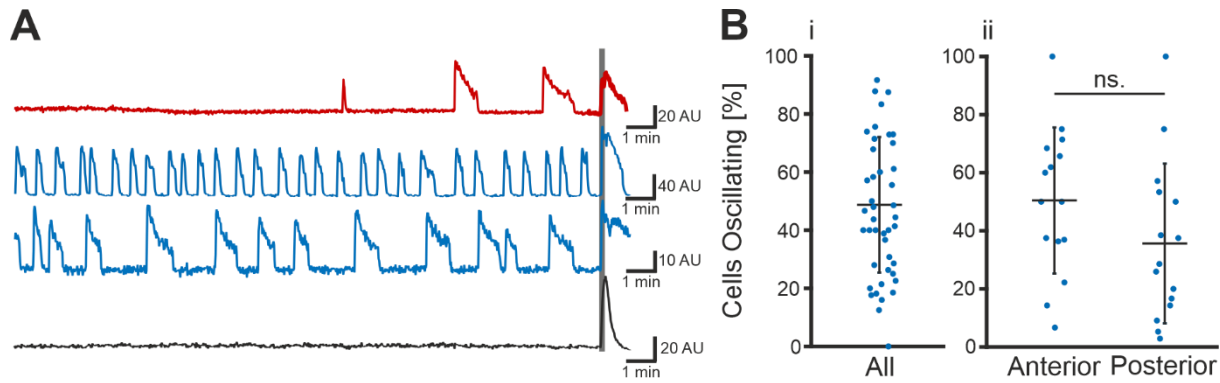


Figure 9: Spontaneous Calcium Activity of AMCs In Vitro. **A:** Representative original calcium signal recordings of fluorescence intensity from four different AMCs over time: Intensity measured in artificial units (AU). The traces either show irregular (red) or periodic (blue) activity. Some AMCs are silent (black). Depolarization based on elevated potassium (S4) proves AMC viability (grey shaded area). **B:** Percentage of AMCs showing spontaneous oscillatory activity. **Bi:** Percentage of AMCs showing oscillating calcium transients. Note the large spread of oscillating AMC fractions. One blue dot indicates one slice experiment. $48.7 \pm 23.3\%$ (mean \pm standard deviation). **Bii:** Like **Bi**, subdivided into anterior and posterior fractions. No significant difference is detected between anterior and posterior AOB. Anterior: $50.4 \pm 25.1\%$, posterior: $35.6 \pm 27.5\%$. Kolmogorov-Smirnoff test is used to test for normal distribution. Wilcoxon rank-sum test is used to test for significance. Adapted from Tsitoura *et al.*, 2020.

Oscillatory behaviour (Figure 9A, blue traces) was observed in around half of all analysed AMCs ($48.7 \pm 23.3\%$, Figure 9Bi). Although the mean indicated that nearly 50% of all AMCs showed this physiological phenomenon, the large standard deviation indicated a highly heterogeneous distribution across measurements. The same was true after subdividing AMCs according to their location within the AOB. Both anterior and posterior AMCs frequently displayed oscillations (anterior: $50.4 \pm 25.1\%$, posterior: $35.6 \pm 27.5\%$, Figure 9Bii). However, they did not show significant differences as a function of anatomical location (Figure 9Bii, Wilcoxon rank-sum test). Furthermore, heterogeneity was comparable between the groups. This indicates that innervation by different VSN classes (i.e., V1R- or V2R-positive) did not affect AMC oscillations along the anterior-posterior AOB axis.

3. Results

3.1.2 Rhythmic AOB Mitral Cell Discharge

The categorization into irregular active and oscillatory AMC populations was based on rhythmicity and frequency analysis. Here, we used autocorrelations as a measure for temporal rhythmicity, and power spectral density (PSD) analysis as a measure in the frequency domain (Figure 10).

Autocorrelation of irregularly active AMCs typically only showed a prominent peak at zero lag (Figure 10Ai). Shifting the signal overlay to either positive or negative lags

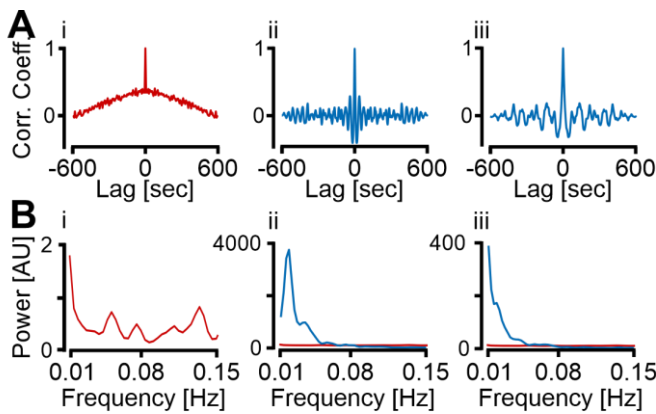


Figure 10: Autocorrelation and Power Spectra of AMCs In Vitro. **A:** Autocorrelation from traces in Figure 9A. **Ai:** Autocorrelation of an irregular bursting AMC from Figure 9A (red trace). **Aii, Aiii:** Autocorrelations calculated from the blue traces seen in Figure 9A. Note the pronounced troughs of the autocorrelations from the oscillating traces (blue). **B:** PSD plot of the irregular active AMC from Figure 9A (red trace). **Bii, Biii:** PSD plots calculated from the red and blue traces seen in Figure 9A. Power depicted in arbitrary units (AU). For comparison, the PSD of the irregular active cell (red) is shown in all three PSD plots. Irregular active cells have a lower PSD peak power. Adapted from Tsitoura *et al.*, 2020.

resulted in linearly decreasing correlation coefficients. This led to a pyramidal shape (Figure 10Ai), which made it easy to distinguish these cells from the oscillating population.

Autocorrelation of oscillating AMCs typically showed a series of pronounced side-troughs and peaks next to the peak at zero lag (Figure 10Ai, Figure 10Aii). These repetitively occurring side peaks indicated a reoccurring signal overlap of the original data trace.

In addition, PSDs were clearly distinguishable between irregular and oscillating AMCs (Figure 10B, red and blue traces). The power of dominant frequency band(s) in irregularly active AMCs was dramatically lower than in oscillating AMCs. In fact, PSDs of irregular neurons appeared as a flat line when compared to those of rhythmic AMCs (Figure 10Bii, Figure 10Biii).

Based on these two measures, autocorrelation and PSD, distinguishing these physiologically different AMC populations was possible in line with existing literature (Gorin *et al.*, 2016).

3. Results

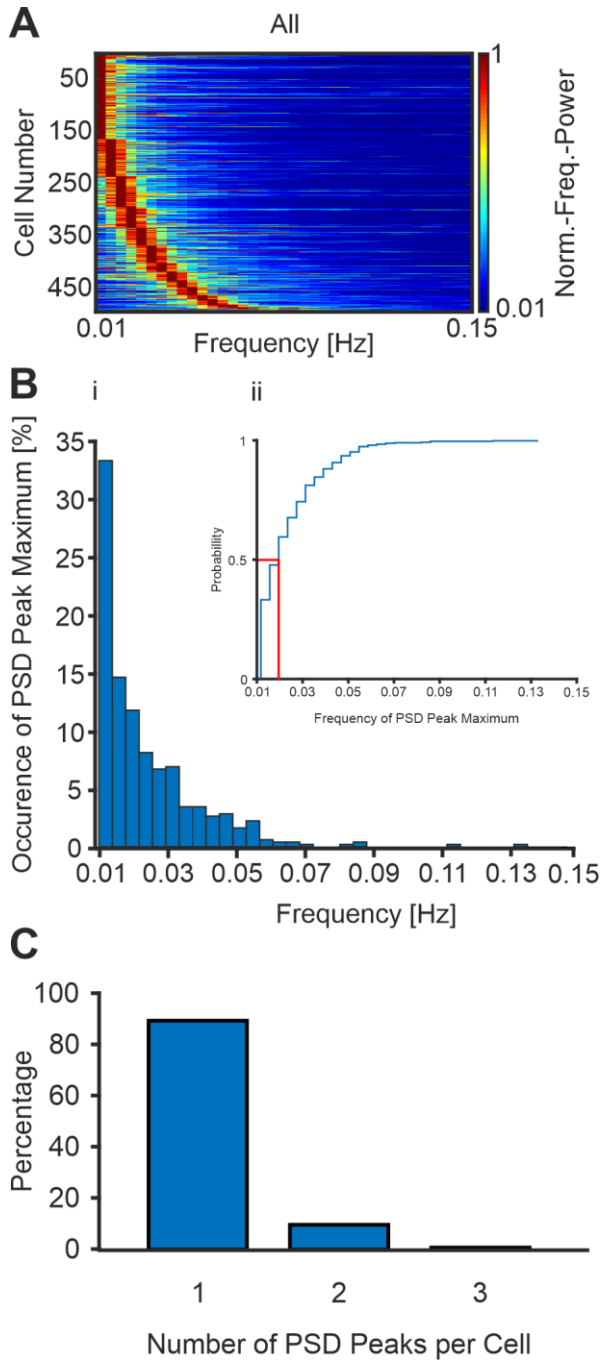


Figure 11: Frequency Spectra of All Oscillating AMCs In Vitro. **A:** Heat map represents normalized power spectra of 494 oscillating AMCs. Sorted after maximum peak frequency bin. Red color indicates high power, blue color indicates low power. **Bi:** The histogram represents the distribution of spectral power peaks from **A**. **Bii:** Cumulative probability of PSD peaks from **Bi**. Red line indicates $P_{0.5} = 0.016$ Hz. **C:** Percentage of AMCs from **A** that showed either 1, 2 or 3 peaks in their PSD spectrum (Threshold: Normalized frequency power ≥ 0.8). Adapted from Tsitoura *et al.*, 2020.

The power spectra of oscillating AMCs typically showed a single maximum peak in a frequency range between 0.01 and 0.15 Hz (Figure 11A, Figure 11C, $n = 494$, indicated by the dark red frequency bin).

Most oscillating AMCs showed a frequency peak below 0.05 Hz at resting conditions (Figure 11A, Figure 11B, 33-min recordings). 33% of all AMCs were in the lowest frequency bin between 0.01 and 0.016 Hz (Figure 11Bi). In line with this, the $P_{0.5}$ probability was 0.02 Hz (Figure 11Bii).

Furthermore, most AMCs showed only one prominent frequency peak with a power ≥ 0.8 (Figure 11C, 89.5 %). Only a minor portion displayed either two (9.7%) or three (0.8%) prominent frequencies.

Concluding, most AMCs showed a frequency peak in the lower frequency range. However, within this range the oscillating AMCs showed a heterogeneous frequency. Mostly, they only displayed one prominent frequency. However, a smaller population showed more than one frequency peak.

3. Results

Based on the topographic innervation of the AOB by VSNs, we checked for differences in the frequency domain of oscillating AMCs based on their location (Figure 12, Figure 13). We divided the AOB in three equally sized areas. The middle part was not analysed to avoid data ambiguity. The left and right parts of the AOB were then referred to as anterior or posterior parts.

In the anterior AOB, innervated mainly by V1R-positive VSNs, 32% of oscillating AMCs displayed their strongest frequency peak in the range between 0.01 and 0.16 Hz (Figure 12Bi). In addition, the $P_{0.5}$ probability was 0.016 Hz (Figure 12Bii). This is in line with the findings for all oscillating AMCs (Figure 11). The frequencies within the lower frequency spectra were again heterogeneous (Figure 12A, $n = 118$). Oscillating AMCs in the anterior AOB only showed up to two distinct frequency peaks with a power ≥ 0.8 (Figure 12C). Here, 92.5% displayed only one strong frequency peak. 7.5% showed a second prominent frequency.

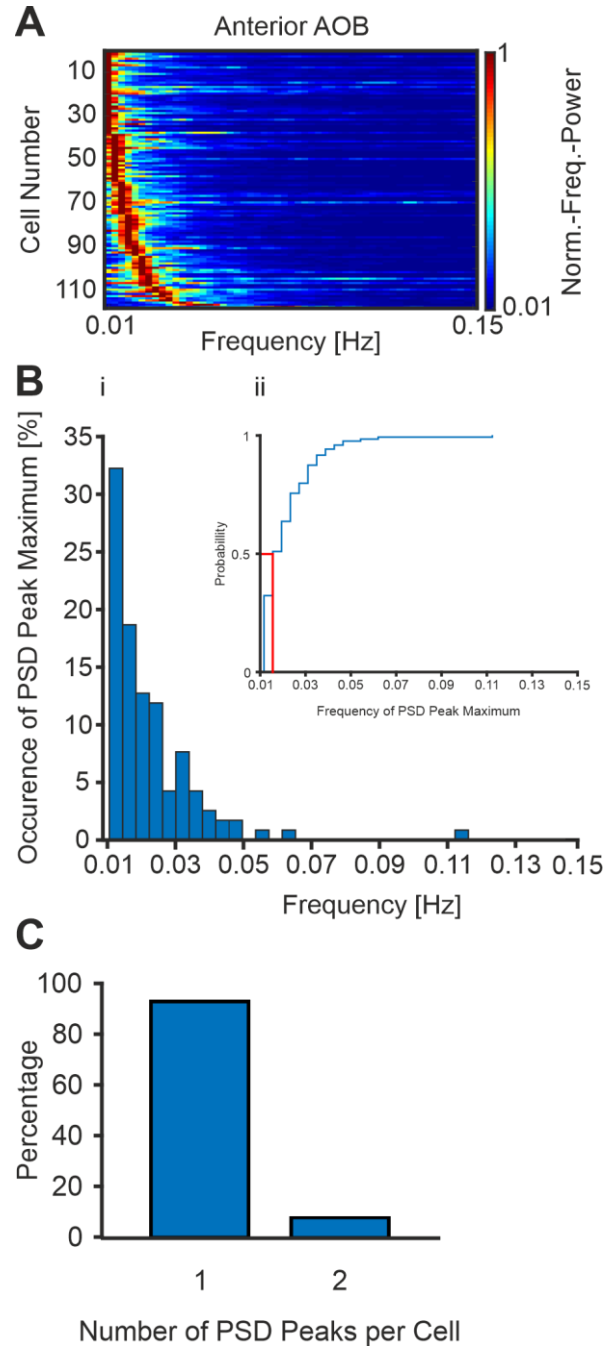


Figure 12: Frequency Spectra of All Oscillating AMCs in the Anterior AOB In Vitro. **A:** Heat map represents normalized power spectra of oscillating 118 AMCs in the anterior AOB. Red color indicates high power, blue color indicates low power. **Bi:** The histogram represents the distribution of spectral power peaks from **A**. **Bii:** Cumulative probability of PSD peaks from **Bi**. Red line indicates $P_{0.5} = 0.016$ Hz. **C:** Percentage of AMCs from **A** that showed either 1 or 2 peaks in their PSD spectrum (Threshold: Normalized frequency power ≥ 0.8).

3. Results

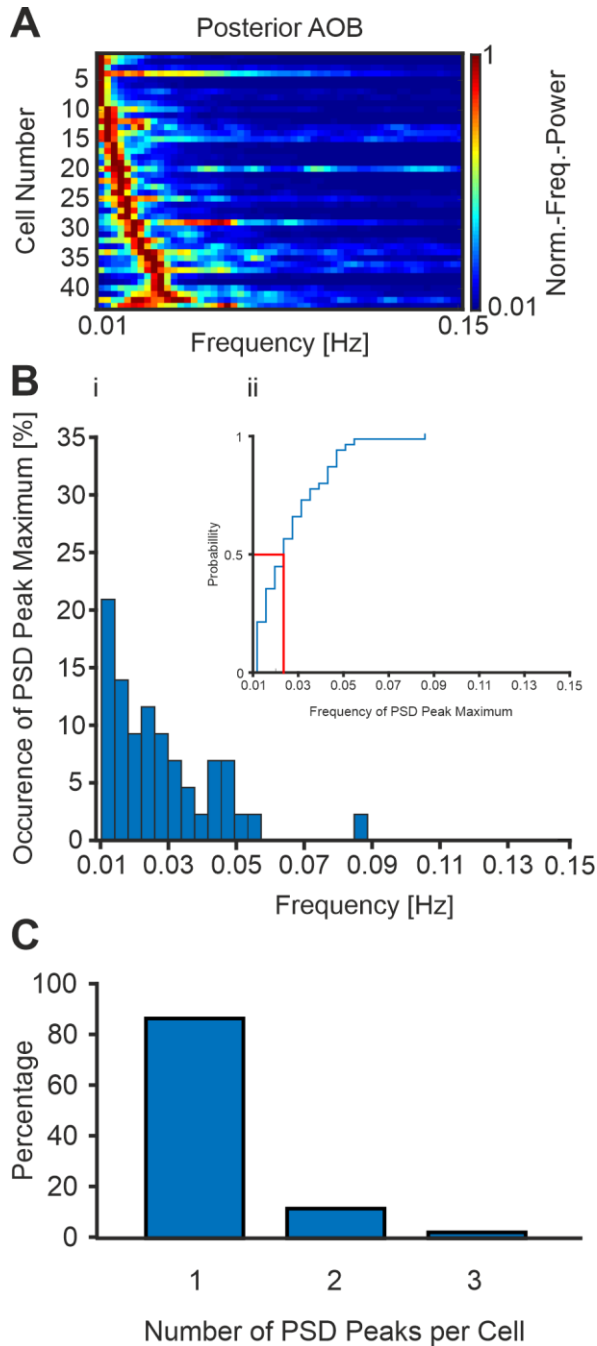


Figure 13: Frequency Spectra of All Oscillating AMCs in the Posterior AOB *In Vitro*. **A:** Heat map represents normalized power spectra of oscillating 43 AMCs in the anterior AOB. Red color indicates high power, blue color indicates low power. **Bi:** The histogram represents the distribution of spectral power peaks from **A**. **Bii:** Cumulative probability of PSD peaks from **Bi**. Red line indicates $P_{0.5} = 0.023$ Hz. **C:** Percentage of AMCs from **A** that showed either 1, 2 or 3 peaks in their PSD spectrum (Threshold: Normalized frequency power ≥ 0.8).

Together, oscillating AMC activity in the anterior AOB was in line with the findings of the whole AMC population, except only showing up to two prominent frequency peaks.

In the posterior AOB, mainly innervated by V2R-positive VSNs, frequency distribution was more heterogeneous compared to all oscillating AMCs or the ones located in the anterior AOB (Figure 13, Figure 11, Figure 12).

Although most oscillating AMCs in the posterior AOB were again located in the frequency domain ranging from 0.01 to 0.016 Hz (21%), the distribution was more heterogeneous (Figure 13Bi). In line with this, the $P_{0.5}$ probability was shifted to a higher frequency of 0.023 Hz (Figure 13Bii).

Comparable to the finding of the pooled oscillating AMC population, AMCs in the posterior AOB showed up to three distinct peaks in the PSD (Figure 13C). Here, most of them displayed a single peak (86.1%), some showed two prominent peaks (11.6%) and only a few three peaks (2.3%).

Summarizing these findings, the physiological properties of oscillating AMCs in either the anterior or posterior AOB did not differ dramatically from the phenotypes of the whole population.

3. Results

3.1.2 AOB Mitral Cells Organize into Distinct Microcircuits

The large number of oscillating AMCs found *in vitro* displaying strong temporal similarities gave rise to the question of neuronal interactions (Figure 11). Rhythmic AMC activity was shown to be either intrinsic or driven via synaptic input from the local neural network (Gorin *et al.*, 2016). Both mechanisms potentially enable entrainment of AMC ensembles into small neuronal subcircuits.

To gain information about cell connectivity we used the measured calcium fluctuations to calculate cross-correlations between AMCs. Allowing a time lag of ± 5 seconds, we examined the strength of correlation between signals from each oscillating AMC within individual brain slices. Since any two signals will display a certain degree of correlation, we focused on signals that are correlated above chance level. Therefore, we first plotted all correlation coefficients among the entire AMC population over all experiments during resting conditions in a 10-minute time window (Figure 14Ai).

Next, we fitted a gaussian function to the corresponding histograms left slope and peak. We used the 95% confidence interval of the gaussian fit as a measure of significance. Every cross-correlation coefficient greater than this value was referred to as significantly correlated neuronal activity. This classification built the basis for clustering AMCs into microcircuits (Figure 14B). All AMCs within a microcircuit were correlated with every other AMC within a circuit above this threshold. Based on this, we defined a microcircuit as the largest unique combination of AMCs found within one experiment that harbours at least three neurons. Notably, according to these criteria, one AMC could be part of multiple microcircuits (Figure 14B). Being part of more than one microcircuit implies that some cells display oscillations with more than one prominent frequency, which was in line with our findings (Figure 11).

3. Results

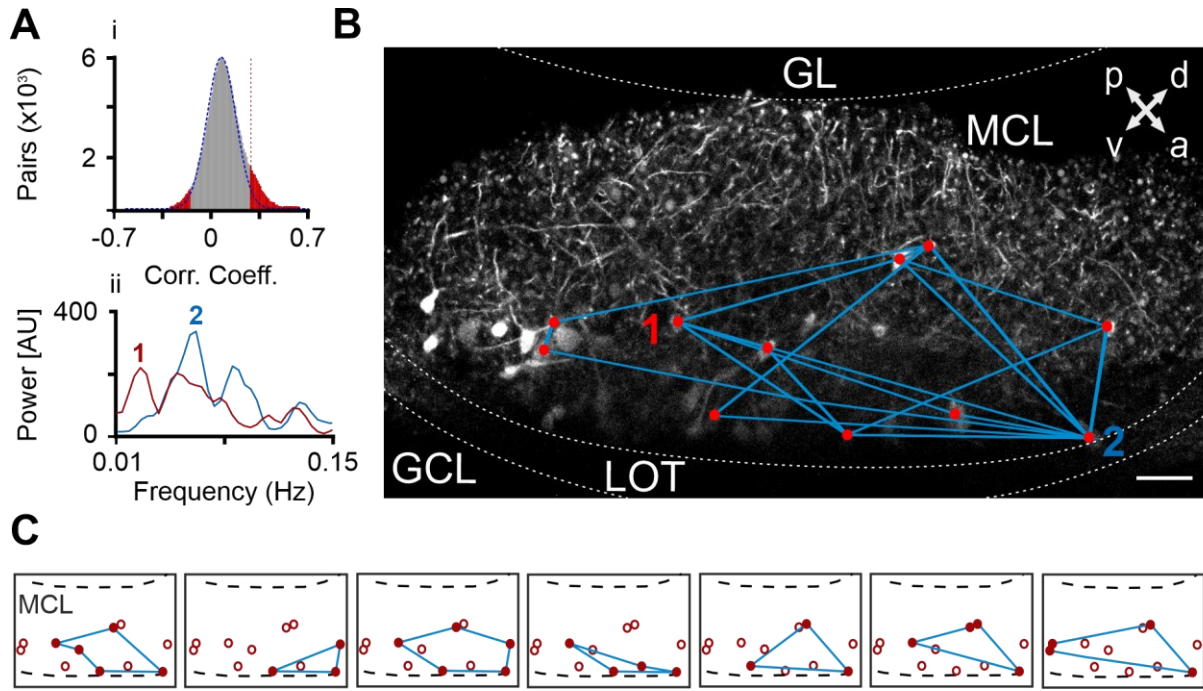


Figure 14: AMC Subsets form Synchronized Oscillatory Microcircuits *In Vitro*. **Ai:** Distribution of pairwise correlation coefficients calculated for all oscillating AMC pairs. Lag of ± 5 seconds was allowed. $n = 5763$. Each pair was analysed during 31 sliding windows with 5-minute duration. $n_{\text{total}}: 178,664$. The highest positive correlation coefficient was plotted. Fitting a Gaussian function, indicated by the blue dashed line, to the left slope and peak of the histogram reveals significantly correlated pairs of AMCs. The red dashed line indicates the 95% confidence interval of the Gaussian fit. **Aii:** PSDs of two distinct oscillating AMCs detected in more than one microcircuit displaying multiple frequency peaks. **B:** Maximum projection of 20 seconds after elevated potassium (S4) stimulation as grayscale image in an acute slice experiment. Red dots indicate AMCs detected as oscillating and significantly correlated with other AMCs. Blue lines indicate detected microcircuits. Tbet-Cre x GCaMP6f mouse. Scale bar 50 μm . GL: glomerular layer, MCL: mitral cell layer, LOT: lateral olfactory tract, GCL: granule cell layer. **C:** Detailed maps of detected oscillating and significantly correlated AMCs and microcircuits depicted in **B**. Adapted from Tsitoura *et al.*, 2020.

A high cross-correlation coefficient depends on strong similarities in the time domain. Some AMCs clearly showed more than one prominent peak in der power spectrum (Figure 14Aii). Accordingly, they were part of more than one microcircuit within the AOB (Figure 14B).

The microcircuits we found were distributed throughout the whole MCL (Figure 14C). Here, some circuits spanned nearly the entire MCL, others were only located within the anterior or posterior part.

3. Results

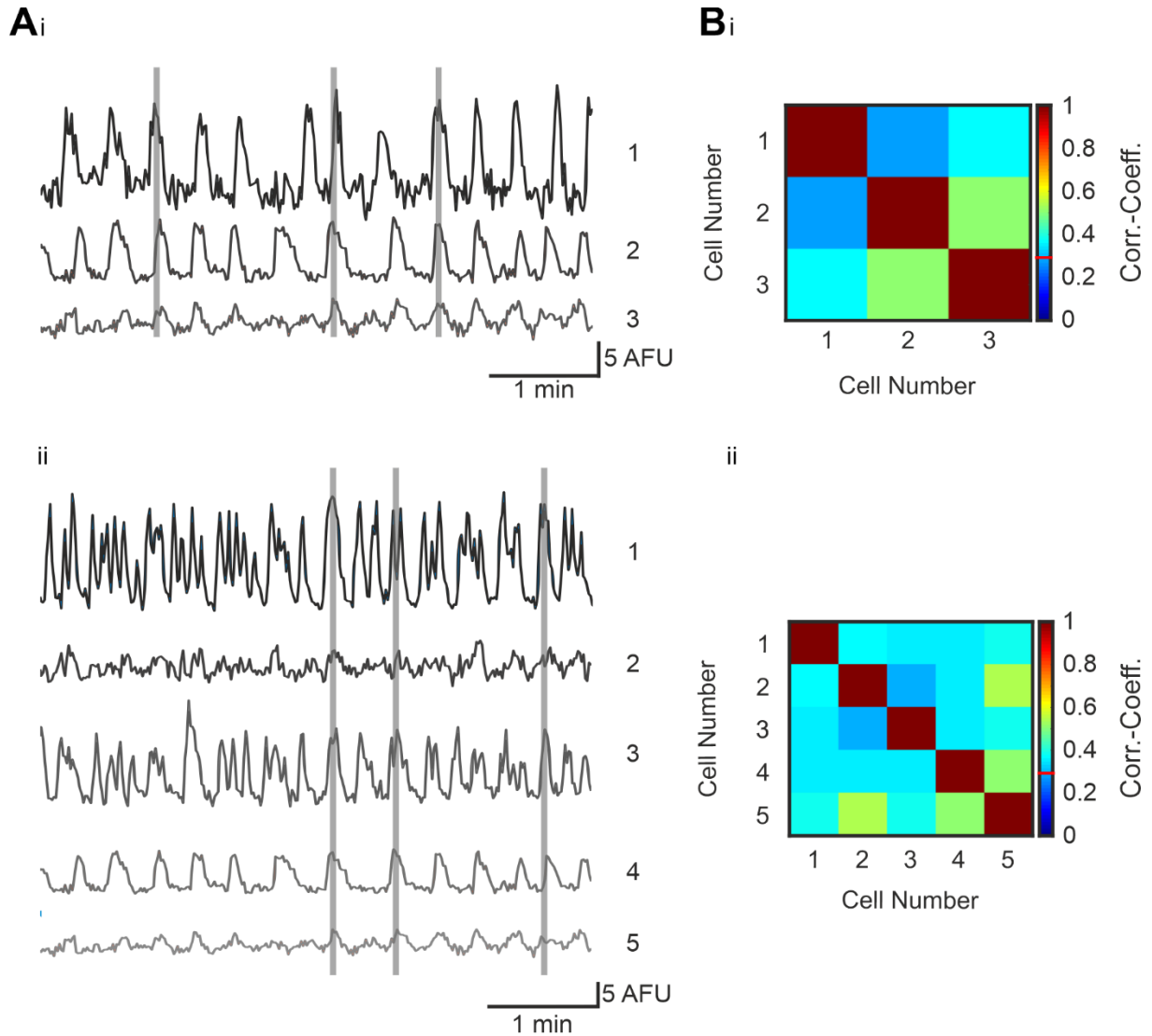


Figure 15: Representative Original Data Traces of Two Microcircuits *In Vitro*. **A:** Original data traces of two microcircuits with three (**A_i**) and five (**A_{ii}**) oscillating correlated AMCs from Figure 14B. The grey shaded areas highlight exemplary synchronized activity. **B_i**, **B_{ii}**: Cross-correlations of the original traces shown in **A**. Note the high degree of correlation among the clustered AMCs. The red bar in the color legend indicates the threshold for correlation significance. Adapted from Tsitoura *et al.*, 2020.

Looking at original data from two representative microcircuits, shown in Figure 14B and Figure 14C, the correlation of AMC calcium activity became obvious (Figure 15A). Over a period of 5 minutes, three respectively five AMCs showed largely correlated activity (Figure 15B). Furthermore, some AMCs showed activity peaks which are not in line with the overall microcircuit rhythm. Again, this was in line with previous spectral analysis identifying more than one prominent frequency. However, if AMCs were clustered within one microcircuit, they mostly communicated in temporal coupling with other circuit members.

3. Results

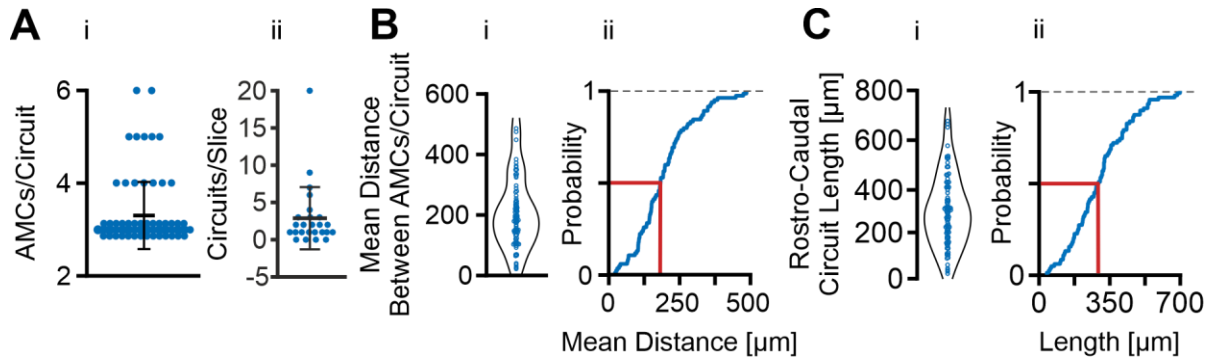


Figure 16: Quantification of AOB Microcircuits In Vitro. **A:** Number of AMCs per microcircuit and number of circuits per slice. Each blue dot indicates one experiment. We found up to six AMCs per microcircuit and up to 20 individual microcircuits per slice. AMCs/Circuit: 3.3 ± 0.72 . Circuits/Slice: 2.92 ± 4.2 . Numbers are mean \pm standard deviation. **B:** Violin plot (**Bi**) and cumulative probability (**Bii**) of the mean distance between AMCs within a circuit. This measure quantifies the mean distance between AMCs within one microcircuit. **Bi:** Mean \pm standard deviation: $195.6 \pm 101.5 \mu\text{m}$. **Bii:** $P_{0.5}$: $182.5 \mu\text{m}$. **C:** Violin plot (**Ci**) and cumulative probability (**Cii**) of the rostro-caudal circuit length. This measure quantifies the distance spanned by one microcircuit within the AOB. **Ci:** Mean \pm standard deviation: $289 \pm 150.5 \mu\text{m}$. **Cii:** $P_{0.5}$: $278.8 \mu\text{m}$. Adapted from Tsitoura *et al.*, 2020.

Utilizing confocal microscopy, the optical z-section depth was restricted. Therefore, we could not observe the whole AMC population at a time. Nevertheless, we found that one microcircuit in a single optical AOB section harbours up to six oscillating AMCs (Figure 14C, Figure 16Ai). Furthermore, in nearly all cases we observed at least one correlated ensemble per slice (Figure 16Aii). Notably, we found ~ 3 microcircuits per slice on average, with a range of up to 20 ensembles per slice. Considering the three-dimensional structure of the AOB and the number of up to 7,000 AMCs per bulb (Mohrhardt *et al.*, 2018), the number of AMCs per circuit in the intact AOB will be considerably higher. Analysing both the mean distance between AMCs within a circuit and the rostro-caudal circuit dimension, microcircuits showed to be distributed across the AOB (Figure 16B, Figure 16C). Considering the $P_{0.5}$ probability of $182.5 \mu\text{m}$ of the mean distance between cells within a circuit and the $P_{0.5}$ probability of $278.8 \mu\text{m}$ for the longest rostro-caudal circuit length, however, microcircuits had the tendency to rather not span the whole AOB.

Together, the large number of AMCs displaying rhythmic calcium oscillations enabled the clustering of highly correlated AMCs into microcircuits. Such circuits thus appeared to represent a prominent phenomenon of ‘idle-state’ AOB computation. Notably, one AMC could be part of more than one microcircuit. Microcircuits could either span a small area, or the AOB’s whole MCL. They had the tendency, however, to cover only a small portion of the MCL. Finally, these circuits can be a powerful tool to contribute to AOS information coding.

3.1.3 Pharmacological Dissection of Spontaneous AOB Mitral Cell Network Activity

Analysing AMC calcium signals *in vitro* revealed a high degree of rhythmic, correlated activity. Previous electrophysiological experiments revealed AMC populations that show these oscillations either as an intrinsic feature or as a result of synaptic entrainment (Gorin *et al.*, 2016). Thereby, a microcircuit could be constructed via an intrinsically oscillating AMC, entraining one or more other AMCs. This would lead to a common rhythm. It is unknown, however, which neurotransmitters could possibly contribute to this entrainment.

In the following, we made use of a major advantage the *in vitro* acute slice preparation offers: we tested pharmacological agents and directly analysed the influence on population activity within the AOB slice. Doing so, we investigated the potential influence of common excitatory and inhibitory neurotransmitters on microcircuit formation.

3.1.3.1 The Influence of Inhibitory Input on AOB Mitral Cells

A major source of inhibition in the AOB is mediated by dendrodendritic synapses between AMCs and GCs (Didier *et al.*, 2001). GCs hereby inhibit AMCs. This inhibition was shown to be largely dependent on activation of GABA_A-receptors (Schoppa *et al.*, 1998). To investigate the role of GABA_A-driven inhibition on AMC calcium oscillation and microcircuit formation we used the GABA_A antagonist gabazine. This inhibitory substance was applied to the network via the perfusion pencil (Figure 8A). The application of gabazine (S7) influenced AMC oscillation in different ways (Figure 17). Some AMCs started to show activity after blocking inhibition mediated by GABA_A receptors (Figure 17Ai). These AMCs not only started to be active: they started to oscillate. After gabazine application they started to show a distinct peak in the infraslow range in the temporal domain (Figure 17Bi).

Another population of AMCs that previously displayed calcium oscillations changed their oscillation pattern during the gabazine application (Figure 17Aii). Here, disinhibition of AMCs led to a shift in their temporal domain (Figure 17Bii). Furthermore, they not only changed their prominent frequency, but sometimes even displayed a second prominent frequency.

3. Results

On the other hand, some AMCs that oscillated before the application of gabazine were not influenced at all (Figure 17Aiii). Their oscillation pattern didn't change, which was also apparent in the PSD (Figure 17Biii).

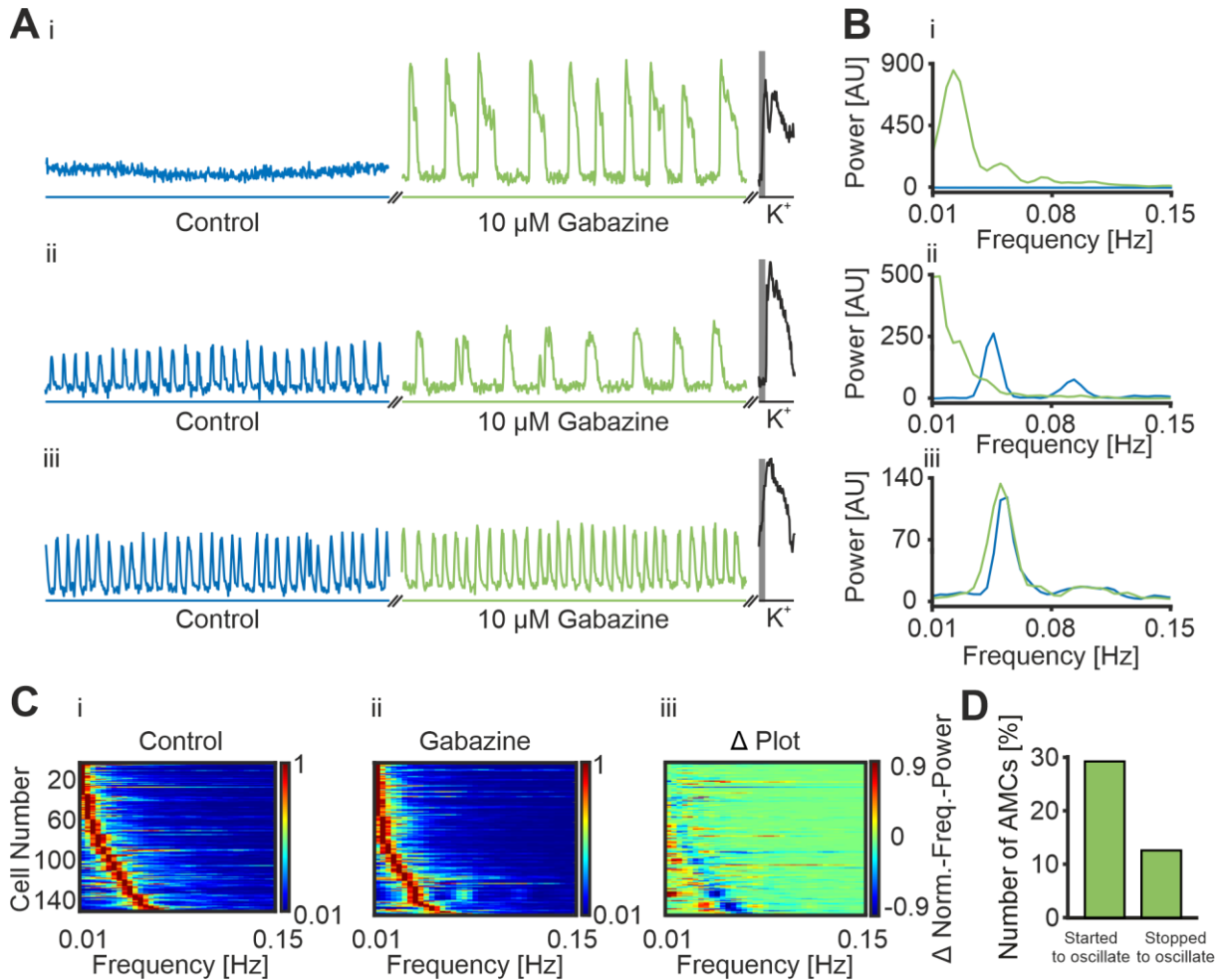


Figure 17: Effects of Gabazine Treatment on AMC Activity *In Vitro*. **A:** Representative recordings of AMC activity. Control (blue trace): 10-minute recording. Inhibitor (green trace): 10-minute recording. Grey shaded area: 10 seconds elevated potassium application (S4). **Ai:** AMC started to oscillate during gabazine treatment. **Aii:** AMC changed its oscillatory activity pattern during treatment. **Aiii:** AMC activity was not influenced by gabazine treatment. **B:** Power spectral density from the original recordings in **A**. Control: blue trace. Inhibitor: green trace. **Bi:** Frequency peak after gabazine treatment (green trace) compared to no strong frequency peak in the infraslow range during control conditions. **Bii:** Shift to one prominent peak in slower frequency ranges during gabazine application (green trace) compared to two prominent, faster frequency peaks during control conditions (blue trace). **Biii:** No difference in the temporal domain between control (blue trace) and gabazine treatment (green trace). **C:** Heatmaps show normalized power spectra for 153 oscillating AMCs during control and gabazine treatment. Sorted from slow to fast frequency peaks. **Ci:** Normalized frequencies of 153 AMCs during 10-minute control recording. **Cii:** Normalized frequencies of 153 AMCs during 10-minute gabazine treatment. Cell identity is the same as in **Ci**. **Ciii:** Heatmap showing the change in frequencies as difference plot from **Ci** and **Cii**. **D:** Percentage of AMCs that either started or stopped to oscillate after being treated with gabazine. Started to oscillate: 29.2%. Stopped to oscillate: 12.6%. Adapted from Tsitoura *et al.*, 2020.

3. Results

AMCs that continued oscillation during gabazine treatment prominently stayed active within the infraslow range, even if these cells shifted their main frequency peak (Figure 17C). However, if AMCs changed their frequency, they were most likely to shift to a slower oscillation frequency (Figure 17Ciii). Note that this was not the only effect on oscillation frequency: Some AMCs also changed their oscillation to faster frequencies.

Quantifying the effect of gabazine on AMC oscillation, we found that 29.2% of all AMCs that did not oscillate under control conditions started to oscillate after gabazine treatment (Figure 17D). On the other hand, we observed that 12.6% of AMCs that did show calcium oscillations under control conditions stopped to display such pattern during disinhibition. Together, these findings suggest that GABA_A receptor activity somehow masks AMC oscillations.

3.1.3.2 The Influence of Excitatory Input on AOB Mitral Cells

The dendrodendritic synapse is both excitatory (AMC-to-GC) and inhibitory (GC-to-AMC) (Didier *et al.*, 2001). Therefore, we blocked N-methyl-D-aspartate (NMDA) receptors using amino-5-phosphonopentanoate (AP5). In addition, we blocked two other common sources of excitation: α -amino-3-hydroxy-5-methyl-4-isoxazolepropionic acid (AMPA) and kainate receptors. To achieve this effect, we used 2,3-dioxo-6-nitro-7-sulfamoyl-benzo[f]quinoxaline (NBQX). AP5 was used at 100 μ M concentration, NBQX at 10 μ M (S7).

In many cases, blocking glutamatergic excitation by using AP5 and NBQX led to a stopping of AMC calcium oscillations (Figure 18Ai). Many AMCs that showed pronounced rhythmic activity stopped to oscillate. This phenotype was furthermore proven by a clear difference in the PSD power between control and inhibitor condition (Figure 18Bi). Quantifying this effect, 18.8% of all initially oscillating AMCs stopped to oscillate during AP5 and NBQX treatment (Figure 18D). To rule out cell death as a reason for this observation we used S4 to show that AMCs are still physiologically functional (Figure 18Ai, grey shaded area).

In addition, many AMCs showed a change in activity patterns after blocking excitation (Figure 18Aii). The oscillation shown under control conditions remained during inhibitor application, but a change in their prominent frequency became visible (Figure 18Bii).

3. Results

In the frequency domain, we didn't observe a clear trend towards faster or slower frequencies (Figure 18Ciii). However, most oscillating AMCs still displayed a frequency below 0.1 Hz after pharmacological treatment (Figure 18Cii).

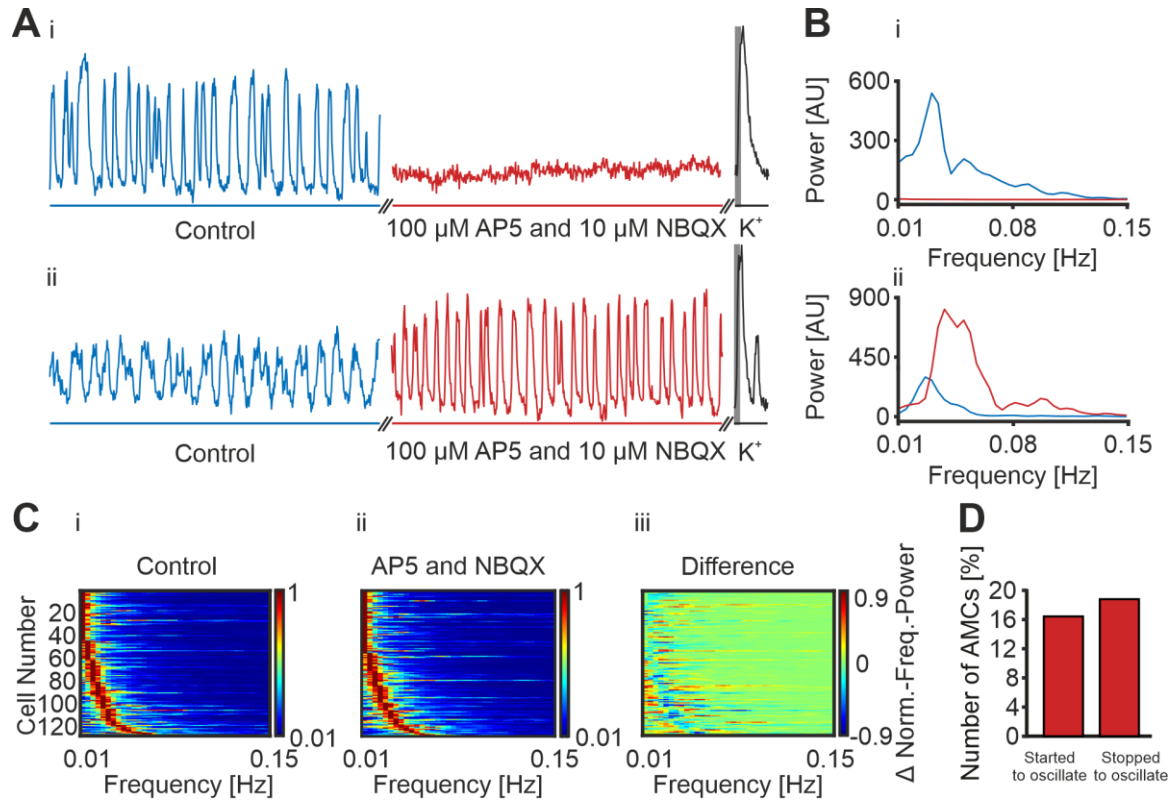


Figure 18: Effects of AP5 and NBQX Treatment on AMC Activity In Vitro. **A:** Representative recordings of AMC activity. Control (blue trace): 10-minute recording. Inhibitor (red trace): 10-minute recording. Grey shaded area: 10 seconds elevated potassium application (S4). **Ai:** AMC stopped to oscillate during AP5 and NBQX treatment. **Aii:** AMC changed its oscillatory activity pattern during treatment. **Bi:** Frequency peak during control conditions (blue trace) compared to no strong frequency peak in the infraslow range during AP5 and NBQX treatment (red trace). **Bii:** Shift in frequency after AP5 and NBQX treatment. Under control conditions (blue trace) the oscillation frequency is slower than under inhibitor conditions (red trace). **C:** Heatmaps show normalized power spectra for 134 oscillating AMCs during control conditions compared to AP5 and NBQX treatment. Sorted from slow to fast frequency peaks. **Ci:** Normalized frequencies of 134 AMCs during 10-minute control recording. **Cii:** Normalized frequencies of 134 AMCs during 10-minute AP5 and NBQX treatment. Cell identity is the same as in **Ci**. **Ciii:** Heatmap showing the change in frequencies as difference plot from **Ci** and **Cii**. **D:** Percentage of AMCs that either started or stopped to oscillate after being treated with AP5 and NBQX. Started to oscillate: 16.4%. Stopped to oscillate: 18.8%. Adapted from Tsitoura *et al.*, 2020.

Lastly, a fraction of AMCs that did not oscillate during control conditions started to oscillate after taking away excitation from the AOB network. This effect was observed for 16.4% of previously not oscillating AMCs (Figure 18D).

Concluding, blocking fast glutamatergic excitation within the AOB modulated AMC frequency in many cases. A clear trend towards a faster or slower frequency, however, was not observed.

3. Results

3.1.3.3 The Influence of Combined Excitatory and Inhibitory Input on AOB

Mitral Cells

Next, we asked what happened if we silence both fast glutamatergic and GABAergic synaptic transmission simultaneously. Using a combination of 100 μ M AP5, 10 μ M NBQX and 10 μ M gabazine (S7), we silenced all GABAergic and glutamatergic synapses in the AOB. Applying all three inhibitors lead to a combination of effects from isolated gabazine or AP5 and NBQX application (Figure 17, Figure 18, Figure 19).

A prominent population of AMCs started to show oscillations under the application of AP5, NBQX and gabazine (Figure 19Ai). This finding was further confirmed by the strong change in the PSDs (Figure 19Bi). We observed this effect in 19.2% of all analysed AMCs (Figure 19D).

Furthermore, taking away inhibition and excitation led to an abolishment of oscillatory activity in many AMCs (Figure 19Aii). Again, a strong change in the power of the PSD between control and inhibitor conditions was at hand (Figure 19Bii). We found that 23.3% of AMCs showed that phenotype after inhibitor treatment (Figure 19D). Interestingly, many AMCs did not alter their oscillatory activity at all (Figure 19Aiii). This can be explained by an absence of synaptic input to these AMCs.

The change in temporal domain overall showed a heterogeneous result under combined inhibitor conditions (Figure 19C). Some AMCs changed their frequency to lower values, but some displayed a strong increase in oscillation frequency (Figure 19Ciii).

3. Results

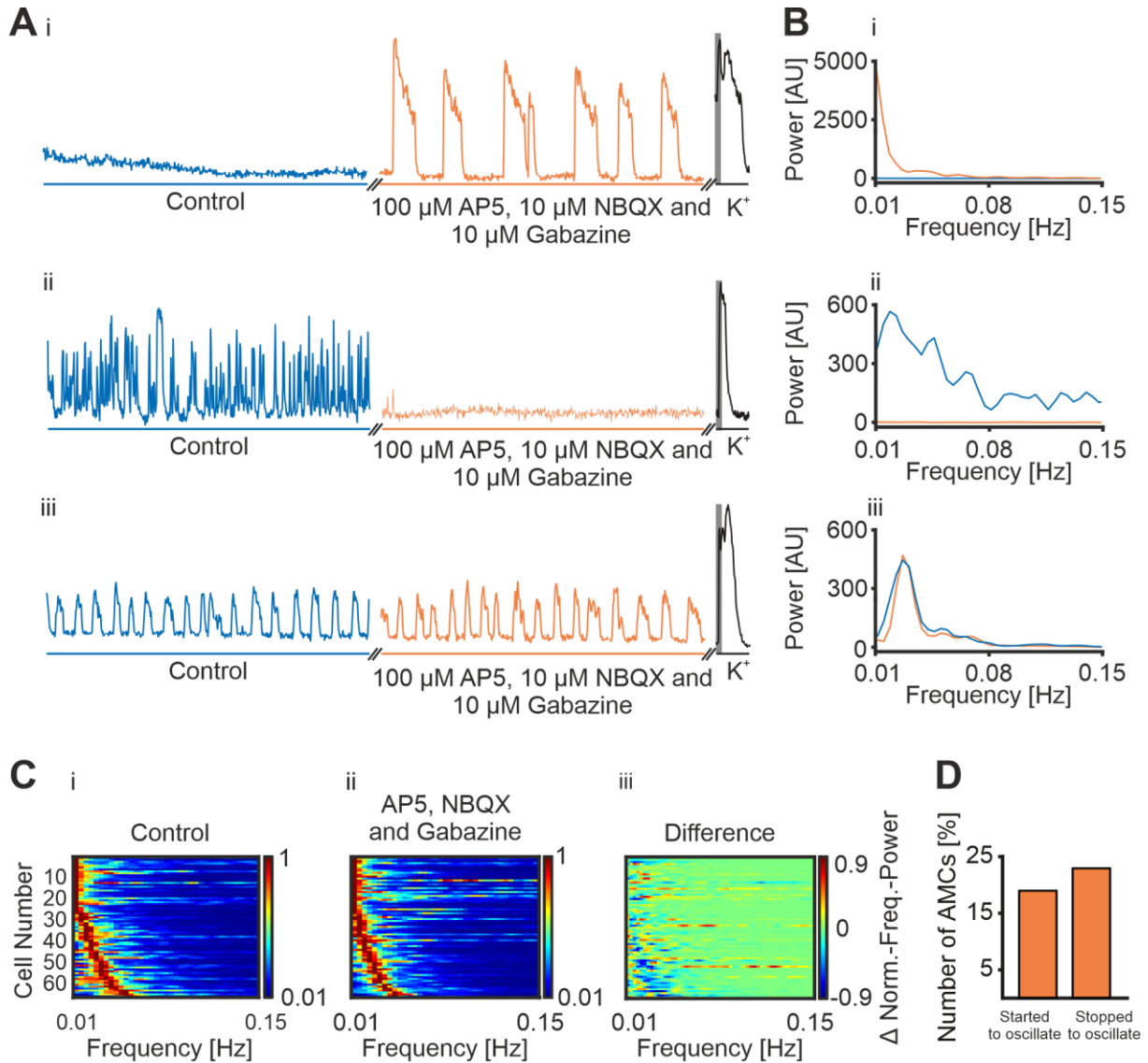


Figure 19: Effects of AP5, NBQX and Gabazine Treatment on AMC Activity In Vitro. **A:** Representative recordings of AMC activity. Control (blue trace): 10-minute recording. Inhibitor (orange trace): 10-minute recording. Grey shaded area: 10 seconds elevated potassium application (S4). **Ai:** AMC started to oscillate during AP5, NBQX and gabazine treatment. **Aii:** AMC stopped its oscillatory activity pattern during AP5, NBQX and gabazine treatment. **Aiii:** AMC activity was not influenced by AP5, NBQX and gabazine treatment. **B:** Power spectral density from the original recordings in **A**. Control: blue trace. Inhibitor: orange trace. **Bi:** Frequency peak after AP5, NBQX and gabazine treatment (orange trace) compared to no strong frequency peak in the infraslow range during control conditions. **Bii:** Frequency peak during control conditions (blue trace) compared to no strong frequency peak in the infraslow range during AP5, NBQX and gabazine treatment (orange trace). **Biii:** No difference in the temporal domain between control (blue trace) and AP5, NBQX and gabazine treatment (orange trace). **C:** Heatmaps show normalized power spectra for 153 oscillating AMCs during control and gabazine treatment. Sorted from slow to fast frequency peaks. **ci:** Normalized frequencies of 70 AMCs during 10-minute control recording. **cii:** Normalized frequencies of 70 AMCs during 10-minute AP5, NBQX and gabazine treatment. Cell identity is the same as in **ci**. **ciii:** Heatmap showing the change in frequencies as difference plot from **ci** and **cii**. **D:** Percentage of AMCs that either started or stopped to oscillate after being treated with gabazine. Started to oscillate: 19.2%. Stopped to oscillate: 23.2%.

3. Results

3.1.4 Pharmacological Dissection of AOB Microcircuit Formation

Pharmacological treatment had a strong effect on oscillatory behaviour of AMCs on single-cell level (Figure 17, Figure 18, Figure 19). Therefore, we next asked how inhibition of synaptic transmission affected microcircuit formation.

Blocking inhibition by applying 10 μM gabazine (S7) to the AOB network led to a significant increase in the number of oscillating AMCs per microcircuit (Figure 20Ai). The number of microcircuits per slice under these conditions, however, remained unchanged (Figure 20Bi). This indicated that AMCs that started to oscillate after disinhibition (Figure 17Ai, Figure 17D) joined already existing microcircuits. Therefore, blocking inhibition did not lead to an unmasking of inactive microcircuits.

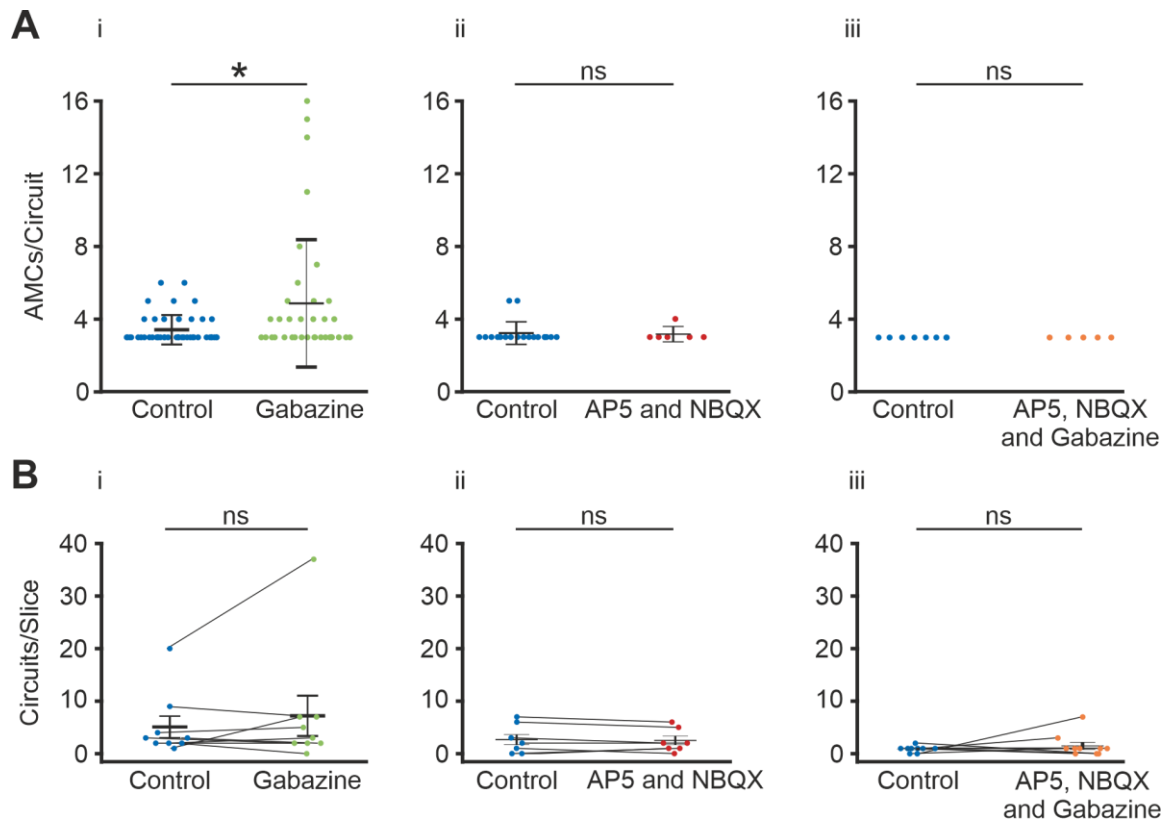


Figure 20: Influence of Blocking Inhibition, Excitation or Both on Microcircuit Formation *In Vitro*. **A:** Number of AMCs per microcircuit. Each dot indicates one experiment. Each brain slice is analysed during control and inhibitor condition. Black bars indicate mean \pm sd. **Ai:** Control: 3.89 ± 1.2 , gabazine (10 μM): 5.07 ± 3.18 . Significant difference, $p < 0.0471$, Wilcoxon rank-sum test. **Aii:** Control: 3.43 ± 0.84 , AP5 (100 μM) and NBQX (10 μM): 3.33 ± 0.84 . No significant difference, Wilcoxon rank-sum test. **Aiii:** Control: 3.22 ± 0.32 , gabazine (10 μM), AP5 (100 μM) and NBQX (10 μM): 3.30 ± 0.48 . No significant difference, Wilcoxon rank-sum test. **B:** Number of microcircuits per analysed brain slice. Each dot indicates one experiment. Each brain slice is analysed during control and inhibitor condition. Black bars indicate mean \pm sd. **Bi:** Control: 5.11 ± 2.02 , gabazine (10 μM): 7.22 ± 3.81 . No significant difference, Wilcoxon rank-sum test. **Bii:** Control: 2.71 ± 1.06 , AP5 (100 μM) and NBQX (10 μM): 2.43 ± 0.84 . No significant difference, Wilcoxon rank-sum test. **Biii:** Control: 0.89 ± 0.2 , gabazine (10 μM), AP5 (100 μM) and NBQX (10 μM): 1.5 ± 0.67 . No significant difference, Wilcoxon rank-sum test. Adapted from Tsitoura *et al.*, 2020.

3. Results

Treating the AOB network with AP5 and NBQX (S7) did not lead to a change in either the number of AMCs per microcircuit (Figure 20Aii) or the number of microcircuits per slice (Figure 20Bii). Therefore, AMPA, NMDA and kainate driven excitation was not an essential component for microcircuit formation. AMCs that stopped their oscillatory activity during treatment (Figure 18Ai, Figure 18D) were not part of active microcircuits.

Combining both paradigms, blocking inhibition and excitation (S7) at once did not lead to a change in either the number of AMCs per circuit (Figure 20Aiii) or the number of microcircuits per slice (Figure 20Biii).

3.2 AOB Mitral Cell Calcium Activity *In Vivo*

The *in vitro* approach, using large-scale calcium imaging in acute brain slices, is well suited to analyse single-cell and network activity, allowing also to dissect network activity pharmacologically. This advantage, however, comes at two major costs: First, the AOB network is perturbed by cutting the brain into 250 μm thin slices. Second, the AOB network is not connected to any other brain region anymore. This means we can neither investigate the influence of peripheral sensory input to the system, nor the influence of top-down modulation. This can only be done in the intact brain in a living animal.

A surgical procedure to observe AMCs at single-cell resolution performing two-photon calcium imaging didn't exist so far. Therefore, for the first time, we established an approach to make the AOB network experimentally accessible using *in vivo* two-photon imaging. This enabled us to gain insight into AMC network activity at large scales with single-cell resolution.

3.2.1 AOB Mitral Cell Imaging Using Glass Microprisms

In many brain areas, gaining optical access *in vivo* is a profound challenge. The main reason is light scattering of brain tissue. Using advanced two-photon microscopy techniques, like underfilling the objectives backside combined with high wavelength laser excitation, a penetration depth of 1,200 μm in brain tissue can be achieved (Kondo *et al.*, 2017). Sometimes, however, other obstacles occur. In this thesis, we had to deal with a large blood vessel that lies in the linear light path from the brain's surface to the MCL (Figure 21Ci). Given the broad spectral absorption range of

3. Results

haemoglobin, two-photon imaging through such a large blood vessel is technically not possible.

Several approaches like thinning the skull, precise tissue removal, or use of optical aids have been developed to extend 2-photon imaging to more hidden brain areas. One of these approaches utilizes glass microprisms (Andermann *et al.*, 2013). The hypotenuse of these microprisms is coated with aluminium to create a reflective surface (Figure 21Ai). This coating helps to create a rectangular light path.

After drilling an opening in the skull above the OB and frontal cortex we obtained access to the brain surface. Doing so, we removed one big blood vessel that lies within the skull above the gap between OB and cortex (Figure 21Ci). This enabled us to remove the dura mater, gently remove some cortical tissue by applying negative pressure to a blunt needle, and finally placing the 1.5 x 1.5 x 1.5 mm sized glass microprism between OB and cortex (Figure 21Aii, Figure 21Cii).

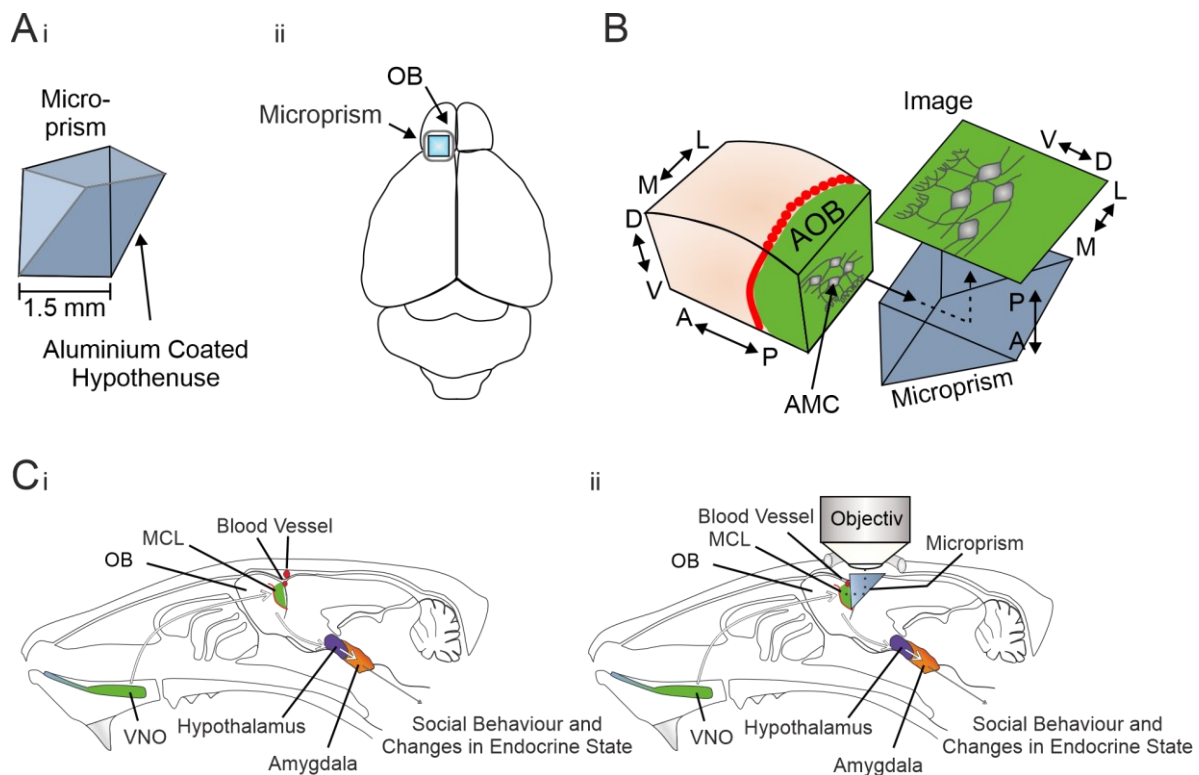


Figure 21: Experimental Procedure of AOB Calcium Imaging *In Vivo*. **A:** Glass microprism and schematic posing for AOB imaging. **Ai:** Glass microprism with aluminium coated hypotenuse. 1.5 x 1.5 x 1.5 mm size. **Aii:** Microprism positioning between the left olfactory bulb (OB) and cortex. **B:** Schematic depiction of a 1.5x1.5x1.5 mm field of view of the MCL enabled by the microprism. Rectangular light path indicated by the black dashed arrow. A: anterior, P: posterior, D: dorsal, V: ventral, L: lateral, M: medial, AMC: accessory olfactory bulb (AOB) mitral cell. **Ci:** Schematic head of a Tbet-Cre x GCaMP6f mouse. Fluorescent AMCs indicated in green. Note the two large blood vessels. One is located within the skull, the other one in the dura mater between AOB and cortex. VNO: Vomeronasal organ, OB: Olfactory bulb, MCL: Mitral cell layer. **Cii:** Same schematic mouse head as in **Ci**, but this time with implanted glass microprism. The rectangular light path is indicated by the black dashed line. Note that the blood vessel between AOB and cortex is still intact. VNO: Vomeronasal organ, OB: Olfactory bulb, MCL: Mitral cell layer.

3. Results

After fixating the microprism in the right position we obtained optical access to the MCL. Therefore, performing calcium imaging of AMCs at cellular resolution became possible (Figure 21B). Making use of the rectangular light path (Figure 21Cii, dashed black line) we achieved a large scanning area with stable optical access to the tissue.

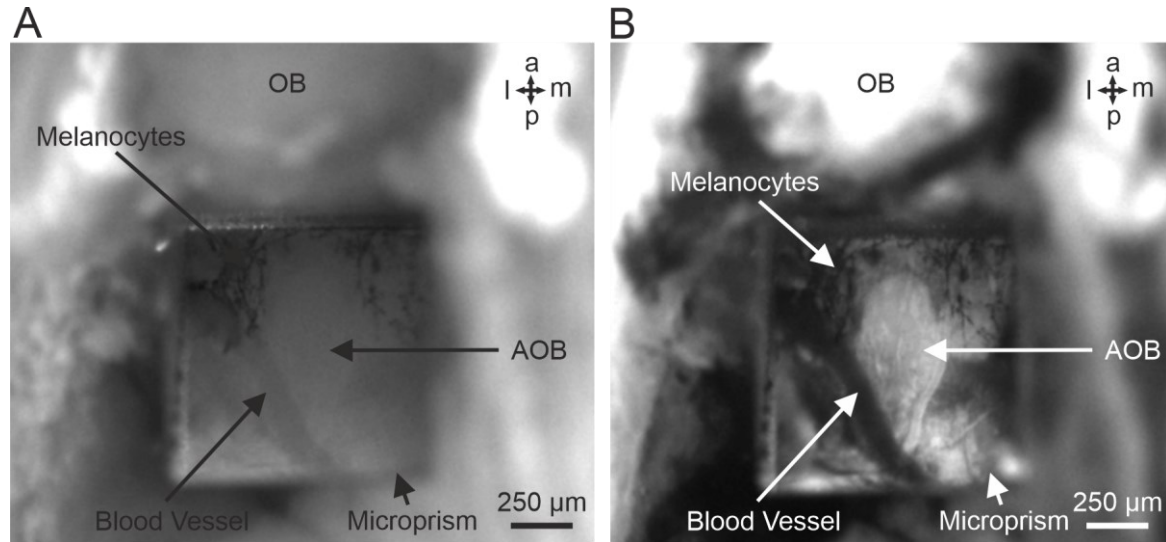


Figure 22: Verification of Microprism Positioning in Differential Interference Contrast and Epifluorescence Microscopy *In Vivo*. **A:** Differential interference contrast image of the microprism positioning. This microscopy technique is used to verify an unhindered field of view. Note that the microprism is inserted without harming the olfactory bulb (OB) after removing cortex tissue. **B:** Epifluorescence microscopy is used to verify the location of the accessory olfactory bulb (AOB) in the microprism. Note that with this technique we cannot distinguish the MCL from the GL. Tbet-Cre x GCaMP6f mouse.

This optical access was verified by differential interference contrast (DIC) microscopy (Figure 22A) and epifluorescence imaging (Figure 22B). Here, we could show that the dura mater is still intact, as indicated by melanocytes (Gudjohnsen *et al.*, 2015). Furthermore, the large blood vessel between AOB and cortex is still intact, indicating continuous tissue oxygenation. Using epifluorescence microscopy, we could then localize the AOB at the bulb's posterio-dorsal end.

The newly established approach shown here had many advantages: First, we obtained single-cell resolution for imaging AMCs. Second, all-important olfactory brain areas were intact after surgery. Neither the OB, nor other important parts of the olfactory pathway like for example the accessory olfactory nucleus (AON) were harmed (Figure 21Cii). Third, we retained a fully intact connection between VNO and AOB (Figure 21Cii), maintaining information flow from peripheral detection of environmental sensory stimuli to the brain's first central processing stage along the accessory

3. Results

olfactory pathway. Furthermore, the AOB still had intact projections to higher brain areas like amygdala and hypothalamus (Figure 21C).

In summary, we established an experimental tool to investigate the cellular activity of the AOBs main projection neurons for the first time.

3.2.2 Spontaneous AOB Mitral Cell Activity

Utilizing this newly established approach we performed *in vivo* live-cell calcium imaging in the AOB of Tbet-Cre x GCaMP6f mice (Figure 23A). Like previously found *in vitro*, we observed pronounced calcium fluctuations in AMCs at rest (Figure 23B). These fluctuations appeared to be highly heterogeneous and displayed either a slow (Figure 23B-1) or fast (burst-like) activity (Figure 23B-4). Furthermore, some AMCs changed activity patterns (Figure 23B-2) during the recording period. Sometimes we observed that AMC activity stopped. Lastly, some neurons showed apparently random activity (Figure 23B-3).

In addition, our recordings monitored AMC calcium fluctuations at detailed spatial resolution. This means, we could not only observe calcium changes in AMC somata, but also in putative dendrites (Figure 23A). Furthermore, our signal-to-noise ratio was sufficiently high to enable analysis of somata that did not lie exactly in the optical z-plane of our two-photon recordings (Figure 23Ai, Figure 23B-4). This increased the yield of cells that could be analysed.

Concluding, the approach developed in this thesis enabled detailed analysis of AMC single-cell activity *in vivo* via large-scale live-cell calcium imaging. This laid a solid basis to gain deeper understanding of AOB physiology.

3. Results

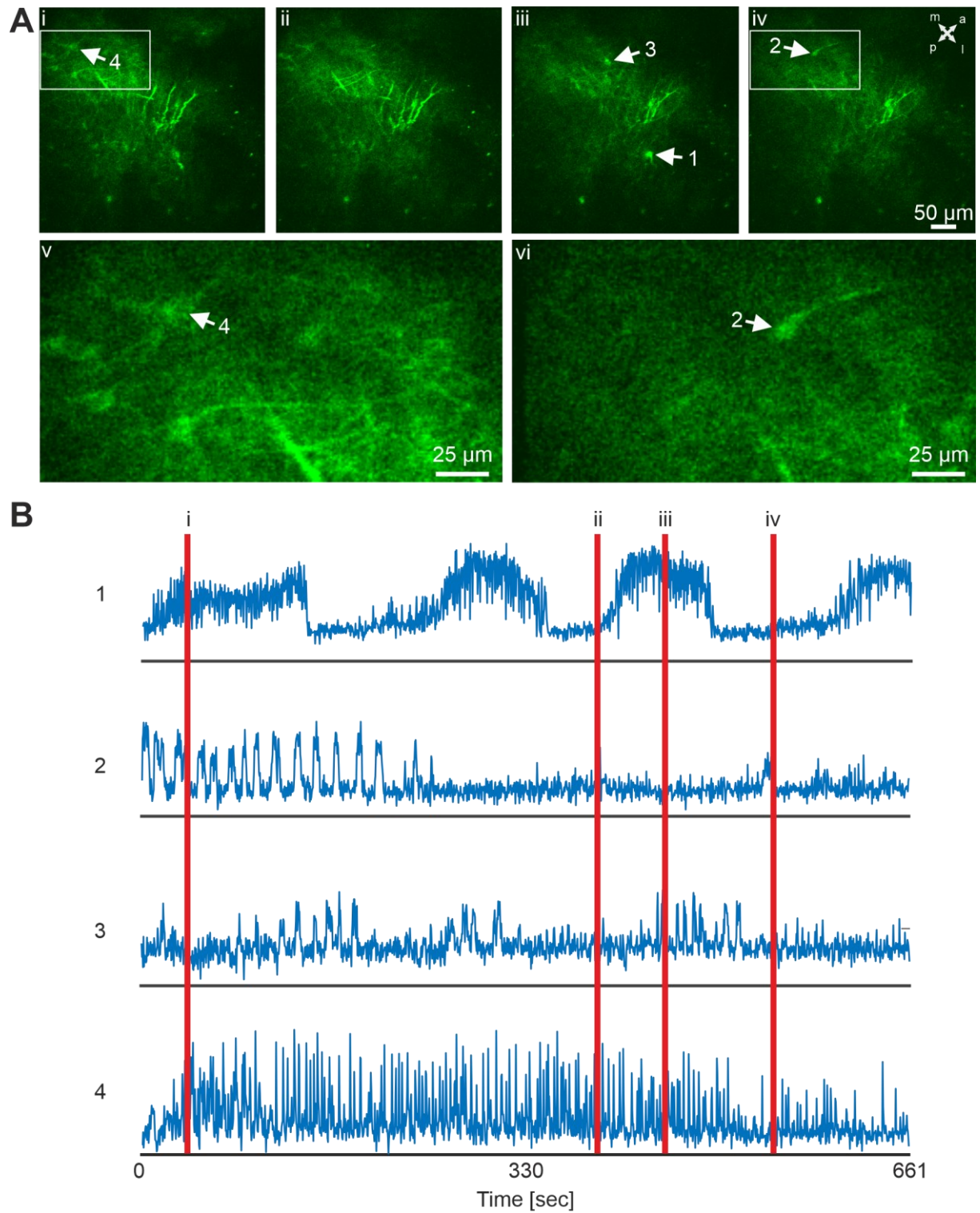


Figure 23: Spontaneous Calcium Activity of AMCs *In Vivo*. **Ai-iv:** Representative pictures of an *in vivo* two-photon microscopy measurement of the MCL using implanted microprisms in an anaesthetised Tbet-Cre x GCaMP6f mouse. Note the oscillatory activity of fluctuating calcium transients over time indicated by the white arrows. Each picture is a maximum projection of 5 frames. A: anterior, p: posterior, m: medial l: lateral. **Av, Aiv:** Zoom in from the area in the white boxes in **Ai** and **Aiv** **B:** Original data traces of the AMCs (1-4) shown in **A** over a time course of 11 minutes. Redlines (i – iv) indicate the time points the images of **A** (i-iv) were taken.

3. Results

3.2.2.1 Single-cell Calcium Analysis

Having shown that the *in vivo* approach was suitable to detect single-cell calcium fluctuations, we now aimed to analyse the AMC activity at rest. Note that “at rest” in this *in vivo* paradigm always means that spontaneous contractions of the VNO, and therefore a stimulation via “volatile” cues, could not be excluded. All data, however, was acquired in absence of intentional stimulation.

We first divided AMCs into active and silent neurons (Figure 24). Here, active neurons showed pronounced activity throughout the recording (Figure 24A). Silent AMCs lacked such activity and were identified only by baseline fluorescence (Figure 24B). In contrast to *in vitro* recordings, however, we could not apply elevated potassium solution (S4) to AMCs as a positive control for AMC viability during *in vivo* experiments. Therefore, we most likely underestimated the number of silent AMCs, because of low baseline fluorescence of GCaMP6f. Comparing original traces of active and silent AMCs, however, allowed distinction between both states.

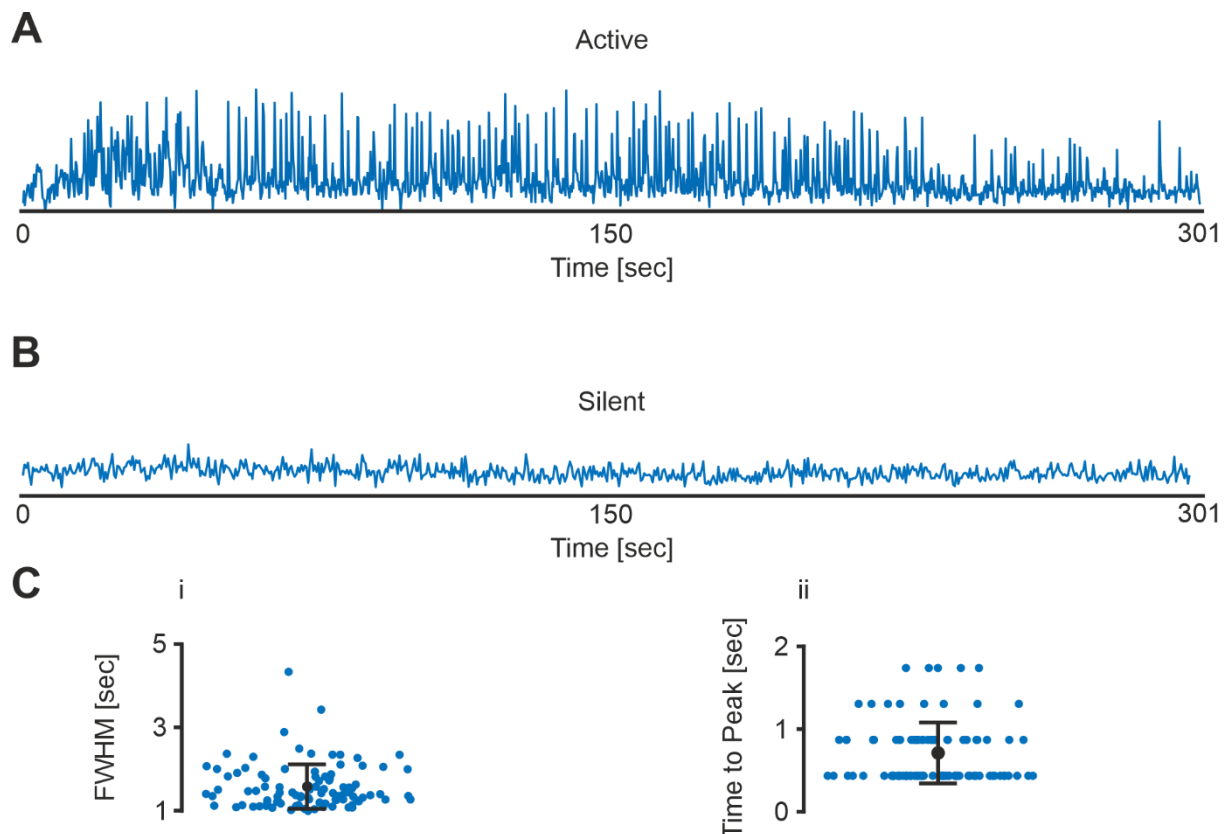


Figure 24: AMCs can be Subdivided into Active and Silent Phenotypes *In Vivo*. **A:** 5-minute recording of an active AMC *in vivo* at resting conditions. **B:** 5-minute recording of an AMC that is silent at resting conditions. **Ci:** Full width at half maximum (FWHM) in seconds for each activity up-state of the AMC shown in **A**. Each blue dot corresponds to one up-state. $n = 98$. Mean \pm SD: 1.58 ± 0.53 seconds. **Cii:** Time to peak in seconds for each activity up-state of the AMC shown in **A**. Each blue dot corresponds to one up-state. $n = 98$. Mean \pm SD: 0.71 ± 0.37 seconds.

3. Results

Next, we quantified signal kinetics in active AMCs (Figure 24C). As basic measures we determined the full width at half maximum (FWHM; Figure 24Ci) and the time to peak of each transient calcium elevation (Figure 24Cii). Here, FWHM serves as a measure for signal duration, whereas time to peak indicates how fast calcium signals rise. The AMC shown in Figure 24A had a mean FWHM of 1.58 ± 0.53 seconds. The time to peak was measured at 0.71 ± 0.37 seconds.

3.2.2.1.1 Oscillating AOB Mitral Cells

Next, we asked whether we could identify oscillating AMCs *in vivo*. So far, we had described this physiological phenotype only *in vitro*. Coarse observations from original traces suggested that many AMCs might display some rhythmicity (Figure 25A). Some AMCs showed such activity on faster (Figure 25Ai), others on slower time scales (Figure 25Aii). Both patterns, however, appeared relatively stable over 11-minute resting condition recordings.

To categorize this activity as rhythmic or not, we again used autocorrelations of the original calcium traces (Figure 25B). Indeed, we found clear evidence in the autocorrelation that AMCs, showing fast or slowly recurring calcium transients, are rhythmically active. Shifting the detected peaks yielded in strong pronounced side peaks (Figure 25Bi, Bii).

Another tool to measure rhythmicity is analysing inter-event times (IET). If calcium up-states occurs rhythmically, we expect IET histograms to show some degree of clustering. Of course, such analysis can only yield robust results if a sufficiently large number of events is recorded. Here, for the example AMC trace shown in Figure 25Ai, many IETs clustered in the time bin of 15 - 17.5 seconds (Figure 25Ci). Notably, all IETs clustered within a relatively small range between 12.5 and 32.5 seconds. We interpret this result as another indication for rhythmically occurring AMC calcium fluctuations *in vivo*.

3. Results

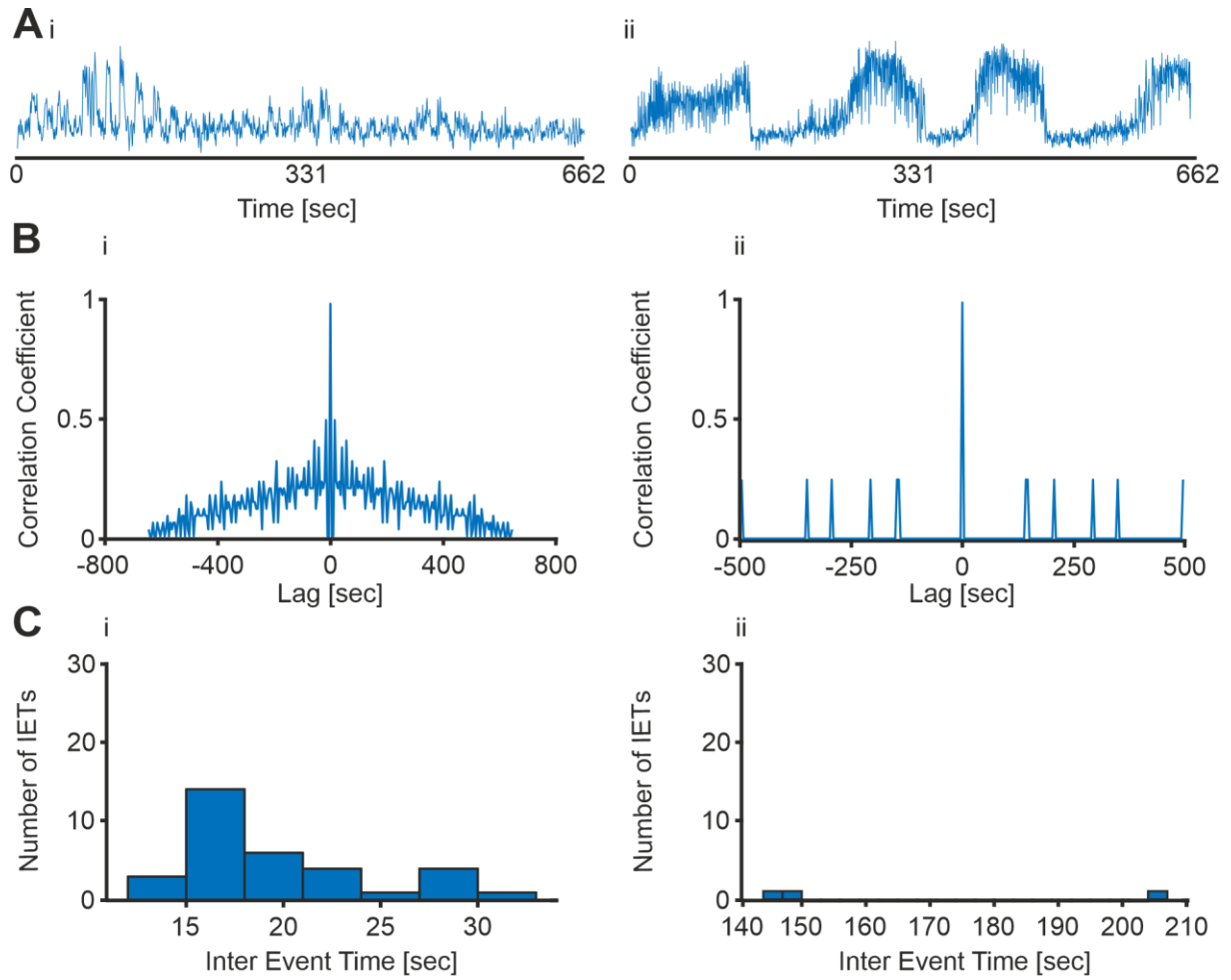


Figure 25: Classification of Oscillating AMCs In Vivo. **A:** Original traces of a fast-oscillating AMC (**Ai**) and a slow-oscillating AMC (**Aii**). Both traces were recorded over 6 minutes at resting conditions. **B:** Autocorrelation of the AMC in **Ai** (shown in **Bi**) and of the AMC in **Aii** (shown in **Bii**). **C:** Number of inter-event times (IET) between the activity up-states from the AMC in **Ai** (shown in **Ci**) and of the AMC shown in **Aii** (shown in **Cii**). **Ci, Cii:** Bin size: 3 seconds.

A somehow comparable, though obviously not robust result was observed for AMCs with slower activity (Figure 25Aii). Note, however, that the IET for such an AMC with ≤ 4 up-states in the analysed time window is by far no reliable measure.

As a last measure we analysed the coefficient of variation (COV) of the IET distribution. The COV is the ratio of the standard deviation to the mean and therefore measures the extend of variability in relation to the mean of the population. The higher the COV, the greater the data dispersion. For oscillating AMCs the COV of the IETs was always < 0.5 . For the two AMCs shown, the COV was 0.239 (Figure 25Ai) and 0.202 (Figure 25Aii), respectively. This finding was another indicator for non-random IETs and, therefore, rhythmicity.

3. Results

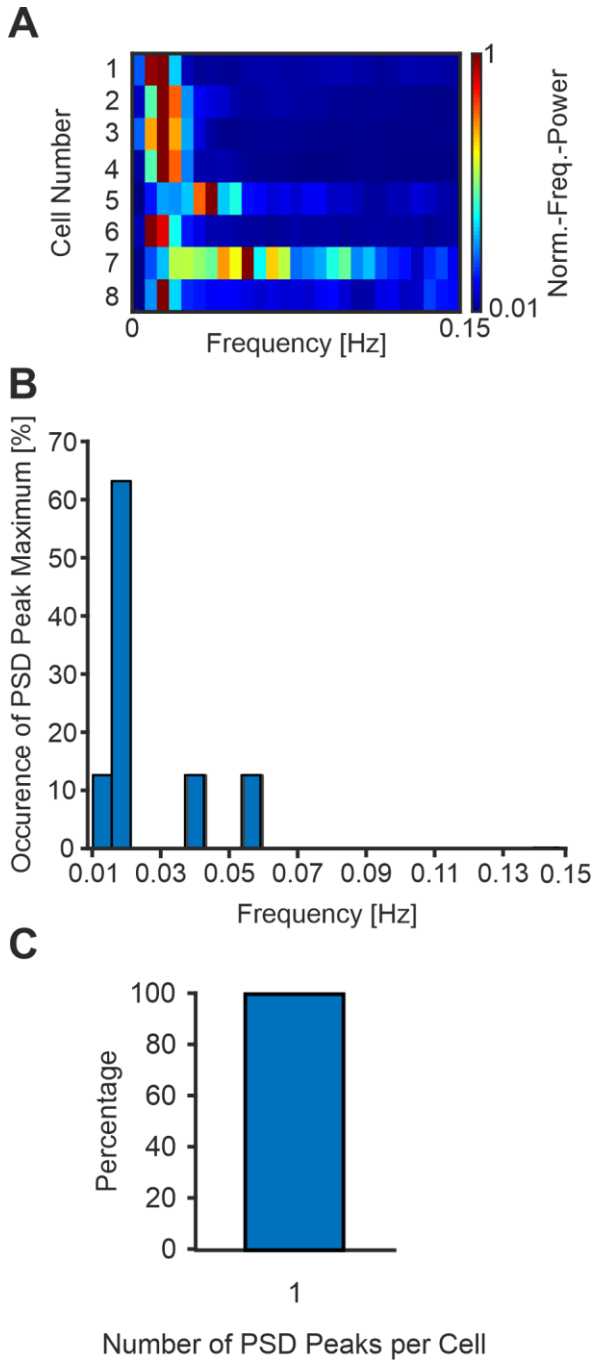


Figure 26: Temporal Domain Properties of Oscillating AMCs In Vivo. **A:** Power spectral density (PSD) of all oscillating AMCs ($n = 8$) in a frequency range from 0 to 0.15 Hz. The power was normalized to the maximal peak for each AMC. Frequency bin: 0.006 Hz. **B:** Occurrence of PSD peak maximum for every AMC from **A**. Bin size: 0.006 Hz. **C:** Percentage of the number of PSD peaks per AMC. A peak is defined as a normalized power in the PSD spectrum > 0.8 . $n = 8$.

In addition, oscillating AMCs *in vivo* were active in a frequency domain comparable to our *in vitro* findings (Figure 12, Figure 26A). The oscillation frequencies clearly clustered in the infraslow range close to 0.01 Hz. No oscillating AMCs recorded so far ($n = 8$) showed a frequency peak above 0.055 Hz (Figure 26B). 62.5% of neurons clustered around 0.012 Hz. Another prominent hallmark of this neuron population was that they only displayed one prominent peak in the PSD (Figure 26C, threshold power > 0.8). This means, these AMCs would likely be members of just one microcircuit that operates in the infraslow frequency range.

Taking together, the *in vivo* recordings of AMC calcium fluctuations showed a clearly oscillating phenotype. This confirmed *in vitro* results and underlined a likely physiological relevance of this activity pattern for AOB network computation.

3. Results

3.2.2.1.2 Irregular Bursting AOB Mitral Cells

Aside from oscillating AMC activity, the literature described another AMC phenotype identified by *in vitro* electrophysiology: irregular bursting AMCs (Gorin *et al.*, 2016). While displaying bursting activity, such bursts occur without any apparent rhythmic pattern.

In *in vivo* calcium imaging experiments, we indeed found AMCs showing this phenotype (Figure 27). This AMC population showed prolonged activity with burst-like periods over a 31-minute recording (Figure 27A). Analysing the original fluorescence traces calculating autocorrelations, however, didn't reveal rhythmic activity (Figure 27B). Both examples showed a steady, linear decay of the correlation coefficient over time, excluding general rhythmogenesis (Figure 27Bi, Figure 27Bii).

In contrast, the IET histograms clearly clustered around specific time bins (Figure 27C). The first example AMC (Figure 27Ai) clearly showed IET clustering between zero and twenty seconds (Figure 27Ci). This peak decreased exponentially. In addition, the second example AMC (Figure 27Aii) showed the same pattern with IET mostly between 10 and 30 seconds. The decay again appeared to be exponential. Since this AMC showed less peaks during the 31-minute recording (Figure 27Aii, Figure 27Cii) the finding of irregular bursting AMCs in *in vivo* calcium imaging experiments was true for neurons that are active at fast and slow timescales.

3. Results

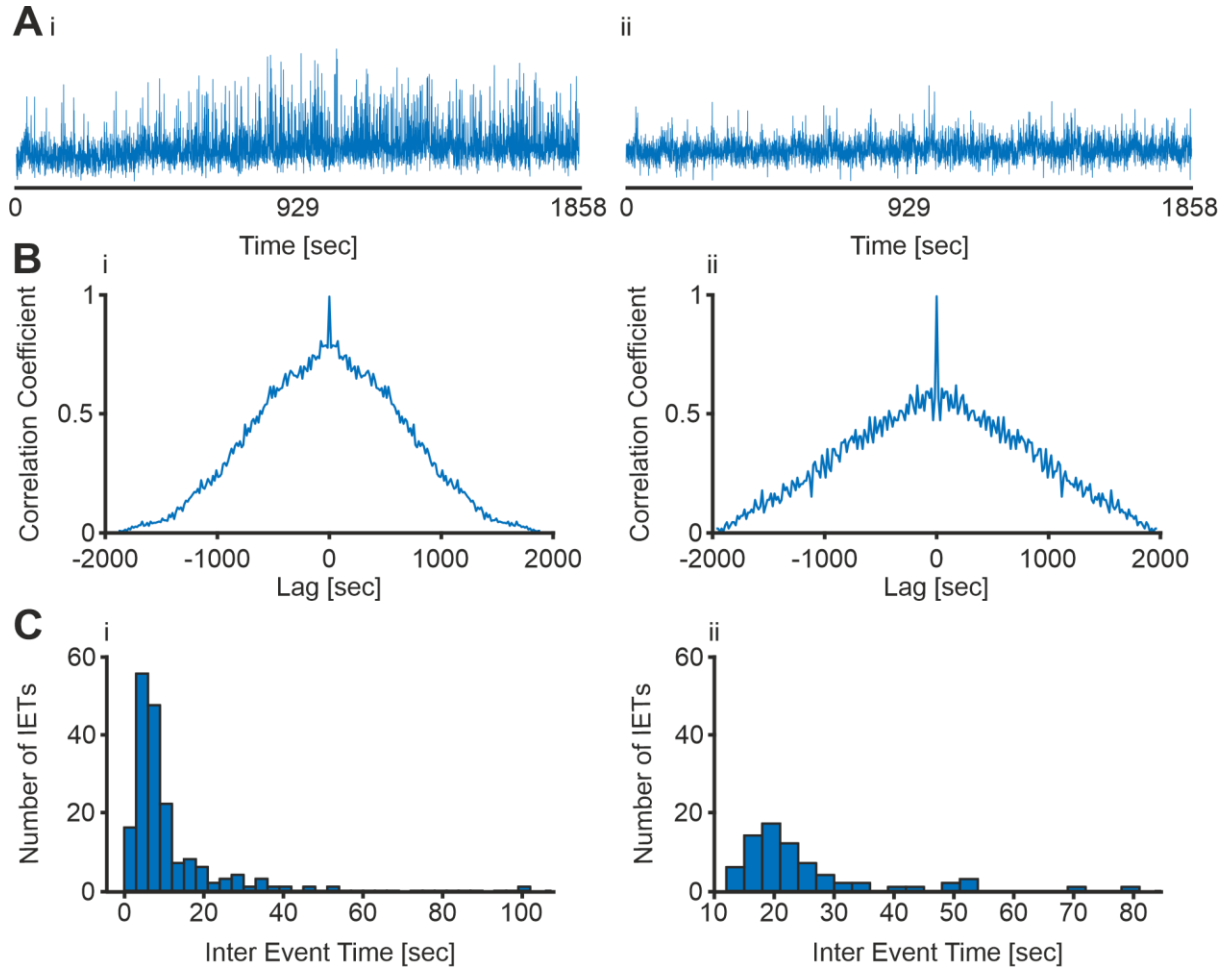


Figure 27: Classification of Irregular Bursting AMCs In Vivo. **A:** Two exemplary traces of two irregular bursting AMCs with different activity patterns (**Ai**, **Aii**). Both traces were recorded over 31 minutes at resting conditions. **B:** Autocorrelation of the AMC in **Ai** (shown in **Bi**) and of the AMC in **Aii** (shown in **Bii**). **C:** Number of inter-event times (IET) between the activity up-states from the AMC in **Ai** (shown in **Ci**) and of the AMC shown in **Aii** (shown in **Cii**). **Ci**, **Cii**: Bin size: 3 seconds.

The COV values for the AMCs shown were 1.069 (Figure 27Ai) and 0.513 (Figure 27Aii), respectively. For all AMCs categorized as irregularly bursting ($n = 17$) the COV range spanned values between 0.5 and 1.1. This distinguishes irregularly bursting from oscillating AMCs. Irregularly bursting AMCs had a somewhat intermediate COV, meaning that IETs showed medium dispersion around the mean. However, since these AMCs displayed patterned activity (i.e., bursting) IET distribution was not random.

Analysing irregularly bursting AMCs in the frequency domain, we observed striking heterogeneity (Figure 28A). Maximum PSD peak showed high diversity (Figure 28B), so did the number of maximum PSD peaks (Figure 28C). Although many irregular bursting AMCs showed a maximum PSD peak between 0.01 and 0.03 Hz, some AMCs

3. Results

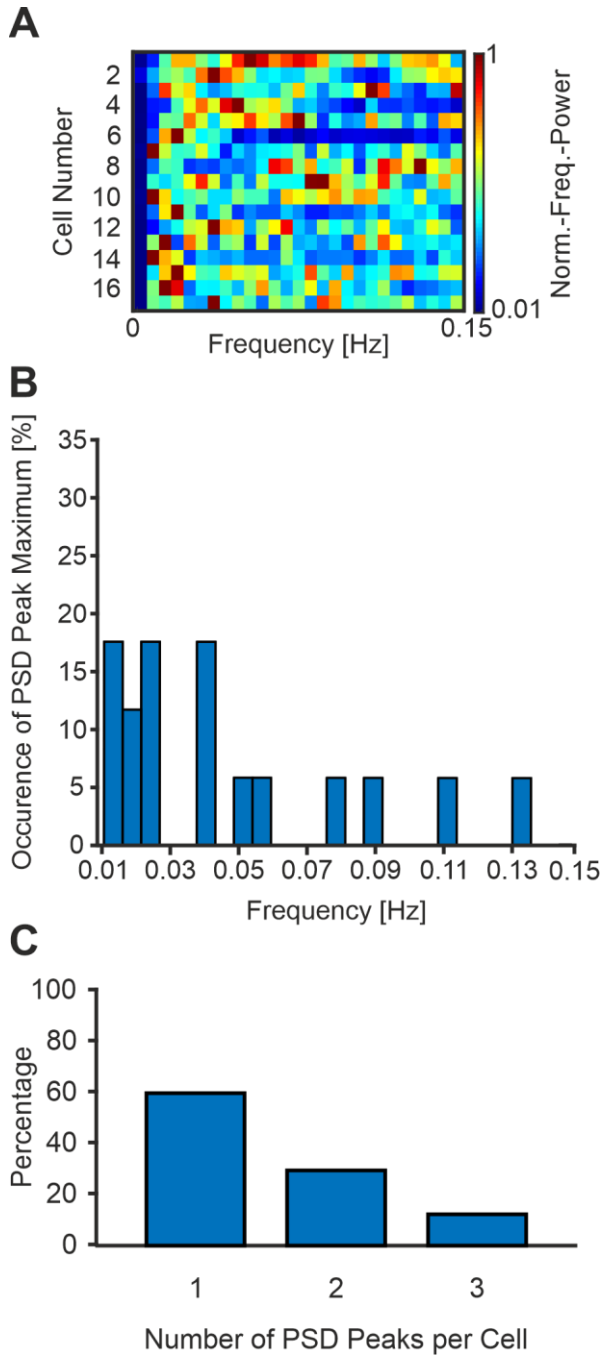


Figure 28: Temporal Domain Properties of Irregular Bursting AMCs. **A:** Power spectral density (PSD) of all oscillating AMCs ($n = 17$) in a frequency range from 0 to 0.15 Hz. The power was normalized to the maximal peak for each AMC. Frequency bin: 0.006 Hz. **B:** Occurrence of PSD peak maximum for every AMC from **A**. Bin size: 0.006 Hz. **C:** Percentage of the number of PSD peaks per AMC. A peak is defined as a normalized power in the PSD spectrum >0.8 . $n = 17$.

had a maximum PSD peak higher than 0.13 Hz. All in all, we observed PSD power values >0.8 over the whole frequency range between 0.01 and 0.15 Hz. Moreover, in comparison to the oscillating AMCs, this neuron population showed up to three maximum PSD peaks with a power >0.8 (Figure 28C).

Taking these findings together, based on unsteady burst-like activity periods over time, this AMC population differs from oscillating AMCs. Irregular activity bursts occur at multiple prominent frequencies.

3. Results

3.2.2.1.3 Irregular Active AOB Mitral Cells

In line with *in vitro* findings, a large population of AMCs was found to be showing an irregular firing pattern in the *in vivo* situation. Here, no clear rhythmic or bursting activity pattern was observed (Figure 29). This AMC population displayed up-states at heterogeneous IETs during continuous 31-minute recordings (Figure 29Ai).

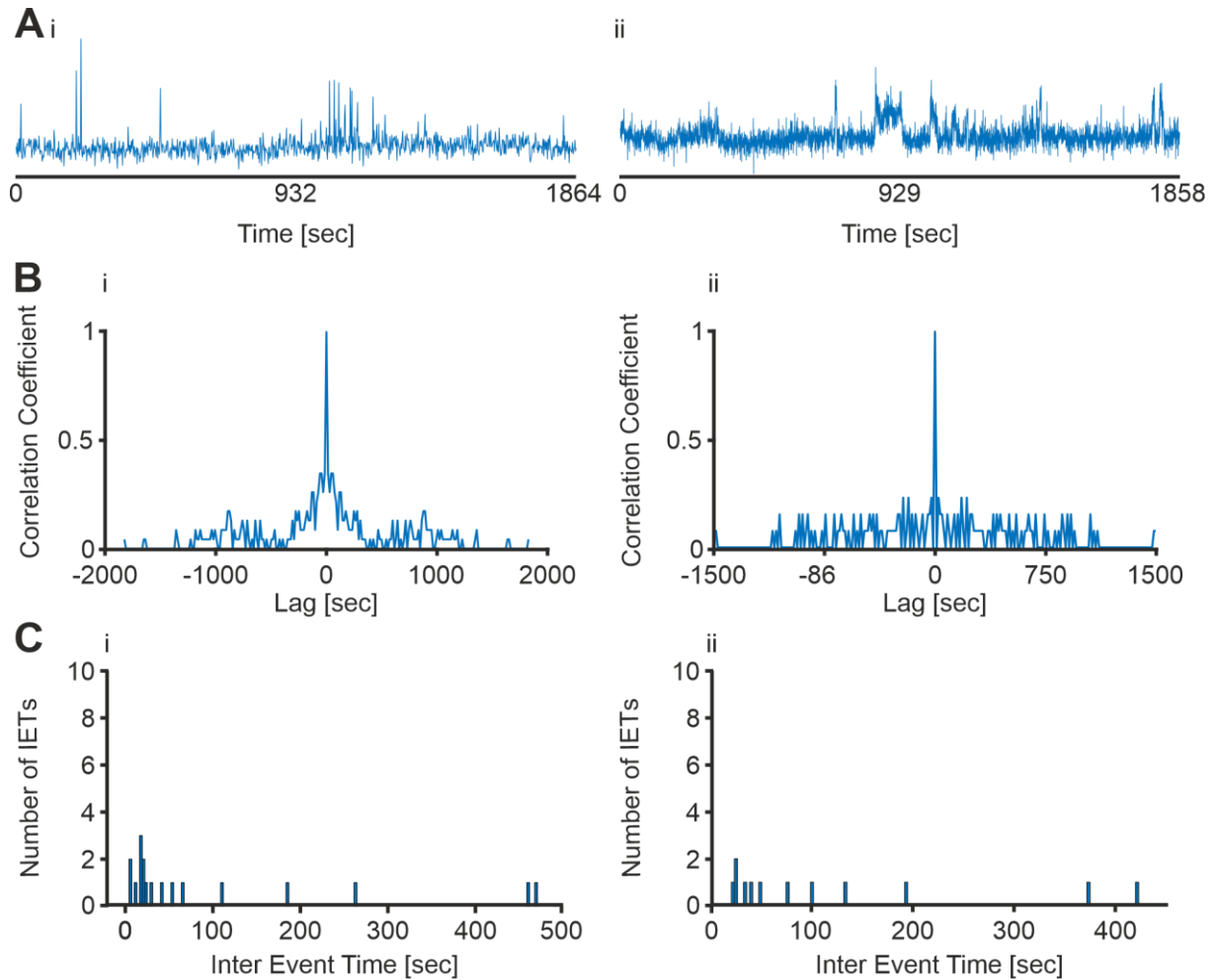


Figure 29: Classification of Irregular Active AMCs In Vivo. **A:** Two exemplary traces of two irregular active AMCs with different activity patterns (**Ai**, **Aii**). Both traces were recorded over 31 minutes at resting conditions. **B:** Autocorrelation of the AMC in **Ai** (shown in **Bi**) and of the AMC in **Aii** (shown in **Bii**). **C:** Number of inter-event times (IET) between the activity up-states from the AMC in **Ai** (shown in **Ci**) and of the AMC shown in **Aii** (shown in **Cii**). **Ci**, **Cii**: Bin size: 3 seconds.

This AMC subtype was distinguished by absence of any analytical parameter that indicates rhythmicity. Accordingly, we did not find prominent side peaks in autocorrelations (Figure 29B) and, furthermore, IETs were largely heterogeneous, indicating absence of reoccurring bursts (Figure 29C). In addition, the durations of IETs

3. Results

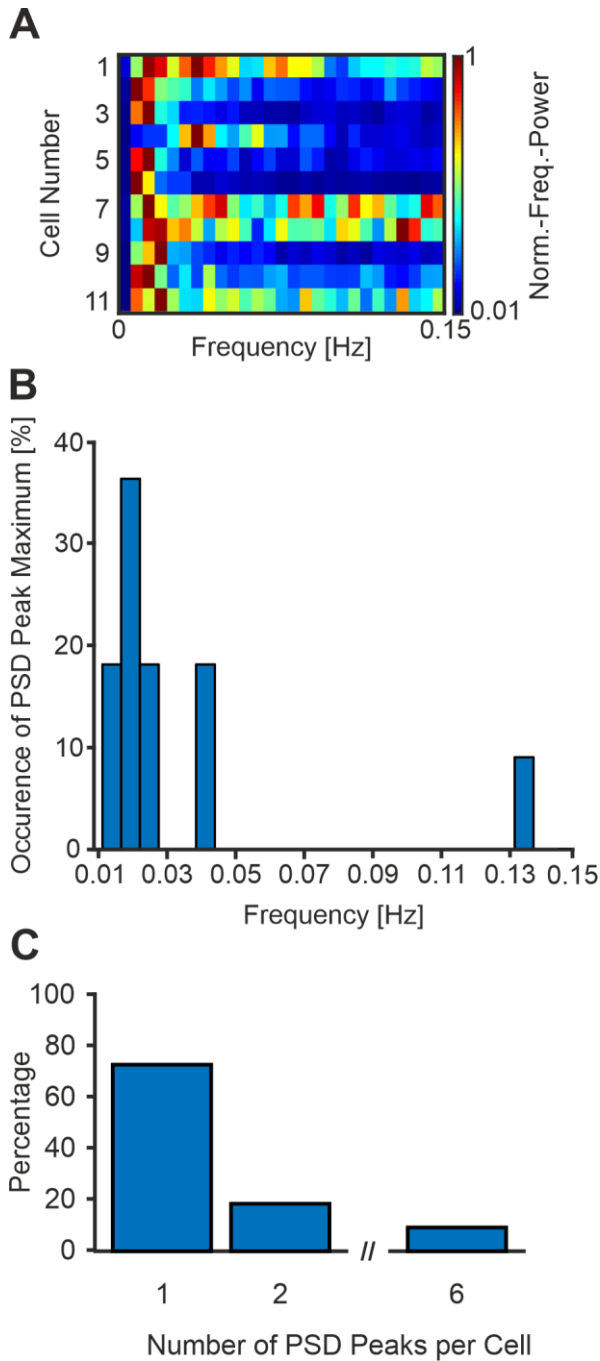


Figure 30: Temporal Domain Properties of Irregular Active AMCs In Vivo. **A:** Power spectral density (PSD) of all oscillating AMCs ($n = 11$) in a frequency range from 0 to 0.15 Hz. The power was normalized to the maximal peak for each AMC. Frequency bin: 0.006 Hz. **B:** Occurrence of PSD peak maximum for every AMC from **A**. Bin size: 0.006 Hz. **C:** Percentage of the number of PSD peaks per AMC. A peak is defined as a normalized power in the PSD spectrum >0.8 . $n = 11$.

were longer in irregular active AMCs (Figure 29C) compared to irregular bursting AMCs (Figure 27C).

The COV of irregular active AMCs was >1.1 . The AMCs shown in Figure 29 had IET distribution COV of 1.489 (Figure 29Ai) and 1.104 (Figure 29Aii), respectively. Such high COV showed that the dispersion around the mean was large, indicating a random distribution in the IET histogram.

Furthermore, we could observe a rather heterogeneous temporal activity pattern for this AMC population (Figure 30A). Here, most AMCs clustered between 0.01 Hz and 0.05 Hz (Figure 30B). In addition, in some cases AMCs of this population showed frequencies higher than 0.13 Hz. A unique feature was the presence of AMCs that showed up to 6 PSD peaks with a power >0.8 (Figure 30C). This underlined the random activity pattern of this neuron population.

Taking these findings together, not all AMCs in the AOB showed rhythmic or bursting physiological phenotypes *in vivo*. A prominent proportion of AMCs showed an irregular firing pattern.

3. Results

3.2.2.1.5 Quantification of AOB Mitral Cell Activity Variability

We showed that AMCs *in vivo* can be distinguished by three distinct activity patterns during their idle state: Oscillating, irregularly bursting, and irregular (Figure 25, Figure 27, Figure 29), respectively. One physiological measure to characterize the individual signal kinetics is to analyse the bursts FWHM (Figure 24Ci, Figure 31). This measure determines the average duration of up-states (and their homo- / heterogeneity).

FWHM analysis revealed that this parameter is significantly different between oscillating and irregularly bursting AMCs (Figure 31, Kruskal-Wallis one-way ANOVA). Oscillating AMCs showed a significantly longer FWHM than irregular bursting AMCs. Note that the longest mean FWHM for one AMC was 91.2 seconds. For irregular bursting cells the longest mean FWHM was 7.3 seconds. In general, oscillating AMCs showed remarkable FWHM variability. The shortest mean FWHM observed for this population was 1.5 seconds.

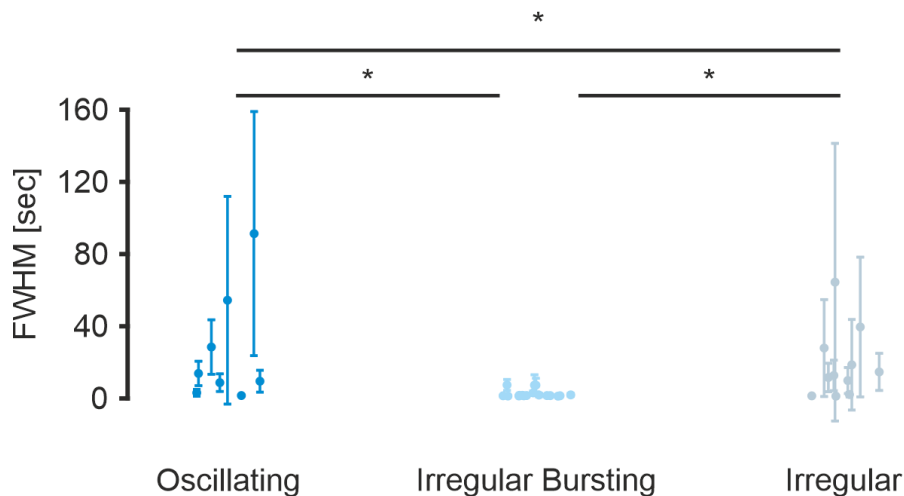


Figure 31: Full Width at Half Maximum Differs Significantly between AMC Phenotypes *In Vivo*. Comparison of full width at half maximum (FWHM) for the three groups of oscillating AMCs (n = 8), irregular bursting AMCs (n = 17) and irregular active AMCs (n = 11). All three groups differ in their FWHM. First, the groups were tested for normal distribution using the Kolmogorov Smirnov test. Second, we tested for significance between the groups using the Kruskal Wallis One-way ANOVA. Each data point is the mean ± SD FWHM for one AMC.

In addition, we found a significant difference between the mean FWHM of irregularly bursting and irregular AMCs *in vivo* (Figure 31, Kruskal-Wallis one-way ANOVA). Irregular AMCs had a significantly longer FWHM than irregular bursting AMCs. For irregular active AMCs the longest mean FWHM was 64.4 seconds, the shortest mean

3. Results

FWHM appeared to be 1.1 seconds. Again, the variability of the FWHM for irregular active AMCs was remarkably high. For irregularly bursting AMCs, however, this variability was small (Figure 31). The shortest mean FWHM was 1.2 seconds, the longest was observed to be 7.3 seconds.

Lastly, we also found a significant difference between oscillating and irregular active AMCs (Figure 31, Kruskal-Wallis one-way ANOVA). Having a significant difference between all three groups in their FWHM again underlines a physiological difference between the AMC populations.

Although many active AMCs showed a stable activity (pattern) over time (Figure 25, Figure 27, Figure 29), some AMCs displayed variable firing (Figure 32A).

For example, a slow activity pattern was changed towards faster activity patterns (Figure 32Ai, Figure 32Bi). This AMC displayed infraslow activity for more than 160 seconds and then changed to fast and more irregular activity. This change could be clearly verified by the change in the PSD (Figure 32Bi). Furthermore, a clear change in the mean FWHM showed a decrease of signal length between the first (27.44 ± 6.35 seconds) and second (2.24 ± 1.15 seconds) pattern (Figure 32C).

In some cases, AMCs changed activity even more often. The AMC shown had six different activity patterns based on PSD and FWHM during an 11-minute recording (Figure 32Aii). The frequencies shown in the PSD varied from infraslow activity up to 0.3 Hz (Figure 32Bii). In addition, clear changes in the FWHM could be observed (Figure 32D). The FWHM between the activity patterns varied from 1.21 ± 0.24 seconds up to 26.29 ± 30.81 seconds.

A clear activity pattern distinction between oscillating, irregular bursting or irregular active for AMCs that frequently change their activity phases, however, was not possible due to the fact, that the periods sometimes are too short to calculate reliable mathematical measures.

3. Results

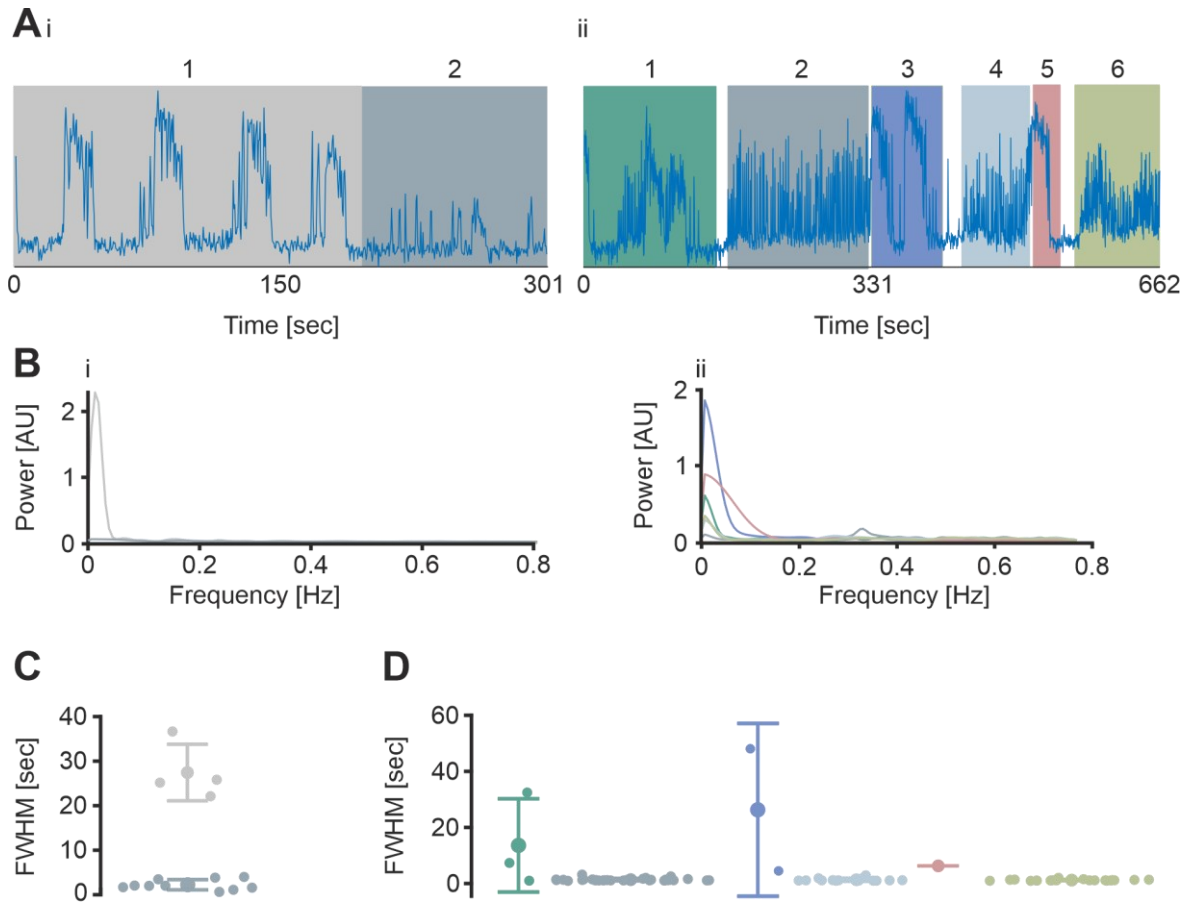


Figure 32: AMCs Show a High Variability in Their Activity Patterns In Vivo. **Ai:** The example AMC shows two different activity patterns within 5 minutes of resting state conditions, indicated by the different colors. **Aii:** The example AMC shows six different activity patterns within 11 minutes of resting state conditions, indicated by the different colors. **Bi:** The power spectra of the AMC shown in **Ai**. The first activity pattern differs from the second activity pattern. **Bii:** The power spectra of the AMC shown in **Aii**. The different time windows analysed differ from each other. Note that the AMC shown changes from slower to faster frequencies and vice versa. **C:** Full width at half maximum (FWHM) from the two activity patterns of the AMC shown in **Ai**. Mean \pm SD: First pattern: 27.44 ± 6.35 seconds, Second pattern: 2.24 ± 1.15 seconds. **D:** Full width at half maximum (FWHM) from the six activity patterns of the AMC shown in **Aii**. Mean \pm SD: First pattern: 13.61 ± 16.63 seconds, Second pattern: 1.38 ± 0.45 seconds, Third pattern: 26.29 ± 30.81 seconds, Fourth pattern: 1.35 ± 0.55 , Fifth pattern: 6.29 ± 0 seconds, Sixth pattern: 1.22 ± 0.24 seconds.

Our observations indicated that a given AMC did not necessarily show stable activity patterns for long periods *in vivo*. In some cases, we observed alternating fast and slow patterns. If this was established by changes in intrinsic activity or via synaptic drive remains elusive. This finding, however, was in line with observations from *in vitro* experiments. According to these findings, the AMCs shown here could be part of more than one microcircuit or they may not be member of any microcircuit.

3.2.2.2 AOB Mitral Cells Show Correlated Activity *In Vivo*

A large proportion of AMCs showed correlated calcium signals *in vitro* (Figure 14, Figure 15), suggesting microcircuits as functional computation units in the AOB. We next asked, whether we find synchronized AMC activity *in vivo*. To tackle this question, we calculated cross-correlations for every continuously active AMC (Figure 33A, $n_{\text{AMC}} = 104$). Comparable to our *in vitro* findings, correlations mostly clustered around a relatively low correlation coefficient. Some AMC pairs, however, showed a high cross-correlation up to a value of 0.75. Fitting gaussian distributions to the histogram yielded three distinct peaks. Of the 104 AMC pairs analysed, 9 AMC pairs clustered in the second and third peak. This means that 8.7% percent of AMC pairs showed higher correlation than the majority of AMCs that cluster in a gaussian distribution that peaks at correlation coefficients between 0.066 and 0.1.

Next, we analysed all experiments in which we recorded more than two continuously active AMCs ($n = 4$ recordings). Among these experiments, we found that examples where all pairwise cross-correlations between continuously active AMCs were relatively low (Figure 33B). However, in one experiment, the cross-correlation between some AMCs was high (Figure 33C). While requiring future confirmation, this indicates that AMCs can organize in correlated ensembles *in vivo*. In this experiment, the three highest correlated AMC pairs had correlation coefficients between 0.66 (Figure 33C, Figure 33D-1,7) and 0.72 (Figure 33C, Figure 33D-1,3).

Since the number of analysed AMCs is low compared to our *in vitro* analysis we did not perform a dedicated microcircuit analysis. AMC *in vivo* cross-correlation results, however, strongly suggest some degree of coordinated idle state activity. This suggests that AMC microcircuits exist not only *in vitro*, but also *in vivo*.

3. Results

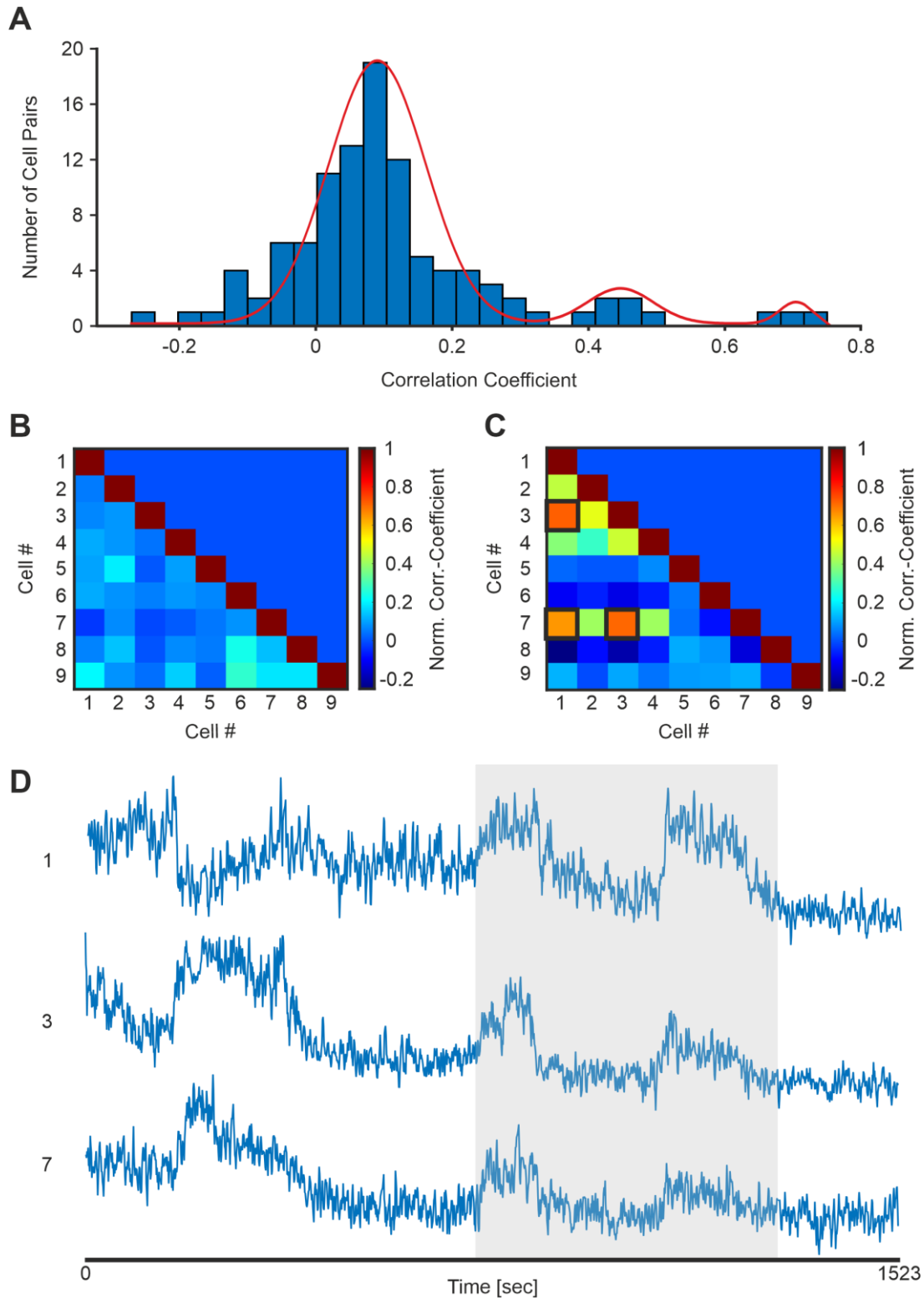


Figure 33: Continuously Active AMCs Show Correlated Activity *In Vivo*. **A:** Number of pairs of AMCs that show a certain correlation coefficient. Each continuously active AMC from one experiment was correlated with the activity of every other AMC. The highest positive cross-correlation coefficient from a sliding window approach with 5-minute window length and 1-minute shift is used. $n = 104$. Bin size: 0.034. Multifitting using gaussian distributions revealed 3 distinct peaks in the distribution. **B:** Cross-correlation matrix of 9 continuously active AMCs derived from an experiment shown in **A**. Note that the average correlation between AMC pairs is low. **C:** Cross-correlation matrix of 9 continuously active AMCs derived from an experiment shown in **A**, including the AMCs from the 3rd distribution peak. Note that the average cross-correlation between AMC pairs is high. Cross-correlation coefficients: AMC 1x3: 0.72; AMC 1x7: 0.66; AMC 3x7: 0.71. **D:** Original traces of the AMCs 1, 3 and 7 from **C** over 25 minutes. The shaded area indicates a period of strong cross-correlation.

4. Discussion

For most mammals, the AOS is indispensable for the detection of chemosensory cues (Mohrhardt *et al.*, 2018). Pheromones enable communication about social hierarchy, endocrine state and individuality (Brennan and Zufall, 2006) on intra- and interspecific levels. In addition, sensing pheromones leads to changes in behaviour or the physiological state of mammals (Chamero, Leinders-Zufall and Zufall, 2012). Many ground-breaking studies showed effects of chemical communication on several behaviours (Bruce, 1959; Luo, Michale S Fee and Katz, 2003; Spehr *et al.*, 2006). Whereas an overlap between the MOS and the AOS in many cases cannot be excluded, it is well-known that many behaviours strongly rely on the detection of pheromones by the AOS (Chamero *et al.*, 2007; Roberts *et al.*, 2010).

Considering the fascinating fact that one chemical reliably elicits the same physiological reaction in a complex living organism leads to a pressing question: How can a sensory system reliably elicit a behavioural or endocrine reaction after detecting a given stimulus? Other senses, like audition, are gated by thalamocortical structures prior to behavioural responses (Niederleitner and Luksch, 2012), although their stimulus space is less multi-dimensional. Chemosensory detection, however, has to extract information from a highly dimensional space and is not previously gated (Tsukahara *et al.*, 2021). How can the AOS reliably control crucial behaviours like mating and aggression on the basis of this information? What are the neurophysiological correlates in the AOS enabling this? Many important questions addressing AOS physiology are unanswered. In this study we characterize neuronal network oscillations in the AOB as a possible coding mechanism in the AOS.

4.1 Calcium Oscillations are a Hallmark of Mitral Cell Network Activity

The AOB is the first processing stage of the AOS after active detection of pheromones by the VNO (Spehr, 2010). Downstream target structures of the AOS, like amygdala and hypothalamus, are directly connected to a behavioural or endocrine output. Therefore, a large proportion of information processing must be done in the AOB. The main projection neurons of the AOB are AMCs. They receive input from VSNs and forward information along the anterior LOT (Larriva-Sahd, 2008). Previous studies investigated the electrophysiological properties of AMCs on a single-cell level *in vitro*

4. Discussion

(Zylbertal *et al.*, 2015; Gorin *et al.*, 2016). A remarkable hallmark of AMC electrical activity was the presence of infraslow recurring depolarisations.

Gorin *et al.* described the percentages of oscillating AMCs *in vitro* to be 69.7%. *In vivo* they found 16.7% of AMCs to be rhythmically active. Both percentages are based on electrophysiological measurements of whole-cell patch clamp experiments or extracellular recordings. In our study, we used the intracellular calcium level of AMCs as a proxy for cell activity and action potential discharge and, therefore, for the electrical activity of a neuron. In *in vitro* calcium imaging experiments, we found $48.7 \pm 23.3\%$ of all AMCs per experiment to be oscillating (Figure 9Bi). In the *in vivo* situation, we observed 29% of all active AMCs to be oscillating (Figure 31). Comparing these two results strongly indicates that results from both techniques are generally pointing into the same direction. This is an important finding for understanding AOB physiology. Each technique has strengths and weaknesses. Single-cell electrophysiology gives detailed information about the electrical activity of one single-cell. The experimenter, however, does not know anything about the state of the network. Calcium imaging *in vitro* and *in vivo* can close this gap. Our study verifies the importance of an oscillating physiological subtype among AMCs.

Furthermore, in both experimental approaches, i.e., electrophysiology and calcium imaging, we see strong quantitative differences between the *in vitro* and *in vivo* condition. The fact that *in vivo* measurements show less oscillating AMCs is pinpointing to effects of possible top-down neuromodulation. In acute brain slices, connections from the periphery, from and to higher brain areas, and sometimes even to / from neighboring neurons are cut (Kepler, Marder and Abbott, 1990). This leads to a network situation with significantly less noise. On the other hand, therefore, we would expect clear-cut robust oscillations to be significantly reduced in *in vivo* recordings that typically display a substantial level of “biological noise”. In addition, cutting the brain in thin slices may change the physiological phenotype of AMCs. This could account for high variability in the percentage of oscillating AMCs between experiments (Figure 9Bi, Figure 9Bii). Independent of their frequency of occurrence, AMC oscillations, however, are a hallmark of AOB network activity both *in vitro* and *in vivo*.

Interestingly, we did not find a significant difference between the percentage of oscillating AMCs in the anterior and posterior AOB (Figure 9Bii). Previous reports described differences in VNO-to-AOB projections along the AOB rostro-caudal axis

4. Discussion

(Rodriguez, Feinstein and Mombaerts, 1999; Larriva-Sahd, 2008). Here, V1R- and V2R-expressing sensory neurons show distinct projections to either anterior or posterior AOB, respectively (Figure 1). Our *in vitro* results suggest that there is no difference in baseline activity of oscillating AMCs along this axis. This leads to the conclusion that, at least without any external input, the AMC network has a common activity state that frequently displays oscillations during the ‘idle’ state, i.e., in absence of sensory input. This finding is even more underlined by the fact, that not only the classification between oscillating or non-oscillating neurons leads to this conclusion. Looking at the temporal domain of these rhythmically active AMCs, we could not observe a difference between the whole population of oscillating AMCs (Figure 11) as compared to either the anterior (Figure 12) or the posterior (Figure 13) population, respectively. All oscillating AMCs were active within the infraslow frequency range between 0.01 Hz and 0.15 Hz. Furthermore, the number of distinct frequency peaks did not differ significantly. Most AMCs showed only one prominent frequency peak, no matter if they are located in the anterior or posterior AOB (Figure 12, Figure 13).

This finding, having a common ground state of oscillatory activity at resting conditions within the whole AMC network, lays the basis for further investigation of possible different coding paradigms of V1R and V2R receptor inputs. Is the reaction of the AMC network upon V1R or V2R activation the same? And, if so, how does the histological separation between the anterior and posterior AOB influence information coding?

Infraslow oscillations are a prominent feature of AMC physiology. This concept is not only supported by the *in vitro* calcium imaging and electrophysiology data, but also by spectral analysis of *in vivo* calcium imaging results. The prominent frequency of all oscillating AMCs analysed *in vivo* was found to be between 0.01 and 0.055 Hz (Figure 26). Within this frequency range, however, peak frequencies were heterogeneous, arguing against a single dominant rhythm. This suggests that AMC activity in the living animal operates on a rather slow timescale as well, supporting previous findings (Yoles-Frenkel, Kahan and Ben-Shaul, 2018).

4. Discussion

4.2 Accessory Olfactory Bulb Network Computation

To compute input from complex environmental cues, network mechanisms must orchestrate single-cell activity on a population level in a meaningful manner. Oscillatory activity, like we observed in many AMCs *in vitro* and *in vivo*, is a widespread mechanism to increase coding capacity of neuronal networks and, thus, occurs across a broad range of frequencies (Buzsáki and Draguhn, 2004). In the AMC network we observed this oscillatory activity to be in the infraslow range. However, prominent frequencies in this temporal space were heterogeneous (Figure 11, Figure 26), adding some degree of flexibility to the system. Accounting for the broad range of possible stimuli we expected a non-heterogeneous frequency distribution. But how can a certain network rhythm enhance the coding capacity of a network? To answer this question, we need to consider what coding capacity is based on: The answer is selectivity. If a certain stimulus can selectively be separated in coding space from another one, we have computational power. Orchestrated neuronal activity was shown to enable this (Fries, 2015). Moreover, spontaneous activity in a network can have strong impact on the received input.

4.2.1 Effects of Oscillatory Activity on Sensory Input

A neuron's dendrite is described to have strong computational power (Gulledge, Kampa and Stuart, 2005). In rat AMCs, action potential backpropagation is known for a long time (Ma, 2004). Thinking about oscillations backpropagating towards the AMCs dendrite and, accordingly, to individual glomeruli, could create periods of lower and higher postsynaptic excitability. The well-studied effect of shunting inhibition, decreasing a neurons excitability by increasing the conductance by depolarisation, could be one possible mechanism (Thorson, 1966). By contrast, recurrent time windows of increased excitability by membrane potential up-states could create "windows-of-opportunity" for facilitated information transfer along the initial AOB relay. Supporting a concept of physiological relevance, rhythmically occurring calcium signals were recently shown to be a prominent hallmark of AOB glomeruli, proven by AMC dendrite calcium imaging *in vivo* (Tsitoura *et al.*, 2020). Since the AOS works on rather slow timescales (Yoles-Frenkel, Kahan and Ben-Shaul, 2018), changing signal detection sensitivity by long pronounced activity bursts combined with long silent periods could tune AMCs to input from the VNO in e.g. times of arousal (Meredith and

4. Discussion

O'Connell, 1979). If the VNO would display a certain rhythmic pumping activity, it could time-lock stimulus uptake to such windows of strong excitability. This could be seen as a possible input gating mechanism. In the hamster, VNO pumping activity *in vivo* was described to be between 0.2 - 0.5 Hz, which would fit the oscillatory tone of the AOB (Meredith, 1994).

4.2.2 Microcircuits as Functional Subnetworks of the Accessory Olfactory Bulb

Aside from modulating the input to the neuronal network, the finding of infra-slow oscillations raises the question how within-network computations are performed. We could find oscillatory activity *in vitro* and *in vivo* (Figure 9, Figure 25). Previous work suggested two subpopulations of oscillating AMCs: neurons developing intrinsic oscillations and AMCs entrained synaptically by local network input (Tsitoura *et al.*, 2020). Intrinsically oscillating AMCs (iAMCs) display this activity pattern based on their ion channel composition. Entrained AMCs (eAMCs) oscillate based on synaptic drive. The default frequency of a network's spontaneous activity is shown to strongly depend on its synaptic wiring (Palva *et al.*, 2000). Hereby, the network's composition based on intrinsically active and entrained neurons can lead to the formation of functionally connected subcircuits.

We used the intracellular calcium level as a proxy for AMC activity. Assuming the existence of subcircuit formation, we analysed *in vitro* calcium signals for indications of orchestrated activity patterns. Indeed, we found temporal correlations that could occur based on a synaptic wiring between iAMCs and eAMCs (Figure 14). The connection between these two populations, that overlap in the frequency domain, could function as an entrained computational unit within the AOB. Indeed, we could prove the existence of these microcircuits in the AOB for the first time (Figure 14, Figure 15). Similar circuit formations were also found in other important brain functions like in sleep and awake state (Crunelli *et al.*, 2018).

Interestingly, we found AMCs with more than one prominent frequency peak that are participating in the rhythm of more than one microcircuit (Figure 14). These neurons could integrate information as members of various different microcircuits.

Furthermore, we found *in vivo* evidence for high correlations between AMCs (Figure 33). In this specific example, we found all oscillating neurons to have one prominent frequency peak, indicating the participation in only one microcircuit (Figure 26).

4. Discussion

However, we could identify a prominent AMC subpopulation that showed burst activity which is not perfectly rhythmic and sometimes even changes its pattern (Figure 27, Figure 32). This cell population often displays more than one prominent frequency peak and was identified as irregular bursting (Figure 28). The high heterogeneity of AMC oscillation frequencies within the infraslow range allows a broad bandwidth to distinguish between external stimuli, if one microcircuit with a given frequency accounts for one detected stimulus. Considering the broad range of possible pheromones to be detected, such adaptation to the biological environment is likely.

Irregular bursting AMCs could serve as neurons that participate in more than one circuit, sharing information between them. The possibility of this additional coding mechanism is supported by the fact that AMCs of a given microcircuit are not necessarily in proximity (Figure 16). Some of them span nearly the whole AOB. These circuits could serve as connecting units between the anterior and posterior AOB, again supporting that the information processing by oscillations is not topographically different based on the different innervation of anterior and posterior AOB. Therefore, microcircuits are a general computation method of the AOB.

This finding is important, since AMC dendrites have the tendency to stay within the borders of the either anterior or posterior part (Del Punta *et al.*, 2002). This is in contrast with the finding that AMC somata do not necessarily stay within these two compartments (Yonekura and Yokoi, 2008). Therefore, it remains elusive if members of a microcircuit target overlapping or identical glomerular subsets. In addition, distinct subtypes of AMCs are described: In the superficial AOB some AMCs have small cell bodies and simple dendritic arborization. Furthermore, in the anterior AOB some AMCs have multiple apical dendritic tufts (Yonekura and Yokoi, 2008). How these two subtypes contribute to microcircuit formation, however, is unclear. Moreover, we cannot exclude a possible spatial clustering of microcircuits along the rostrocaudal axis, since confocal imaging is restriction to a small z-section.

An additional important finding is the physiological separation of AMCs *in vivo* in oscillating (Figure 25), irregular bursting (Figure 27) and irregular (Figure 29) activity patterns. Here, we could distinguish the subtypes based on their autocorrelation, the inter-event time histograms, the coefficient of variation, their temporal domain (Figure 26, Figure 28, Figure 30) and the full width at half maximum (Figure 31). Here, we could proof significant differences in the rhythmicity of their activity and the

4. Discussion

duration of activity up-states. Based on this we hypothesize different physiological functions within the network computation.

Based on our *in vitro* findings (Figure 14), oscillating AMCs *in vivo* most likely would serve in one microcircuit based on their single peak frequency domain. This microcircuit could compute and forward the information of one specific incoming stimulus to higher brain areas. This is further supported by their long signal up-states (Figure 31). This makes activity substantially more resistant to “biological noise”.

Irregular bursting AMCs, characterized by significantly shorter FWHMs (Figure 31) and autocorrelations indicating no rhythmicity (Figure 27), have a bursting phenotype. Here, the burst-behaviour lacks clear rhythmicity (Figure 28). We could, however, detect multiple frequency peaks in the PSDs of these cells. According to the *in vitro* situation (Figure 14), these neurons could function as “bridges” between several AMC ensembles. Here, information could be exchanged between microcircuits. This idea is supported by the notion that some AMCs cross the histological separation between the anterior and posterior AOB (Larriva-Sahd, 2008). If information exchange between these compartments is needed this can only be realised by AMCs that are part of more than one microcircuit. The need for this is further supported, that natural stimuli of the AOS is mostly a chemical blend like urine (Chamero, Leinders-Zufall and Zufall, 2012), than a single molecule. Here, we would activate both, V1R and V2R receptor families, leading to the need of communication between the anterior and posterior AOB.

Lastly, irregular AMCs (Figure 29) still offers the opportunity to forward information reliably if rhythmicity is added to these cells. This could either be achieved by entrainment within the network by iAMCs, or via top-down modulation. In the AOB network context they could serve as “idle” neurons, that can be added to a given microcircuit by neuromodulation to strengthen the circuit’s computational power.

Concluding, our results strongly indicate a physiological relevant separation within the AMC population. Existing literature (Zylbertal *et al.*, 2015; Gao *et al.*, 2017) so far treats AMCs as a more or less homogenous cell population. This is based on the fact, that the AOB is meant to be comparable to the MOB in physiology and therefore nomenclature (Meredith, 1991). Transferring the nomenclature from the MOB to the AOB, however, neglects a possible heterogeneity of neurons in the AOB. Recent work (Gorin *et al.*, 2016; Maksimova *et al.*, 2019; Tsitoura *et al.*, 2020) showed first indications that we largely underestimate the complexity of AMC and GC population. Further underlined by our findings in this study it becomes apparent that AOB

4. Discussion

nomenclature and computation as it is understood so far (Figure 3) most likely is not comprehensive at all. To shed light on this, we need to extend our findings with histological and behavioural work on AMC diversity.

4.2.3 Effects of Oscillatory Activity on Accessory Olfactory Bulb Output

What benefits do rhythmically orchestrated infraslow AMC activity and the formation of microcircuits have for the biology of the individual? From a computational perspective, oscillations with higher frequency would result in high temporal resolution. Pronounced and periodic bursts of activity, however, are perfectly suited to reliably forward a signal, thus, being less sensitive to noise. It is of course well established, that a synchronized synaptic input is more likely to elicit a postsynaptic response (Kogo and Ariel, 1999).

Considering the biological function(s) exerted by the AOS, reliably inducing stereotypic and important behaviours like mating, aggression and maternal care (Brennan and Zufall, 2006), it becomes clear that a reliably computed and forwarded signal is indispensable. The rhythmic bursts are strong hallmarks of activity that will be forwarded to the medial amygdala or the hippocampus. Here, possible downstream targets are known to control slow pulsatile neuroendocrine release, which act on the infraslow timescale. Gonadotrophin-releasing hormone neurons (Chu *et al.*, 2012) or vasopressin (Brown, 2004) are known examples. Furthermore, although the authors do not comment on this finding, electrophysiological responses in the medial amygdala in context of oxytocin signalling show oscillation-like patterns (Yao *et al.*, 2017). These applications for AOB coding, however, only cover a small fraction of AOS endocrine and behavioural outputs. The importance of the system in forming behaviour has just recently been shown, deciphering the labelled line pathway from the detection of ESP1 to the motor output of lordosis in female mice (Ishii *et al.*, 2017).

Here, we show that rhythmic AMC calcium oscillations are a prominent hallmark of AOB physiology (Figure 23, Figure 25). Little, however, is known about its impact on downstream targets. This is most likely due to two factors: First, the field is lacking comprehensive studies of this phenomenon and, second, the coding language can change dramatically along the systems pathway. A prominent example for the change of coding language is found in the MOS. The highly coordinated activity in the MOB is translated in a different, yet not fully understood code in the piriform cortex

4. Discussion

(Pashkovski *et al.*, 2020). Therefore, we need to deepen our knowledge how infraslow oscillations contribute to AOS function.

4.3 Mitral Cell Network Pharmacology

The exact orchestration of the AOB network, especially any (poly)synaptic connectivity between AMCs, is poorly understood (Mohrhardt *et al.*, 2018). Among all synaptic connections, a unique feature of the (A)OB network is the presence of dendrodendritic synapses (Didier *et al.*, 2001; Shepherd *et al.*, 2007). AMCs and GCs share common synapses that on each site both pre- and postsynaptic structures. Projections from AMCs to GCs are glutamatergic and, therefore, excitatory. GCs, on the other hand, forward inhibitory input via GABAergic synapses to AMCs. If an AMC is strongly activated, connected GCs are activated as well. On the other hand, an activated GC can reciprocally inhibit the same AMC, from which it received excitatory input, or other AMCs depending on synaptic connection and synaptic strength of these connections. This could lead to either self- and / or lateral inhibition, well-known mechanisms for contrast enhancement (Price and Powell, 1970) and memory formation (Kaba *et al.*, 1994). Only recently it was shown that the AOB is able to undergo learning mechanisms (Marom *et al.*, 2019). The physiological correlate for this mechanism remains unknown. Since synaptic plasticity is a mechanistic correlate of learning (Antonov *et al.*, 2003), changes in the synaptic weight of the dendrodendritic synapse could have a major effect on AOB activity and therefore learning.

The dendrodendritic synapse, however, is not the only connectivity type, which is found to be important for the AOB network. Recently, Mohrhardt and colleagues counted 21,203 nuclei in the mitral cell layer of a prototypical mouse AOB. 6,842 (32%) of those nuclei were identified as belonging to putative AMCs (Mohrhardt *et al.*, 2018). This means that every AMC can undergo strong local modulation by other AMCs as well as non-AMC neurons in close proximity. Aside from AMCs and GCs the AOB harbours sparse populations of PGCs and JGNs (Figure 3). Summarizing this finding, only four distinct neuron populations are accounting for the reliable computation in the network. Caution should be exerted, however, since each of the four major neuron populations, i.e., AMCs, GCs, PGCs, and JGNs, is mainly classified by morphological and anatomical features. As discussed previously, it is entirely possible, if not likely,

4. Discussion

that genetic clustering and / or physiological categorizations will identify more and maybe different classes of AOB neurons.

We assume that the modulation of a neuron population has a major impact on coding capabilities. We took advantage of *in vitro* calcium imaging, allowing us to observe network modulation by pharmacological agents. Here, we analysed the effect of blocking either inhibition, excitation, or both on the number of oscillating AMCs and their spectral properties.

We did not observe a strong effect of either gabazine (Figure 17), AP5 and NBQX (Figure 18), or all three inhibitors combined (Figure 19) on AMC oscillation frequencies. Previous studies stated that blocking GABA_A receptors does not elicit oscillatory discharge (Zylbertal, Yarom and Wagner, 2017). We found, however, that during such disinhibition a large proportion of AMC started to show oscillations (Figure 17D). This finding points in the direction that inhibition has a modulatory and potentially masking effect on AMC activity. An intrinsic oscillation pattern, or one entrainment by excitatory chemical synapses, could be masked by simultaneous inhibition. In this context, GCs are described to have a strong modulatory effect on AMC activity (Maksimova *et al.*, 2019). Notably, we do not find general synchrony of AMC activity after disinhibition.

We do, however, find that relief from inhibition affects microcircuit formation (Figure 20). Gabazine was the only agent having a significant impact on microcircuit size. This supports our theory that unmasking rhythmic AMC activity by blocking inhibition leads to a recruitment of additional AMCs to already existing microcircuits. GABAergic synapses are not only found between AMCs and GCs. Indeed, previous studies confirmed strong top-down modulation of GABAergic input to the MCL from the bed nucleus of the stria terminalis (Fan and Luo, 2009). This brain area is described to contribute to the modulation of sensory signals depending on the animal's internal state (Dong and Swanson, 2006; Shin, Geerling and Loewy, 2008). In the context of microcircuits as functional computation units of the AOB, the bed nucleus of the stria terminalis could strengthen a microcircuit by increasing the number of AMCs sharing the same temporal domain via reduced GABAergic input. Assuming that a microcircuit is the computation unit for one specific stimulus class, like e.g. predator, this way the system could bind several distinct receptor types to integrate important information.

4. Discussion

Although we see an effect on microcircuit size applying gabazine, we do not see a complete synchronization of the network as described by others (Zylbertal, Yarom and Wagner, 2017). This has two reasons: First, we described synchrony as correlated activity with a lag of ± 5 seconds. Zylbertal *et al.* allowed ± 15 seconds for correlated signals to count as synchronized activity. Even on the slow timescale of the AOS such delays seem rather unphysiological, considering the timescales chemical synapses, and therefore neuronal networks, are working on (Greengard, 2001). Second, we defined a microcircuit as a neuron ensemble where all cells are correlated with each other. Zylbertal and colleagues did not implement a similarly conservative criterion.

Aside from GABA, glutamate is one of the most prominent neurotransmitters driving network activity (Akgül and McBain, 2016). We did not find a significant change in microcircuit size or number after application of AP5 and NBQX (Figure 20). Blocking NMDA, AMPA and kainate receptors, however, did decrease the number of oscillating AMCs *in vitro* (Figure 18D). This pinpoints towards a role of fast excitatory input in the network. The main driving force of AMC network activity, however, remains unclear. This is especially true for the question whether entrainment is direct or indirect. Recent studies performing paired patch-clamp experiments in acute brain slices indicate, that direct coupling between AMCs, either chemically or electrically, is rare (Tsitoura *et al.*, 2020).

Nevertheless, microcircuit formation *in vivo* is most likely influenced by top-down modulation (Mohedano-Moriano *et al.*, 2012; in 't Zandt *et al.*, 2019). Pioneering work suggested input to the AOB network from many different brain areas by different neurotransmitters (Fan and Luo, 2009; Smith and Araneda, 2010a; Huang, Thiebaud and Fadool, 2017).

Two studies indicated the influence of muscarinic acetylcholine receptors (Smith and Araneda, 2010a; Takahashi and Kaba, 2010). This input is provided by neuromodulatory neurons in the horizontal limb of the diagonal band of Broca. The studies showed either an enhanced excitability of GCs directly, or indirectly via stronger glutamatergic input from AMCs. Given our pharmacological results, an increased excitability of GCs could lead to smaller AOB microcircuits, due to the enhanced GABAergic tone in the network.

In addition, serotonin was shown recently to have similar effects to the AOB network via 5-HT₂ metabotropic receptors (Huang, Thiebaud and Fadool, 2017).

4. Discussion

Considering the slower and frequently more persistent timescales of metabotropic receptor signalling (Roth, 2019), this input could be used to change the general network activity on longer timescales.

Moreover, Huang and colleagues showed that faster serotonergic input can inhibit AMCs directly via 5-HT₁ receptors. This could lead to more time-locked changes in AOB network activity. Both effects would also increase the inhibitory tone in the network.

Acting on an even slower timescale, ER- α estrogen receptors located in the bed nucleus of the stria terminalis and the amygdala were shown to project to the AOB (Fan and Luo, 2009). This mechanism could explain how endocrine release might not only be triggered by the AOS, but also influence its activity depending on the state of the animal. Here, one could think about different cycle stage-dependent, mating-related behaviours in female mice. A change in estrogen concentration during the female's cycle in mice is known for a long time (Zysow *et al.*, 1997).

Lastly, electrical coupling is a well-known mechanism entraining oscillatory network activity (Stagkourakis *et al.*, 2018). Studies in the murine AOB proposed, based on modelling and pharmacology, a possible role of gap junctions in AMC coupling (Zylbertal, Yarom and Wagner, 2017). Due to poor selectivity of gap junction inhibitors (Connors, 2012) more studies, either performing paired patch-clamp experiments or using advanced animals models with gap junction deficiency, are needed to proof or falsify this finding.

4.4 Future Directions based on Single-Cell Mitral Cell Calcium Imaging *In Vivo*

Aside from the physiological advances that this study contributes to the field of AOS coding, one major methodological advance is the development of large-scale calcium imaging of AMCs at single-cell resolution *in vivo* (Figure 21, Figure 22, Figure 23). Here, we closed a gap in the toolbox of physiological AMC measurements. So far, whole-cell patch clamp (Zylbertal *et al.*, 2015; Gorin *et al.*, 2016; Cansler, Maksimova and Meeks, 2017; Zylbertal, Yarom and Wagner, 2017; Maksimova *et al.*, 2019), *in vivo* extracellular recordings (Ben-Shaul *et al.*, 2010), *ex vivo* electrophysiological experiments (Meeks and Holy, 2009) and *in vitro* calcium imaging in acute brain slices (Tsitoura *et al.*, 2020) were used to describe AOB physiology. In addition, due to

histological advances like tracing studies (Fan and Luo, 2009) and tissue clearing (Mohrhardt *et al.*, 2018), many questions to the AOS could be already addressed.

However, until now we lacked the opportunity to analyse network activity on a single neuron basis using intracellular calcium as a proxy for cell activity. Here, we combined the selectivity of genetically labelled and identified neurons with the opportunity to observe many neurons at once. Previously, we had to either use acute brain slices for calcium imaging, losing the networks bottom-up and top-down connectivity, or perform extracellular recordings not being able to confirm individual cell identities. Recent advances in the field of implantable optics, like microprisms (Chia and Levene, 2009; Andermann *et al.*, 2013), now made it possible to access brain areas that are not accessible with standard microscopy techniques. Furthermore, we can now monitor AMC activity without harming any brain region that is connected to olfactory processing, like for example the anterior olfactory nucleus.

This study quantifies the basic oscillatory activity of the AOB *in vivo* at single-cell level for the first time. Recent advances in being able to deliver natural stimuli to the system (Ben-Shaul *et al.*, 2010; Yoles-Frenkel *et al.*, 2017) combined with our newly established imaging approach offers the unique opportunity to close major knowledge gaps in the field: How do microcircuits react to natural stimulus delivery? How does the system distinguish between pure pheromone stimuli and pheromone mixtures? Answering these questions will generate an in-depth understanding of AOS functionality.

5. Summary

Controlling social behaviour and endocrine state, the accessory olfactory system is indispensable for most mammals. Here, the AOB represents the first stage of information processing in this important, though relatively reductionist system. Surprisingly, many basic principles of AOB information processing remain elusive.

In this thesis, I showed that the default activity pattern of AMCs, the sole projection neurons in the AOB, is represented by infraslow oscillations both *in vitro* and *in vivo*. *In vitro*, about 50% of AMCs in their idle state showed this periodic activity, whereas we observed this phenomenon in 29% of AMCs *in vivo*.

My data reveal that temporal coupling of AMCs leads to formation of synchronized microcircuits that build functional subunits within the mitral cell layer. These ensembles enable advanced information processing by adding another temporal coding feature. In addition, pronounced rhythmic activity makes information processing more resistant to internal noise, which is of utmost importance for an indispensable system like the AOS. Furthermore, I showed the influence of inhibition via GABAergic synaptic transmission on microcircuit formation. The AOB is a target of GABAergic top-down modulation. My findings indicate a possible influence of centrifugal inputs on microcircuit formation, and therefore on AOB information processing.

In addition, my work enabled AMC large-scale calcium imaging *in vivo* at single-cell resolution for the first time. I observed the presence of correlated network activity *in vivo*, supporting the *in vitro* finding of ensemble activity. Together, this approach, being able to monitor a large population of genetically targeted AMCs simultaneously without harming any olfactory brain area, lays a basis to address many pressing questions in AOS research. Here, I could show the presence of three physiologically different AMC populations: oscillating, irregularly bursting, and irregular. Thereby, I strengthen the emerging insights that AMCs are a rather heterogeneous neuron population. Further investigations, combining the experimental toolbox I established in this thesis with behavioural paradigms, will help to ultimately decipher AOS physiology.

6. References

- Ache, B. W. and Young, J. M. (2005) 'Olfaction: Diverse Species, Conserved Principles', *Neuron*, 48(3), pp. 417–430. doi: 10.1016/j.neuron.2005.10.022.
- Akerboom, J. *et al.* (2013) 'Genetically encoded calcium indicators for multi-color neural activity imaging and combination with optogenetics', *Frontiers in Molecular Neuroscience*, 6. doi: 10.3389/fnmol.2013.00002.
- Akgül, G. and McBain, C. J. (2016) 'Diverse roles for ionotropic glutamate receptors on inhibitory interneurons in developing and adult brain', *The Journal of Physiology*, 594(19), pp. 5471–5490. doi: 10.1113/JP271764.
- Andermann, M. L. *et al.* (2013) 'Chronic Cellular Imaging of Entire Cortical Columns in Awake Mice Using Microprisms', *Neuron*, 80(4), pp. 900–913. doi: 10.1016/j.neuron.2013.07.052.
- Antonov, I. *et al.* (2003) 'Activity-Dependent Presynaptic Facilitation and Hebbian LTP Are Both Required and Interact during Classical Conditioning in Aplysia', *Neuron*, 37(1), pp. 135–147. doi: 10.1016/S0896-6273(02)01129-7.
- Araneda, R. C. (2006) 'Adrenergic Enhancement of Inhibitory Transmission in the Accessory Olfactory Bulb', *Journal of Neuroscience*, 26(12), pp. 3292–3298. doi: 10.1523/JNEUROSCI.4768-05.2006.
- Baum, M. J. (2012) 'Contribution of pheromones processed by the main olfactory system to mate recognition in female mammals', *Frontiers in Neuroanatomy*, 6. doi: 10.3389/fnana.2012.00020.
- Belluscio, L. *et al.* (1999) 'A Map of Pheromone Receptor Activation in the Mammalian Brain', *Cell*, 97(2), pp. 209–220. doi: 10.1016/S0092-8674(00)80731-X.
- Ben-Shaul, Y. *et al.* (2010) 'In vivo vomeronasal stimulation reveals sensory encoding of conspecific and allospecific cues by the mouse accessory olfactory bulb', *Proceedings of the National Academy of Sciences*, 107(11), pp. 5172–5177. doi: 10.1073/pnas.0915147107.
- Bennett, M. V. L. and Zukin, R. S. (2004) 'Electrical coupling and neuronal synchronization in the Mammalian brain.', *Neuron*, 41(4), pp. 495–511. Available at: <http://www.ncbi.nlm.nih.gov/pubmed/14980200>.

6. References

- Berger, H. (1929) 'Über das Elektroenzephalogramm des Menschen.', *European Archives of Psychiatry and Clinical Neuroscience*, 87.1, pp. 527–570.
- Berridge, M. J. (2002) 'The endoplasmic reticulum: a multifunctional signaling organelle', *Cell Calcium*, 32(5–6), pp. 235–249. doi: 10.1016/S0143416002001823.
- Berridge, M. J. (2006) 'Calcium microdomains: Organization and function', *Cell Calcium*, 40(5–6), pp. 405–412. doi: 10.1016/j.ceca.2006.09.002.
- Berridge, M. J., Lipp, P. and Bootman, M. D. (2000) 'The versatility and universality of calcium signalling', *Nature Reviews Molecular Cell Biology*, 1(1), pp. 11–21. doi: 10.1038/35036035.
- Boesveldt, S. and Parma, V. (2021) 'The importance of the olfactory system in human well-being, through nutrition and social behavior', *Cell and Tissue Research*, 383(1), pp. 559–567. doi: 10.1007/s00441-020-03367-7.
- Bootman, M. D. *et al.* (2013) 'Ca²⁺-Sensitive Fluorescent Dyes and Intracellular Ca²⁺ Imaging', *Cold Spring Harbor Protocols*, 2013(2), p. pdb.top066050. doi: 10.1101/pdb.top066050.
- Bootman, M. D. and Berridge, M. J. (1995) 'The elemental principles of calcium signaling', *Cell*, 83(5), pp. 675–678. doi: 10.1016/0092-8674(95)90179-5.
- Boschat, C. *et al.* (2002) 'Pheromone detection mediated by a V1r vomeronasal receptor', *Nature Neuroscience*, 5(12), pp. 1261–1262. doi: 10.1038/nn978.
- Brennan, P. A. and Keverne, E. B. (1997) 'Neural mechanisms of mammalian olfactory learning', *Progress in Neurobiology*, 51(4), pp. 457–481. doi: 10.1016/S0301-0082(96)00069-X.
- Brennan, P. A. and Zufall, F. (2006) 'Pheromonal communication in vertebrates', *Nature*, 444(7117), pp. 308–315. doi: 10.1038/nature05404.
- Broadwell, R. D. and Jacobowitz, D. M. (1976) 'Olfactory relationships of the telencephalon and diencephalon in the rabbit. III. The ipsilateral centrifugal fibers to the olfactory bulbar and retrobulbar formations', *The Journal of Comparative Neurology*, 170(3), pp. 321–345. doi: 10.1002/cne.901700305.

6. References

- Brody, C. D. and Hopfield, J. J. (2003) 'Simple Networks for Spike-Timing-Based Computation, with Application to Olfactory Processing', *Neuron*, 37(5), pp. 843–852. doi: 10.1016/S0896-6273(03)00120-X.
- Brown, C. H. (2004) 'Rhythmogenesis in Vasopressin Cells', *Journal of Neuroendocrinology*, 16(9), pp. 727–739. doi: 10.1111/j.1365-2826.2004.01227.x.
- Bruce, H. M. (1959) 'An Exteroceptive Block to Pregnancy in the Mouse', *Nature*, 184(4680), pp. 105–105. doi: 10.1038/184105a0.
- Buck, L. and Axel, R. (1991) 'A novel multigene family may encode odorant receptors: a molecular basis for odor recognition.', *Cell*, 65(1), pp. 175–87. Available at: <http://www.ncbi.nlm.nih.gov/pubmed/1840504>.
- Buzsáki, G. and Draguhn, A. (2004) 'Neuronal oscillations in cortical networks.', *Science (New York, N.Y.)*, 304(5679), pp. 1926–9. doi: 10.1126/science.1099745.
- Buzsáki, G., Logothetis, N. and Singer, W. (2013) 'Scaling Brain Size, Keeping Timing: Evolutionary Preservation of Brain Rhythms', *Neuron*, 80(3), pp. 751–764. doi: 10.1016/j.neuron.2013.10.002.
- Cansler, H. L., Maksimova, M. A. and Meeks, J. P. (2017) 'Experience-Dependent Plasticity in Accessory Olfactory Bulb Interneurons following Male–Male Social Interaction', *The Journal of Neuroscience*, 37(30), pp. 7240–7252. doi: 10.1523/JNEUROSCI.1031-17.2017.
- Carafoli, E. (1988) 'The Role of Calcium in the Control of Cell Function', in *Integration of Mitochondrial Function*. Boston, MA: Springer US, pp. 475–485. doi: 10.1007/978-1-4899-2551-0_46.
- Catterall, W. A. (2011) 'Voltage-Gated Calcium Channels', *Cold Spring Harbor Perspectives in Biology*, 3(8), pp. a003947–a003947. doi: 10.1101/cshperspect.a003947.
- Chamero, P. *et al.* (2007) 'Identification of protein pheromones that promote aggressive behaviour', *Nature*, 450(7171), pp. 899–902. doi: 10.1038/nature05997.
- Chamero, P. *et al.* (2017) 'Type 3 inositol 1,4,5-trisphosphate receptor is dispensable for sensory activation of the mammalian vomeronasal organ', *Scientific Reports*, 7(1), p. 10260. doi: 10.1038/s41598-017-09638-8.

6. References

- Chamero, P., Leinders-Zufall, T. and Zufall, F. (2012) 'From genes to social communication: Molecular sensing by the vomeronasal organ', *Trends in Neurosciences*. Elsevier Ltd, 35(10), pp. 597–606. doi: 10.1016/j.tins.2012.04.011.
- Cheetham, S. A. *et al.* (2007) 'The genetic basis of individual-recognition signals in the mouse.', *Current biology : CB*, 17(20), pp. 1771–7. doi: 10.1016/j.cub.2007.10.007.
- Chen, T.-W. *et al.* (2013) 'Ultrasensitive fluorescent proteins for imaging neuronal activity', *Nature*, 499(7458), pp. 295–300. doi: 10.1038/nature12354.
- Chia, T. H. and Levene, M. J. (2009) 'Microprisms for In Vivo Multilayer Cortical Imaging', *Journal of Neurophysiology*, 102(2), pp. 1310–1314. doi: 10.1152/jn.91208.2008.
- Chu, Z. *et al.* (2012) 'Two types of burst firing in gonadotrophin-releasing hormone neurones.', *Journal of neuroendocrinology*, 24(7), pp. 1065–77. doi: 10.1111/j.1365-2826.2012.02313.x.
- Ciges, M. *et al.* (1977) 'Ultrastructure of the Organ of Jacobson and Comparative Study with Olfactory Mucosa', *Acta Oto-Laryngologica*, 83(1–6), pp. 47–58. doi: 10.3109/00016487709128812.
- Clapham, D. E. (2007) 'Calcium Signaling', *Cell*, 131(6), pp. 1047–1058. doi: 10.1016/j.cell.2007.11.028.
- Connors, B. W. (2012) 'Tales of a Dirty Drug: Carbenoxolone, Gap Junctions, and Seizures', *Epilepsy Currents*, 12(2), pp. 66–68. doi: 10.5698/1535-7511-12.2.66.
- 'Correlation Methods' (2003) in, pp. 191–213. doi: 10.1016/S0922-3487(08)70227-2.
- Crunelli, V. *et al.* (2018) 'Dual function of thalamic low-vigilance state oscillations: rhythm-regulation and plasticity', *Nature Reviews Neuroscience*, 19(2), pp. 107–118. doi: 10.1038/nrn.2017.151.
- Crunelli, V. and Hughes, S. W. (2010) 'The slow (<1 Hz) rhythm of non-REM sleep: a dialogue between three cardinal oscillators.', *Nature neuroscience*, 13(1), pp. 9–17. doi: 10.1038/nn.2445.

6. References

- Dana, H. *et al.* (2019) 'High-performance calcium sensors for imaging activity in neuronal populations and microcompartments', *Nature Methods*, 16(7), pp. 649–657. doi: 10.1038/s41592-019-0435-6.
- Deak, A. T. *et al.* (2014) 'IP3-mediated STIM1 oligomerization requires intact mitochondrial Ca²⁺ uptake.', *Journal of cell science*, 127(Pt 13), pp. 2944–55. doi: 10.1242/jcs.149807.
- Didier, A. *et al.* (2001) 'A dendrodendritic reciprocal synapse provides a recurrent excitatory connection in the olfactory bulb.', *Proceedings of the National Academy of Sciences of the United States of America*, 98(11), pp. 6441–6. doi: 10.1073/pnas.101126398.
- Dietschi, Q. *et al.* (2013) 'Convergence of FPR-rs3-expressing neurons in the mouse accessory olfactory bulb', *Molecular and Cellular Neuroscience*, 56, pp. 140–147. doi: 10.1016/j.mcn.2013.04.008.
- Dombeck, D. A. *et al.* (2007) 'Imaging Large-Scale Neural Activity with Cellular Resolution in Awake, Mobile Mice', *Neuron*, 56(1), pp. 43–57. doi: 10.1016/j.neuron.2007.08.003.
- Dong, H.-W. and Swanson, L. W. (2006) 'Projections from bed nuclei of the stria terminalis, anteromedial area: Cerebral hemisphere integration of neuroendocrine, autonomic, and behavioral aspects of energy balance', *The Journal of Comparative Neurology*, 494(1), pp. 142–178. doi: 10.1002/cne.20788.
- Dulac, C. and Axel, R. (1995) 'A novel family of genes encoding putative pheromone receptors in mammals.', *Cell*, 83(2), pp. 195–206. Available at: <http://www.ncbi.nlm.nih.gov/pubmed/7585937>.
- Dulac, C. and Wagner, S. (2006) 'Genetic Analysis of Brain Circuits Underlying Pheromone Signaling', *Annual Review of Genetics*, 40(1), pp. 449–467. doi: 10.1146/annurev.genet.39.073003.093937.
- Duvarci, S. and Pare, D. (2014) 'Amygdala Microcircuits Controlling Learned Fear', *Neuron*, 82(5), pp. 966–980. doi: 10.1016/j.neuron.2014.04.042.
- Fan, S. and Luo, M. (2009) 'The organization of feedback projections in a pathway important for processing pheromonal signals', *Neuroscience*, 161(2), pp. 489–500. doi: 10.1016/j.neuroscience.2009.03.065.

6. References

- Ferrero, D. M. *et al.* (2011) 'Detection and avoidance of a carnivore odor by prey', *Proceedings of the National Academy of Sciences*, 108(27), pp. 11235–11240. doi: 10.1073/pnas.1103317108.
- Fries, P. (2015) 'Rhythms for Cognition: Communication through Coherence', *Neuron*, 88(1), pp. 220–235. doi: 10.1016/j.neuron.2015.09.034.
- Galvan, A. and Wichmann, T. (2008) 'Pathophysiology of parkinsonism.', *Clinical neurophysiology : official journal of the International Federation of Clinical Neurophysiology*, 119(7), pp. 1459–74. doi: 10.1016/j.clinph.2008.03.017.
- Gao, Y. *et al.* (2017) 'Neural mechanisms of social learning in the female mouse.', *eLife*, 6. doi: 10.7554/eLife.25421.
- Gee, K. R. *et al.* (2000) 'Chemical and physiological characterization of fluo-4 Ca²⁺-indicator dyes', *Cell Calcium*, 27(2), pp. 97–106. doi: 10.1054/ceca.1999.0095.
- Giorgi, C., Marchi, S. and Pinton, P. (2018) 'The machineries, regulation and cellular functions of mitochondrial calcium', *Nature Reviews Molecular Cell Biology*, 19(11), pp. 713–730. doi: 10.1038/s41580-018-0052-8.
- Gochin, P. M. *et al.* (1994) 'Neural ensemble coding in inferior temporal cortex.', *Journal of neurophysiology*, 71(6), pp. 2325–37. Available at: <http://www.ncbi.nlm.nih.gov/pubmed/7931520>.
- Gorin, M. *et al.* (2016) 'Interdependent Conductances Drive Infralow Intrinsic Rhythmogenesis in a Subset of Accessory Olfactory Bulb Projection Neurons', *Journal of Neuroscience*, 36(11), pp. 3127–3144. doi: 10.1523/JNEUROSCI.2520-15.2016.
- Greengard, P. (2001) 'The Neurobiology of Slow Synaptic Transmission', *Science*, 294(5544), pp. 1024–1030. doi: 10.1126/science.294.5544.1024.
- Greer, P. L. *et al.* (2016) 'A Family of non-GPCR Chemosensors Defines an Alternative Logic for Mammalian Olfaction', *Cell*, 165(7), pp. 1734–1748. doi: 10.1016/j.cell.2016.05.001.
- Grienberger, C. and Konnerth, A. (2012) 'Imaging Calcium in Neurons', *Neuron*, 73(5), pp. 862–885. doi: 10.1016/j.neuron.2012.02.011.

6. References

- Grüneberg, H. (1973) 'A ganglion probably belonging to the N. terminalis system in the nasal mucosa of the mouse.', *Zeitschrift für Anatomie und Entwicklungsgeschichte*, 140(1), pp. 39–52. Available at: <http://www.ncbi.nlm.nih.gov/pubmed/4749131>.
- Gudjohnsen, S. A. H. *et al.* (2015) 'Meningeal Melanocytes in the Mouse: Distribution and Dependence on Mitf', *Frontiers in Neuroanatomy*, 9. doi: 10.3389/fnana.2015.00149.
- Gulledge, A. T., Kampa, B. M. and Stuart, G. J. (2005) 'Synaptic integration in dendritic trees', *Journal of Neurobiology*, 64(1), pp. 75–90. doi: 10.1002/neu.20144.
- Gupta, G. S. *et al.* (2020) 'Prototype algorithm for three-class motor imagery data classification: a step toward development of human–computer interaction-based neuro-aid', in *Smart Biosensors in Medical Care*. Elsevier, pp. 1–28. doi: 10.1016/B978-0-12-820781-9.00001-2.
- Gutiérrez-Castellanos, N. *et al.* (2014) 'The vomeronasal cortex - afferent and efferent projections of the posteromedial cortical nucleus of the amygdala in mice', *European Journal of Neuroscience*, 39(1), pp. 141–158. doi: 10.1111/ejn.12393.
- Haddad, R. *et al.* (2013) 'Olfactory cortical neurons read out a relative time code in the olfactory bulb', *Nature Neuroscience*, 16(7), pp. 949–957. doi: 10.1038/nn.3407.
- Haga-Yamanaka, S. *et al.* (2014) 'Integrated action of pheromone signals in promoting courtship behavior in male mice', *eLife*, 3. doi: 10.7554/eLife.03025.
- Haga-Yamanaka, S., Ma, L. and Yu, C. R. (2015) 'Tuning properties and dynamic range of type 1 vomeronasal receptors', *Frontiers in Neuroscience*, 9. doi: 10.3389/fnins.2015.00244.
- Halpern, M. (2003) 'Structure and function of the vomeronasal system: an update', *Progress in Neurobiology*, 70(3), pp. 245–318. doi: 10.1016/S0301-0082(03)00103-5.
- Halpern, M. and Frumin, N. (1979) 'Roles of the vomeronasal and olfactory systems in prey attack and feeding in adult garter snakes', *Physiology & Behavior*, 22(6), pp. 1183–1189. doi: 10.1016/0031-9384(79)90274-9.

6. References

- Hartung, J. E. and Gold, M. S. (2020) 'GCaMP as an indirect measure of electrical activity in rat trigeminal ganglion neurons', *Cell Calcium*, 89, p. 102225. doi: 10.1016/j.ceca.2020.102225.
- Hayar, A. *et al.* (2004) 'Olfactory bulb glomeruli: external tufted cells intrinsically burst at theta frequency and are entrained by patterned olfactory input.', *The Journal of neuroscience : the official journal of the Society for Neuroscience*, 24(5), pp. 1190–9. doi: 10.1523/JNEUROSCI.4714-03.2004.
- Herrada, G. and Dulac, C. (1997) 'A novel family of putative pheromone receptors in mammals with a topographically organized and sexually dimorphic distribution.', *Cell*, 90(4), pp. 763–73. Available at: <http://www.ncbi.nlm.nih.gov/pubmed/9288755>.
- Hirschi, M. *et al.* (2017) 'Cryo-electron microscopy structure of the lysosomal calcium-permeable channel TRPML3', *Nature*, 550(7676), pp. 411–414. doi: 10.1038/nature24055.
- Huang, Z., Thiebaud, N. and Fadool, D. A. (2017) 'Differential serotonergic modulation across the main and accessory olfactory bulbs', *The Journal of Physiology*, 595(11), pp. 3515–3533. doi: 10.1113/JP273945.
- Hurst, J. L. *et al.* (2001) 'Individual recognition in mice mediated by major urinary proteins', *Nature*, 414(6864), pp. 631–634. doi: 10.1038/414631a.
- in 't Zandt, E. E. *et al.* (2019) 'Centrifugal Innervation of the Olfactory Bulb: A Reappraisal', *eneuro*, 6(1), p. ENEURO.0390-18.2019. doi: 10.1523/ENEURO.0390-18.2019.
- Ishii, K. K. *et al.* (2017) 'A Labeled-Line Neural Circuit for Pheromone-Mediated Sexual Behaviors in Mice', *Neuron*, 95(1), pp. 123-137.e8. doi: 10.1016/j.neuron.2017.05.038.
- Ishii, T., Hirota, J. and Mombaerts, P. (2003) 'Combinatorial Coexpression of Neural and Immune Multigene Families in Mouse Vomeronasal Sensory Neurons', *Current Biology*, 13(5), pp. 394–400. doi: 10.1016/S0960-9822(03)00092-7.
- Isogai, Y. *et al.* (2011) 'Molecular organization of vomeronasal chemoreception', *Nature*, 478(7368), pp. 241–245. doi: 10.1038/nature10437.

6. References

- Kaba, H. *et al.* (1994) 'Induction of an Olfactory Memory by the Activation of a Metabotropic Glutamate Receptor', *Science*, 265(5169), pp. 262–264. doi: 10.1126/science.8023145.
- Kepler, T. B., Marder, E. and Abbott, L. F. (1990) 'The Effect of Electrical Coupling on the Frequency of Model Neuronal Oscillators', *Science*, 248(4951), pp. 83–85. doi: 10.1126/science.2321028.
- Kim, H. *et al.* (2018) 'Mouse Cre-LoxP system: general principles to determine tissue-specific roles of target genes', *Laboratory Animal Research*, 34(4), p. 147. doi: 10.5625/lar.2018.34.4.147.
- Kogo, N. and Ariel, M. (1999) 'Response Attenuation During Coincident Afferent Excitatory Inputs', *Journal of Neurophysiology*, 81(6), pp. 2945–2955. doi: 10.1152/jn.1999.81.6.2945.
- Kolaczowska, E. and Kubes, P. (2013) 'Neutrophil recruitment and function in health and inflammation', *Nature Reviews Immunology*, 13(3), pp. 159–175. doi: 10.1038/nri3399.
- Kondo, M. *et al.* (2017) 'Two-Photon calcium imaging of the medial prefrontal cortex and hippocampus without cortical invasion', *eLife*, 6, pp. 1–20. doi: 10.7554/eLife.26839.
- von Krosigk, M., Bal, T. and McCormick, D. A. (1993) 'Cellular mechanisms of a synchronized oscillation in the thalamus.', *Science (New York, N.Y.)*, 261(5119), pp. 361–4. Available at: <http://www.ncbi.nlm.nih.gov/pubmed/8392750>.
- Lapis, T. J., Penner, M. H. and Lim, J. (2016) 'Humans can taste glucose oligomers independent of the hT1R2/hT1R3 sweet taste receptor', *Chemical Senses*, 41(9), pp. 755–762. doi: 10.1093/chemse/bjw088.
- Larriva-Sahd, J. (2008) 'The accessory olfactory bulb in the adult rat: A cytological study of its cell types, neuropil, neuronal modules, and interactions with the main olfactory system', *Journal of Comparative Neurology*, 510(3), pp. 309–350. doi: 10.1002/cne.21790.
- LE, Y., MURPHY, P. and WANG, J. (2002) 'Formyl-peptide receptors revisited', *Trends in Immunology*, 23(11), pp. 541–548. doi: 10.1016/S1471-4906(02)02316-5.

6. References

- Lee, K. P. *et al.* (2010) 'STIM1-dependent and STIM1-independent Function of Transient Receptor Potential Canonical (TRPC) Channels Tunes Their Store-operated Mode', *Journal of Biological Chemistry*, 285(49), pp. 38666–38673. doi: 10.1074/jbc.M110.155036.
- Leinders-Zufall, T. *et al.* (2004) 'MHC Class I Peptides as Chemosensory Signals in the Vomeronasal Organ', *Science*, 306(5698), pp. 1033–1037. doi: 10.1126/science.1102818.
- Liberles, S. D. *et al.* (2009) 'Formyl peptide receptors are candidate chemosensory receptors in the vomeronasal organ', *Proceedings of the National Academy of Sciences*, 106(24), pp. 9842–9847. doi: 10.1073/pnas.0904464106.
- Liberles, S. D. and Buck, L. B. (2006) 'A second class of chemosensory receptors in the olfactory epithelium.', *Nature*, 442(7103), pp. 645–50. doi: 10.1038/nature05066.
- Lin, D. Y. *et al.* (2005) 'Encoding social signals in the mouse main olfactory bulb.', *Nature*, 434(7032), pp. 470–7. doi: 10.1038/nature03414.
- Lisman, J. (1997) 'Bursts as a unit of neural information: making unreliable synapses reliable', *Trends in Neurosciences*, 20(1), pp. 38–43. doi: 10.1016/S0166-2236(96)10070-9.
- Lisman, J. E. (1999) 'Relating hippocampal circuitry to function: recall of memory sequences by reciprocal dentate-CA3 interactions.', *Neuron*, 22(2), pp. 233–42. Available at: <http://www.ncbi.nlm.nih.gov/pubmed/10069330>.
- Liu, S. and Shipley, M. T. (2008) 'Multiple conductances cooperatively regulate spontaneous bursting in mouse olfactory bulb external tufted cells.', *The Journal of neuroscience : the official journal of the Society for Neuroscience*, 28(7), pp. 1625–39. doi: 10.1523/JNEUROSCI.3906-07.2008.
- Llinás, R. R. (1988) 'The intrinsic electrophysiological properties of mammalian neurons: insights into central nervous system function.', *Science (New York, N.Y.)*, 242(4886), pp. 1654–64. Available at: <http://www.ncbi.nlm.nih.gov/pubmed/3059497>.
- Losacco, J. *et al.* (2020) 'Learning improves decoding of odor identity with phase-referenced oscillations in the olfactory bulb', *eLife*, 9. doi: 10.7554/eLife.52583.

6. References

- Luo, M., Fee, Michale S. and Katz, L. C. (2003) 'Encoding Pheromonal Signals in the Accessory Olfactory Bulb of Behaving Mice', *Science*, 299(5610), pp. 1196–1201. doi: 10.1126/science.1082133.
- Lytton, J. *et al.* (1992) 'Functional comparisons between isoforms of the sarcoplasmic or endoplasmic reticulum family of calcium pumps.', *The Journal of biological chemistry*, 267(20), pp. 14483–9. Available at: <http://www.ncbi.nlm.nih.gov/pubmed/1385815>.
- Ma, J. (2004) 'Action Potential Backpropagation and Multiglomerular Signaling in the Rat Vomeronasal System', *Journal of Neuroscience*, 24(42), pp. 9341–9352. doi: 10.1523/JNEUROSCI.1782-04.2004.
- Maksimova, M. A. *et al.* (2019) 'Interneuron Functional Diversity in the Mouse Accessory Olfactory Bulb', *eneuro*, 6(4), p. ENEURO.0058-19.2019. doi: 10.1523/ENEURO.0058-19.2019.
- Manzini, I., Schild, D. and Di Natale, C. (2022) 'Principles of odor coding in vertebrates and artificial chemosensory systems', *Physiological Reviews*, 102(1), pp. 61–154. doi: 10.1152/physrev.00036.2020.
- Mao, T. *et al.* (2008) 'Characterization and Subcellular Targeting of GCaMP-Type Genetically-Encoded Calcium Indicators', *PLoS ONE*. Edited by E. Greene, 3(3), p. e1796. doi: 10.1371/journal.pone.0001796.
- Marder, E. and Bucher, D. (2001) 'Central pattern generators and the control of rhythmic movements', *Current Biology*, 11(23), pp. R986–R996. doi: 10.1016/S0960-9822(01)00581-4.
- Marom, K. *et al.* (2019) 'The Vomeronasal System Can Learn Novel Stimulus Response Pairings', *Cell Reports*, 27(3), pp. 676-684.e6. doi: 10.1016/j.celrep.2019.03.042.
- Martinez-Marcos, A. (2009) 'On the organization of olfactory and vomeronasal cortices', *Progress in Neurobiology*, 87(1), pp. 21–30. doi: 10.1016/j.pneurobio.2008.09.010.
- Matsunami, H. and Buck, L. B. (1997) 'A multigene family encoding a diverse array of putative pheromone receptors in mammals.', *Cell*, 90(4), pp. 775–84. Available at: <http://www.ncbi.nlm.nih.gov/pubmed/9288756>.

6. References

- Meeks, J. P. and Holy, T. E. (2009) 'An ex vivo preparation of the intact mouse vomeronasal organ and accessory olfactory bulb', *Journal of Neuroscience Methods*, 177(2), pp. 440–447. doi: 10.1016/j.jneumeth.2008.11.013.
- Meisami, E. and Bhatnagar, K. P. (1998) 'Structure and diversity in mammalian accessory olfactory bulb.', *Microscopy research and technique*, 43(6), pp. 476–99. doi: 10.1002/(SICI)1097-0029(19981215)43:6<476::AID-JEMT2>3.0.CO;2-V.
- Meredith, M. *et al.* (1980) 'Vomeronasal pump: significance for male hamster sexual behavior.', *Science (New York, N.Y.)*, 207(4436), pp. 1224–6. Available at: <http://www.ncbi.nlm.nih.gov/pubmed/7355286>.
- Meredith, M. (1991) 'Sensory processing in the main and accessory olfactory systems: Comparisons and contrasts', *The Journal of Steroid Biochemistry and Molecular Biology*, 39(4), pp. 601–614. doi: 10.1016/0960-0760(91)90258-7.
- Meredith, M. (1994) 'Chronic recording of vomeronasal pump activation in awake behaving hamsters.', *Physiology & behavior*, 56(2), pp. 345–54. Available at: <http://www.ncbi.nlm.nih.gov/pubmed/7938248>.
- Meredith, M. and O'Connell, R. J. (1979) 'Efferent control of stimulus access to the hamster vomeronasal organ.', *The Journal of Physiology*, 286(1), pp. 301–316. doi: 10.1113/jphysiol.1979.sp012620.
- Messina, A. *et al.* (2012) 'VDAC isoforms in mammals', *Biochimica et Biophysica Acta (BBA) - Biomembranes*, 1818(6), pp. 1466–1476. doi: 10.1016/j.bbamem.2011.10.005.
- Minsky, M. (1988) 'Memoir on inventing the confocal scanning microscope', *Scanning*, 10(4), pp. 128–138. doi: 10.1002/sca.4950100403.
- Mizuseki, K. *et al.* (2009) 'Theta Oscillations Provide Temporal Windows for Local Circuit Computation in the Entorhinal-Hippocampal Loop', *Neuron*, 64(2), pp. 267–280. doi: 10.1016/j.neuron.2009.08.037.
- Mohedano-Moriano, A. *et al.* (2012) 'Centrifugal telencephalic afferent connections to the main and accessory olfactory bulbs', *Frontiers in Neuroanatomy*, 6. doi: 10.3389/fnana.2012.00019.

6. References

- Mohrhardt, J. *et al.* (2018) 'Signal Detection and Coding in the Accessory Olfactory System', *Chemical Senses*, 43(9), pp. 667–695. doi: 10.1093/chemse/bjy061.
- Mombaerts, P. (2004) 'Genes and ligands for odorant, vomeronasal and taste receptors', *Nature Reviews Neuroscience*, 5(4), pp. 263–278. doi: 10.1038/nrn1365.
- Mori, K. (1987) 'Membrane and synaptic properties of identified neurons in the olfactory bulb', *Progress in Neurobiology*, 29(3), pp. 275–320. doi: 10.1016/0301-0082(87)90024-4.
- Müller, J. P. (1826) 'Über die phantastischen Gesichterscheinungen', *Hölscher Verlag*, 1.
- Munger, S. D. (2009) 'Noses within noses', *Nature*, 459(7246), pp. 521–522. doi: 10.1038/459521a.
- Nakai, J., Ohkura, M. and Imoto, K. (2001) 'A high signal-to-noise Ca²⁺ probe composed of a single green fluorescent protein', *Nature Biotechnology*, 19(2), pp. 137–141. doi: 10.1038/84397.
- Narayanan, N. S. and Laubach, M. (2009) 'Methods for Studying Functional Interactions Among Neuronal Populations', in, pp. 135–165. doi: 10.1007/978-1-59745-543-5_7.
- NEHER, E. and SAKMANN, B. (1976) 'Single-channel currents recorded from membrane of denervated frog muscle fibres', *Nature*, 260(5554), pp. 799–802. doi: 10.1038/260799a0.
- Ngai, J. *et al.* (1993) 'The Family of Genes Encoding Odorant Receptors in the Channel Catfish', 72, pp. 657–666.
- Niederleitner, B. and Luksch, H. (2012) 'Neuronal morphology in subdivisions of the inferior colliculus of chicken (*Gallus gallus*).', *Journal of chemical neuroanatomy*, 44(1), pp. 24–33. doi: 10.1016/j.jchemneu.2012.03.004.
- Oboti, L. *et al.* (2018) 'Amygdala Corticofugal Input Shapes Mitral Cell Responses in the Accessory Olfactory Bulb', *eneuro*, 5(3), p. ENEURO.0175-18.2018. doi: 10.1523/ENEURO.0175-18.2018.

6. References

- Orrenius, S., Zhivotovsky, B. and Nicotera, P. (2003) 'Regulation of cell death: the calcium–apoptosis link', *Nature Reviews Molecular Cell Biology*, 4(7), pp. 552–565. doi: 10.1038/nrm1150.
- Pachitariu, M. *et al.* (2017) 'Suite2p: beyond 10,000 neurons with standard two-photon microscopy. bioRxiv', *Bioarxiv*, 20, p. 2017.
- Palva, J. M. *et al.* (2000) 'Fast Network Oscillations in the Newborn Rat Hippocampus In Vitro', *The Journal of Neuroscience*, 20(3), pp. 1170–1178. doi: 10.1523/JNEUROSCI.20-03-01170.2000.
- Pashkovski, S. L. *et al.* (2020) 'Structure and flexibility in cortical representations of odour space', *Nature*, 583(7815), pp. 253–258. doi: 10.1038/s41586-020-2451-1.
- PRICE, J. L. and POWELL, T. P. S. (1970) 'The Synaptology of the Granule Cells of the Olfactory Bulb', *Journal of Cell Science*, 7(1), pp. 125–155. doi: 10.1242/jcs.7.1.125.
- Del Punta, K. *et al.* (2002) 'A divergent pattern of sensory axonal projections is rendered convergent by second-order neurons in the accessory olfactory bulb', *Neuron*, 35(6), pp. 1057–1066. doi: 10.1016/S0896-6273(02)00904-2.
- Ringer, S. (1883) 'A further Contribution regarding the influence of the different Constituents of the Blood on the Contraction of the Heart', *The Journal of Physiology*, 4(1), pp. 29–42. doi: 10.1113/jphysiol.1883.sp000120.
- Rivière, S. *et al.* (2009) 'Formyl peptide receptor-like proteins are a novel family of vomeronasal chemosensors.', *Nature*, 459(7246), pp. 574–7. doi: 10.1038/nature08029.
- Roberts, S. A. *et al.* (2010) 'Darcin: A male pheromone that stimulates female memory and sexual attraction to an individual male's odour', *BMC Biology*, 8. doi: 10.1186/1741-7007-8-75.
- Rodolfo-Masera, T. (1943) 'Su l'esistenza di un particolare organo olfattivo nel setto nasale della cavia e di altri roditori.', *Arch Ital Anat Embryol*, 48, pp. 157–212.
- Rodriguez, I., Feinstein, P. and Mombaerts, P. (1999) 'Variable Patterns of Axonal Projections of Sensory Neurons in the Mouse Vomeronasal System', *Cell*, 97(2), pp. 199–208. doi: 10.1016/S0092-8674(00)80730-8.

6. References

- Roppolo, D. *et al.* (2007) 'Gene cluster lock after pheromone receptor gene choice', *The EMBO Journal*, 26(14), pp. 3423–3430. doi: 10.1038/sj.emboj.7601782.
- Roth, B. L. (2019) 'Molecular pharmacology of metabotropic receptors targeted by neuropsychiatric drugs', *Nature Structural & Molecular Biology*, 26(7), pp. 535–544. doi: 10.1038/s41594-019-0252-8.
- Ryba, N. J. and Tirindelli, R. (1997) 'A new multigene family of putative pheromone receptors.', *Neuron*, 19(2), pp. 371–9. Available at: <http://www.ncbi.nlm.nih.gov/pubmed/9292726>.
- Salazar, I. *et al.* (2006) 'General organization of the perinatal and adult accessory olfactory bulb in mice', *The Anatomical Record Part A: Discoveries in Molecular, Cellular, and Evolutionary Biology*, 288A(9), pp. 1009–1025. doi: 10.1002/ar.a.20366.
- Scalia, F. and Winans, S. S. (1975) 'The differential projections of the olfactory bulb and accessory olfactory bulb in mammals', *The Journal of Comparative Neurology*, 161(1), pp. 31–55. doi: 10.1002/cne.901610105.
- Schaefer, A. T. *et al.* (2006) 'Neuronal oscillations enhance stimulus discrimination by ensuring action potential precision.', *PLoS biology*, 4(6), p. e163. doi: 10.1371/journal.pbio.0040163.
- Schatzmann, H. J. (1966) 'ATP-dependent Ca⁺⁺-Extrusion from human red cells', *Experientia*, 22(6), pp. 364–365. doi: 10.1007/BF01901136.
- Schoppa, N. E. *et al.* (1998) 'Dendrodendritic Inhibition in the Olfactory Bulb Is Driven by NMDA Receptors', *The Journal of Neuroscience*, 18(17), pp. 6790–6802. doi: 10.1523/JNEUROSCI.18-17-06790.1998.
- Schoppa, N. E. and Urban, N. N. (2003) 'Dendritic processing within olfactory bulb circuits', *Trends in Neurosciences*, 26(9), pp. 501–506. doi: 10.1016/S0166-2236(03)00228-5.
- Schroeder, C. E. and Lakatos, P. (2009) 'Low-frequency neuronal oscillations as instruments of sensory selection.', *Trends in neurosciences*, 32(1), pp. 9–18. doi: 10.1016/j.tins.2008.09.012.

6. References

- Shepherd, G. M. *et al.* (2007) 'The olfactory granule cell: from classical enigma to central role in olfactory processing.', *Brain research reviews*, 55(2), pp. 373–82. doi: 10.1016/j.brainresrev.2007.03.005.
- Shin, J.-W., Geerling, J. C. and Loewy, A. D. (2008) 'Inputs to the ventrolateral bed nucleus of the stria terminalis', *The Journal of Comparative Neurology*, 511(5), pp. 628–657. doi: 10.1002/cne.21870.
- SLATER, E. C. and CLELAND, K. W. (1953) 'The calcium content of isolated heart-muscle sarcosomes.', *The Biochemical journal*, 54(3), p. xxii. Available at: <http://www.ncbi.nlm.nih.gov/pubmed/13058943>.
- Smith, R. S. and Araneda, R. C. (2010a) 'Cholinergic Modulation of Neuronal Excitability in the Accessory Olfactory Bulb', *Journal of Neurophysiology*, 104(6), pp. 2963–2974. doi: 10.1152/jn.00446.2010.
- Spehr, M. *et al.* (2006) 'Parallel processing of social signals by the mammalian main and accessory olfactory systems.', *Cellular and molecular life sciences : CMLS*, 63(13), pp. 1476–84. doi: 10.1007/s00018-006-6109-4.
- Spehr, M. (2010) 'Sniffing out social signals', *e-Neuroforum*, 1(1), pp. 9–16. doi: 10.1007/s13295-010-0002-1.
- Stagkourakis, S. *et al.* (2018) 'Network oscillation rules imposed by species-specific electrical coupling', *eLife*, 7. doi: 10.7554/eLife.33144.
- Steriade, M., McCormick, D. A. and Sejnowski, T. J. (1993) 'Thalamocortical oscillations in the sleeping and aroused brain.', *Science (New York, N. Y.)*, 262(5134), pp. 679–85. Available at: <http://www.ncbi.nlm.nih.gov/pubmed/8235588>.
- Stowers, L. and Liberles, S. D. (2016) 'State-dependent responses to sex pheromones in mouse', *Current Opinion in Neurobiology*, 38, pp. 74–79. doi: 10.1016/j.conb.2016.04.001.
- Stringer, C. and Pachitariu, M. (2019) 'Computational processing of neural recordings from calcium imaging data', *Current Opinion in Neurobiology*, 55, pp. 22–31. doi: 10.1016/j.conb.2018.11.005.

6. References

- Takahashi, Y. and Kaba, H. (2010) 'Muscarinic receptor type 1 (M1) stimulation, probably through KCNQ/Kv7 channel closure, increases spontaneous GABA release at the dendrodendritic synapse in the mouse accessory olfactory bulb', *Brain Research*, 1339, pp. 26–40. doi: 10.1016/j.brainres.2010.03.104.
- Takami, S. and Graziadei, P. P. C. (1991) 'Light microscopic golgi study of mitral/tufted cells in the accessory olfactory bulb of the adult rat', *The Journal of Comparative Neurology*, 311(1), pp. 65–83. doi: 10.1002/cne.903110106.
- Tazir, B. et al. (2016) 'The extremely broad odorant response profile of mouse olfactory sensory neurons expressing the odorant receptor MOR256-17 includes trace amine-associated receptor ligands', *European Journal of Neuroscience*, 43(5), pp. 608–617. doi: 10.1111/ejn.13153.
- Thorson, J. (1966) 'Small-signal analysis of a visual reflex in the locust', *Kybernetik*, 3(2), pp. 53–66. doi: 10.1007/BF00299898.
- Tirindelli, R. et al. (2009) 'From pheromones to behavior.', *Physiological reviews*, 89(3), pp. 921–56. doi: 10.1152/physrev.00037.2008.
- Trotier, D. and Doving, K. B. (1998) "'Anatomical description of a new organ in the nose of domesticated animals" by Ludvig Jacobson (1813)', *Chemical Senses*, 23(6), p. 743. doi: 10.1093/chemse/23.6.743.
- Tsien, R. Y. (1980) 'New calcium indicators and buffers with high selectivity against magnesium and protons: design, synthesis, and properties of prototype structures', *Biochemistry*, 19(11), pp. 2396–2404. doi: 10.1021/bi00552a018.
- Tsien, R. Y. (1981) 'A non-disruptive technique for loading calcium buffers and indicators into cells', *Nature*, 290(5806), pp. 527–528. doi: 10.1038/290527a0.
- Tsitoura, C. et al. (2020) 'Synchronous infra-slow oscillations organize ensembles of accessory olfactory bulb projection neurons into distinct microcircuits', *Journal of Neuroscience*, 40(21), pp. 4203–4218. doi: 10.1523/JNEUROSCI.2925-19.2020.
- Tsukahara, T. et al. (2021) 'A transcriptional rheostat couples past activity to future sensory responses', *Cell*, 184(26), pp. 6326–6343.e32. doi: 10.1016/j.cell.2021.11.022.

6. References

- Vargas-Barroso, V. *et al.* (2016) 'Electrophysiological Evidence for a Direct Link between the Main and Accessory Olfactory Bulbs in the Adult Rat', *Frontiers in Neuroscience*, 9. doi: 10.3389/fnins.2015.00518.
- Vierra, N. C. and Trimmer, J. S. (2022) 'Ion Channel Partnerships: Odd and Not-So-Odd Couples Controlling Neuronal Ion Channel Function', *International Journal of Molecular Sciences*, 23(4), p. 1953. doi: 10.3390/ijms23041953.
- Vilela, M. *et al.* (2013) 'Fluctuation Analysis of Activity Biosensor Images for the Study of Information Flow in Signaling Pathways', in, pp. 253–276. doi: 10.1016/B978-0-12-405539-1.00009-9.
- Wagner, S. *et al.* (2006) 'A Multireceptor Genetic Approach Uncovers an Ordered Integration of VNO Sensory Inputs in the Accessory Olfactory Bulb', *Neuron*, 50(5), pp. 697–709. doi: 10.1016/j.neuron.2006.04.033.
- White, C. and McGeown, G. (2002) 'Imaging of changes in sarcoplasmic reticulum [Ca²⁺] using Oregon Green BAPTA 5N and confocal laser scanning microscopy', *Cell Calcium*, 31(4), pp. 151–159. doi: 10.1054/ceca.2001.0269.
- Wilson, K. C. P. and Raisman, G. (1980) 'Age-related changes in the neurosensory epithelium of the mouse vomeronasal organ: Extended period of post-natal growth in size and evidence for rapid cell turnover in the adult', *Brain Research*, 185(1), pp. 103–113. doi: 10.1016/0006-8993(80)90675-7.
- Wyatt, T. D. (2009) 'Fifty years of pheromones', *Nature*, 457(7227), pp. 262–263. doi: 10.1038/457262a.
- Wysocki, C. J., Wellington, J. L. and Beauchamp, G. K. (1980) 'Access of Urinary Nonvolatiles to the Mammalian Vomeronasal Organ', *Science*, 207(4432), pp. 781–783. doi: 10.1126/science.7352288.
- Xu, H. and Ren, D. (2015) 'Lysosomal Physiology', *Annual Review of Physiology*, 77(1), pp. 57–80. doi: 10.1146/annurev-physiol-021014-071649.
- Yao, S. *et al.* (2017) 'Oxytocin signaling in the medial amygdala is required for sex discrimination of social cues', *eLife*, 6. doi: 10.7554/eLife.31373.

6. References

- Yoles-Frenkel, M. *et al.* (2017) 'In vivo stimulus presentation to the mouse vomeronasal system: Surgery, experiment, setup, and software', *Journal of Neuroscience Methods*. Elsevier B.V., 285, pp. 19–32. doi: 10.1016/j.jneumeth.2017.05.001.
- Yoles-Frenkel, M., Kahan, A. and Ben-Shaul, Y. (2018) 'Temporal Response Properties of Accessory Olfactory Bulb Neurons: Limitations and Opportunities for Decoding', *The Journal of Neuroscience*, 38(21), pp. 4957–4976. doi: 10.1523/JNEUROSCI.2091-17.2018.
- Yonekura, J. and Yokoi, M. (2008) 'Conditional genetic labeling of mitral cells of the mouse accessory olfactory bulb to visualize the organization of their apical dendritic tufts', *Molecular and Cellular Neuroscience*, 37(4), pp. 708–718. doi: 10.1016/j.mcn.2007.12.016.
- Young, J. M. and Trask, B. J. (2007) 'V2R gene families degenerated in primates, dog and cow, but expanded in opossum', *Trends in Genetics*, 23(5), pp. 212–215. doi: 10.1016/j.tig.2007.03.004.
- Zylbertal, A. *et al.* (2015) 'Prolonged Intracellular Na⁺ Dynamics Govern Electrical Activity in Accessory Olfactory Bulb Mitral Cells', *PLoS Biology*, 13(12), pp. 1–25. doi: 10.1371/journal.pbio.1002319.
- Zylbertal, A., Yarom, Y. and Wagner, S. (2017) 'Synchronous Infra-Slow Bursting in the Mouse Accessory Olfactory Bulb Emerge from Interplay between Intrinsic Neuronal Dynamics and Network Connectivity', *The Journal of Neuroscience*, 37(10), pp. 2656–2672. doi: 10.1523/JNEUROSCI.3107-16.2017.
- Zysow, B. R. *et al.* (1997) 'Effects of Estrus Cycle, Ovariectomy, and Treatment with Estrogen, Tamoxifen, and Progesterone on Apolipoprotein(a) Gene Expression in Transgenic Mice', *Arteriosclerosis, Thrombosis, and Vascular Biology*, 17(9), pp. 1741–1745. doi: 10.1161/01.ATV.17.9.1741.

7. Abbreviations

ADP	Adenosine diphosphate
AL	Apical layer
AMC	Accessory olfactory bulb mitral cell
AMPA	α -amino-3-hydroxy-5-methyl-4-isoxazolepropionic acid
AOB	Accessory olfactory bulb
AON	Accessory olfactory nucleus
AOS	Accessory olfactory System
AP	Action potential
AP5	Amino-5-phosphonopentanoate
ATP	Adenosine triphosphate
AU	Arbitrary unit
BL	Basal layer
BV	Blood vessel
CaM	Calmodulin
COV	Coefficient of variation
cpEGFP	Circular permuted enhanced green fluorescent protein
CRAC	Calcium release-activated calcium channel
DIC	Differential interference contrast
eGC	External granule cell
ER	Endoplasmic reticulum
FPR	Formyl peptide receptors
FWHM	Full width at half maximum
GABA	Gamma-aminobutric acid
GC	Granule cell

7. Abbreviations

GCL	Granule cell layer
GECI	Genetically encoded calcium indicator
GFP	Green fluorescent protein
GL	Glomerular layer
IET	Inter event time
iGC	Internal granule cell
Ins(1,4,5)P ₃ R	Inositol 1,4,5-trisphosphate receptor
JGN	Juxtaglomerular neuron
LOT	Lateral olfactory tract
MCL	Mitral cell layer
MCU	Mitochondrial calcium uniporter
MHC	Major histocompatibility complex
MOE	Main olfactory epithelium
MOS	Main olfactory system
MUP	Major urinary proteins
NBQX	2,3-dioxo-6-nitro-7-sulfamoyl-benzo[f]quinoxaline
NMDA	N-methyl-D-aspartate
OB	Olfactory bulb
OCAM	Olfactory axon cell adhesion molecule
OGB1-AM	Oregon Green Bapta-1-AM
OMP	Olfactory marker protein
ORAI1	Calcium release-activated calcium channel protein 1
PGC	Periglomerular cell
PMCA	Plasma membrane calcium ATPase
PP	Perfusion pencil

7. Abbreviations

PSD	Power spectral density
RyR	Ryanodine receptor
SERCA	Sarcoplasmic/endoplasmic reticulum calcium ATPase
STIM1	Stromal interaction molecule 1
TRPC	Transient receptor potential channel
TRPML	Transient receptor channel mucolipin receptor
VDAC	Voltage-dependent anion-selective channel proteins
VMH	Ventromedial hypothalamus
VNL	Vomeroneasal nerve layer
VNO	Vomeroneasal organ
VSN	Vomeroneasal sensory neuron
V1R	Vomeroneasal receptor type 1
V2R	Vomeroneasal receptor type 2
wt	Wild type

8. Acknowledgement

Abschließend möchte ich mich bei all den Menschen bedanken, die mich bei der Durchführung dieser Arbeit unterstützt und somit zum Erfolg dieser beigetragen haben.

Beginnend möchte ich mich herzlichst bei meinem Doktorvater Prof. Dr. Marc Spehr bedanken. Marc, du hast mich seit nunmehr 6 Jahren wissenschaftlich sowie persönlich begleitet und gefördert. Ich danke dir für das von vorneherein entgegengebrachte Vertrauen, sowohl in Bezug auf selbstständiges wissenschaftliches Arbeiten, die Möglichkeit Abschlussarbeiten zu betreuen, sowie Vorlesungen zu halten. Weiterhin hast du mir direkt zu Beginn meiner Promotion ermöglicht Erfahrungen im Ausland zu sammeln.

Auch möchte ich dir dafür danken stets ein offenes Ohr für meine Anliegen zu haben. Du hast durch deine stetige Unterstützung maßgeblich zu meiner professionellen und persönlichen Weiterentwicklung beigetragen.

Weiterhin möchte ich Prof. Dr. Björn Kampa für die Zweitbetreuung dieser Arbeit und das stetige fachliche Interesse an meiner wissenschaftlichen Tätigkeit bedanken. Ich habe die Gespräche mit dir stets als Bereicherung empfunden.

In addition, I would like to express my sincerest thanks to Prof. Dr. Yoram Ben-Shaul. Yoram, you supported me strongly expanding my knowledge in the field of data science and agreed to function as external supervisor for this thesis. Aside from the scientific support I also would like to thank you for inviting me to Israel. The time in your lab broadened my scientific and personal horizon enormously.

Als Mitglieder des Graduiertenkollegs 2416 möchte ich der Deutschen Forschungsgemeinschaft für die finanzielle und ideelle Unterstützung meiner Arbeit danken. Weiterhin bedanke ich mich bei der Minerva Stiftung für die Förderung meines Aufenthalts an der Hebrew University of Jerusalem, Israel.

Weiterhin möchte ich allen ehemaligen und aktuellen Mitgliedern der AG Chemosensorik für das kollegiale und produktive Arbeitsumfeld danken. Dr. David Fleck möchte ich für die stetige Hilfe bei der technischen Entwicklung danken. Julia Mohrhardt danke ich für den wissenschaftlichen Austausch während des Projekts.

8. Acknowledgement

In addition, I want to thank my girlfriend Andrea. Thank you for your never-ending support and always believing in me. I can't put in words how much this helps me to pursue my way.

Besonderer Dank gilt meiner Familie, insbesondere meinen Eltern. Ihr habt mich stets in allen Phasen meines Lebens unterstützt und nie an mir gezweifelt. Ohne eure stetige Unterstützung wäre meine akademische Laufbahn in dieser Form nicht möglich gewesen. Danke für alles!

9. Curriculum Vitae

Address: Veltmanplatz 8a, 52062 Aachen, Germany
Day of birth: 28th February 1993 in Bergheim, Germany
e-Mail: s.malinowski@sensorik.rwth-aachen.de

Education

- 11/2017 – 08/2022 **Doctoral Student in Neuroscience (Dr. rer. nat.)**
Research Training Group 2416, RWTH Aachen University
- 10/2015 – 09/2017 **Master of Science in Biology (Grade 1.1 | Passed with Excellence | Dean's List)**
Institute of Biology II, Department of Chemosensation,
RWTH Aachen University
Master thesis: „Investigation of Mitral Cell Calcium Oscillations in the Mouse Accessory Olfactory Bulb“ (**Grade: 1.0**)
- 10/2012 – 08/2015 **Bachelor of Science in Biology (Grade: 2.2)**
Institute of Biology II, Department for Animal Physiology,
RWTH Aachen University
Bachelor thesis: “Influence of Intrinsic Properties on the Adaptation of Neurons in the Central Inferior Colliculus of the Chicken (*Gallus gallus domesticus*)” (**Grade: 1.0**)
- 07/2003 – 06/2012 **Abitur (Grade: 1.8)**
Erftgymnasium Bergheim

Research Experience

- 02/2018 – 03/2018 **Visiting Research Fellow**
School of Medicine, The Hebrew University of Jerusalem, Israel
- 12/2016 – 09/2017 **Research Assistant**
Institute of Biology II, Department for Animal Physiology,
RWTH Aachen University, AG Spehr
- 10/2016 – 12/2016 **Research Internship**
Institute of Biology II, Department for Animal Physiology,
RWTH Aachen University, AG Spehr
- 07/2015 – 09/2016 **Scientific Assistant**
Institute of Biology II, Department for Animal Physiology,
RWTH Aachen University, AG Künzel

9. Curriculum Vitae

Teaching Experience

- 12/2020 – Present **Lecturer in the Master Study Program Biology**
RWTH Aachen University
- 01/2019 – 09/2020 **Thesis Supervisor**
Bachelor Thesis of Kristine Schuster and Moritz Nesseler,
Department for Animal Physiology, RWTH Aachen University
- 11/2018 – Present **Lecturer in the Bachelor Study Programs Biology,
Mathematics and Informatics**
RWTH Aachen University
- 07/2015 – Present **Teaching Instructor**
Animal Physiology Practical Course (B.Sc.),
RWTH Aachen University

Fellowships and Awards

- Since 10/2018 **Affiliated Member and Student Speaker of the DFG Research
Training Group 2416 “Multi Senses – Multi Scales”**
RWTH Aachen University
- 01/2018 **Named to the „Dean’s List“**
RWTH Aachen University
- 12/2017 **Minerva Short-Term Research Grant**
Minerva Foundation of the Max-Planck-Society
- 12/2016 **Undergraduate Funds**
RWTH Aachen University
- 10/2016 – 10/2017 **Education Fund (Deutschlandstipendium)**
Bayer Science & Education Foundation
- Since 09/2016 **e-fellows.net fellowship**

9. Curriculum Vitae

Publications (peer-reviewed)

- 03/2020 Tsitoura C.*, **Malinowski ST.***, Mohrhardt J.*, Degen R., DiBenedictis BT., Gao Y., Watznauer K., Gerhold K., Nagel M., Weber M., Rothermel M., Hanganu-Opatz IL., Ben-Shaul Y., Davison IG., Spehr M.
Synchronous Infra-Slow Oscillations Organize Ensembles of Accessory Olfactory Bulb Projection Neurons into Distinct Microcircuits, *Journal of Neuroscience*
Doi: <https://doi.org/10.1523/JNEUROSCI.2925-19.2020>
- 07/2019 **Malinowski ST.**, Wolf J, Kuenzel T.
Intrinsic and Synaptic Dynamics Contribute to Adaptation in the Core of Avian Central Nucleus of the Inferior Colliculus, *Frontiers in Neural Circuits*
Doi: 10.3389/fncir.2019.00046

Conference Poster

- 09/2021 **Malinowski ST.**, Mohrhardt J., Tsitoura C., Fleck D., DiBenedictis BT., Gao Y., Davison I., Ben-Shaul Y., Spehr M.
Synchronous Infra-Slow Oscillations Organize Ensembles of Accessory Olfactory Bulb Projection Neurons into Distinct Microcircuits In Vitro and In Vivo, ECRO2021 - Meeting of the European Chemoreception Research Organization, Cascais, Portugal
- 03/2019 **Malinowski S.**, Mohrhardt J., Tsitoura C., Ben-Shaul Y., Spehr M.
Physiological analysis of oscillatory microcircuits in the mouse accessory olfactory bulb. 13th Meeting of the German Neuroscience Society, Göttingen, Germany
- 04/2018 Mohrhardt J., Tsitoura C., **Malinowski S.**, Watznauer K., Gorin M., Ben-Shaul Y., Spehr M.
Infraslow Oscillations in the Mouse Accessory Olfactory Bulb. 39th Annual Meeting of the Association of Chemoreception Sciences, Bonita Springs, USA
- 11/2017 Mohrhardt J., Tsitoura C., Watznauer K., **Malinowski S.**, Gerhold K., Gorin M., Spehr M.
Infraslow Oscillations in the Mouse Accessory Olfactory Bulb. Annual Meeting of the Society for Neuroscience, Washington DC, USA

9. Curriculum Vitae

- 10/2017 Spehr M., Tsitoura C., Nagel M., Degen R., Mohrhardt J., **Malinowski S.**, Ben-Shaul Y.
Signaling Mechanisms in the Mouse Accessory Olfactory System. 27th Annual Meeting of the European Chemoreception Research Organization, Cambridge, UK
- 04/2017 Tsitoura C., Mohrhardt J., Gerhold K., Gorin M., **Malinowski S.**, Watznauer K., Spehr M.
Infraslow oscillations in the mouse accessory olfactory bulb. 38th Annual Meeting of the Association of Chemoreception Sciences, Bonita Springs, USA
- 02/2017 Wolf J., **Malinowski ST.**, Kuenzel T.
Characterization of Ascending Synaptic Connections in the Core of the Central Nucleus of the Inferior Colliculus of the Chicken. 40th Annual Midwinter Meeting of the Association for Research in Otolaryngology, Baltimore, USA
- 02/2016 Kuenzel T., **Malinowski S.**, Kurth S., Wagner H.
In-vitro analysis of intrinsic and synaptic contributions to adaptation in the avian central nucleus of the inferior colliculus. 39th Annual Midwinter Meeting of the Association for Research in Otolaryngology, San Diego, USA

10. Eidesstattliche Erklärung

Sebastian Tobias Malinowski

erklärt hiermit, dass diese Dissertation und die darin dargelegten Inhalte die eigenen sind und selbständig, als Ergebnis der eigenen originären Forschung, generiert wurden.

Hiermit erkläre ich an Eides statt:

1. Diese Arbeit wurde vollständig oder größtenteils in der Phase als Doktorand dieser Fakultät und Universität angefertigt.
2. Sofern irgendein Bestandteil dieser Dissertation zuvor für einen akademischen Abschluss oder eine andere Qualifikation an dieser oder einer anderen Institution verwendet wurde, wurde dies klar angezeigt.
3. Wenn immer andere eigene- oder Veröffentlichungen Dritter herangezogen wurden, wurden diese klar benannt.
4. Wenn aus anderen eigenen- oder Veröffentlichungen Dritter zitiert wurde, wurde stets die Quelle hierfür angegeben. Diese Dissertation ist vollständig meine eigene Arbeit, mit der Ausnahme solcher Zitate.
5. Alle wesentlichen Quellen und Unterstützungen wurden benannt.
6. Wenn immer ein Teil dieser Dissertation auf der Zusammenarbeit mit anderen basiert, wurde von mir klar gekennzeichnet, was von anderen und was von mir selbst erarbeitet wurde.
7. Teile dieser Arbeit wurden zuvor veröffentlicht und zwar in: The Journal of Neuroscience (DOI: <https://doi.org/10.1523/JNEUROSCI.2925-19.2020>)

Datum:

Unterschrift